Modeling the (proto)neutron star crust: toward a controlled estimation of uncertainties

Thomas Carreau

May 28, 2020

Contents

List of Figures

List of Tables

Chapter 1

Structure and equation of state of cold non-accreting neutron stars

This chapter deals with the structure and equation of state (EoS) of neutron stars (NS) within the framework of the "cold catalyzed matter" (CCM) hypothesis.

With typical temperature of about $T \sim 10^8$ K ~ 0.01 MeV$/k_B$, NS are very cold systems from the nuclear physics viewpoint, therefore the CCM hypothesis is commonly used to predict their internal composition and pressure. In this limit, thermal, nuclear, and beta equilibrium are established at zero temperature, meaning that the energy cannot be lowered by weak, strong, or electromagnetic processes, thus the matter is in its ground state. It is reasonable to expect these equilibrium conditions to be valid in any NS as far as it is not accreting matter from a neighbor. Indeed, in the accretion scenario, the typical timescale of the process are such that the matter composition is believed to be out of equilibrium.

As already discussed in the general introduction, the EoS relates, in given conditions of temperature and densities, the macroscopic quantities of the star, such as the mass density and the pressure, which determines among others the mass-radius relation of NS. The evaluation of the EoS therefore implies to know the microscopic composition at each point in the star. At subsaturation densities, the solid crust consists mainly of clusterized matter, arranged in a body-centered cubic lattice [HPY07]. The relevant degrees of freedom in the crust are the Wigner-Seitz (WS) cells, containing exactly one lattice point [WS33]. At zero temperature, WS cells are supposed to be identical, thus the so-called single nucleus approximation (SNA), which considers a unique configuration for a given thermodynamic condition of temperature and pressure (P,T), becomes exact. The ground state of the outer crust is almost entirely characterized by experimental nuclear masses, which are available up to $(N - Z)/A \lesssim 0.3$. The determination of inner-crust ground state is however more challenging because the crust is permeated by free neutrons, a situation which cannot be achieved in terrestrial conditions. Therefore, different treatments, from microscopic [NV73] to classical [BBP71], can be envisaged to estimate the energy of matter, and the EoS in this region depends on the nucleon-nucleon (NN) effective interaction or energy functional. At suprasaturation densities, matter consists of a uniform plasma of neutrons, protons, electrons, and eventually muons, in both strong and weak equilibrium. The development of a unified EoS, that is such that

matter at subsaturation and supersaturation densities are treated within a unique model, is essential if one wants to make realistic predictions on NS observables [For+16].

The plan of the chapter is as follows. In Section 1.1, the ground state of the outer crust is determined by application of the method introduced by Baym, Pethick, and Sutherland (BPS) [BPS71], using experimental masses [Hua+17] supplemented by state-of-the-art microscopic theoretical mass tables. Section 1.2 is devoted to the determination of the inner-crust ground state using a compressible liquid drop model (CLDM) based on the metamodeling technique [MHG18a; CGM19a]. The phase transition from the solid crust to the liquid core, occuring at some ≈ 1 km from the surface of the star, is investigated. In Section 1.3, we calculate the ground state of matter in the outer core, and we address the problem of the inner-core composition. In Section 1.4, a unified metamodeling of the EoS is proposed. Finally, conclusions are given in Section 1.5.

Contents

1.1 Ground state of the outer crust

At zero temperature, the matter inside the outer crust corresponds to a lattice of strongly bound nuclei, immersed in an sea of electrons. The mass density at which nuclei are fully ionized and electron completely degenerated is of the order of $\rho \gg 6AZ \sim 10^4$ g/cm^3 for ^{56}Fe, which is the ground state of matter at very low density. Below 10^4 g/cm^3, some electrons are still bound to the nuclei and one must rely on the EoS calculated by Feynman, Metropolis, and Teller from 15 to 10^4 g/cm^3, suitable for the envelope of neutron stars [FMT49].

This section deals with the determination of the outer-crust ground state. In 1.1.1, we detail the different terms entering the WS cell energy, with emphasis on the relativistic electron gas energy as well as nuclear masses. The ground state of the outer crust is calculated by application of the variational BPS method [BPS71], which is presented in 1.1.2. Finally, using current knowledge on experimental masses [Hua+17] supplemented by different microscopic theoretical mass tables, we compute the equilibrium composition and EoS. Our results are presented in 1.1.3.

1.1.1 Wigner-Seitz cell energetics

In the outer crust, a WS cell is composed of a strongly bound nucleus at the center, immersed in a relativistic electron gas of density n_e. Charge neutrality is assured in each unit cell, $n_e = n_p$, with n_p the proton density inside the cell.

The energy of a WS cell in the outer crust can therefore be written as

$$E_{WS} = E_i + V_{WS}\varepsilon_e, \tag{1.1}$$

with E_i the ion energy, V_{WS} the volume of the cell, and ε_e the energy density of the relativistic electron gas. The ion energy reads

$$E_i = M'(A, Z)c^2 + E_L + E_{zp}, \tag{1.2}$$

where $M'(A, Z)c^2$ is the nuclear mass of a nucleus with associated mass number A and charge number Z, E_L the temperature-independent static-lattice term, and E_{zp} the zero-point quantum vibration term given by

$$E_{zp} = \frac{3}{2}\hbar\omega_p u_1, \tag{1.3}$$

where $u_1 = 0.5113875$ is a numerical constant for a body-centered cubic lattice (see Table 2.4 of [HPY07]), which is assumed to be the geometry minimizing the lattice energy. This assumption was recently confirmed in [CF16]. The ion plasma frequency ω_p is given by

$$\hbar\omega_p = \sqrt{\frac{(\hbar c)^2 4\pi n_N (Ze)^2}{M'(A, Z)c^2}}, \tag{1.4}$$

e being the elementary charge, c the speed of light, $\hbar = h/2\pi$ the reduced Planck constant, and where the ion density $n_N = 1/V_{WS}$ has been introduced.
The lattice energy reads

$$E_L = -C_M \frac{(Ze)^2}{a_N}, \tag{1.5}$$

with $C_M = 0.895929255682$ the Mandelung constant for a body-centered cubic lattice (see Table 2.4 of [HPY07]), and $a_N = (4\pi n_N/3)^{-1/3}$ the ion-sphere radius.

1.1.1.1   Nuclear mass tables

An essential input for Eq. (1.2) is the nuclear mass table. When available, that is for $I = (N-Z)/A \lesssim 0.3$, we use experimental masses from the 2016 Atomic Mass Evaluation (AME) [Hua+17]. For more neutron-rich nuclei and until we reach the neutron drip line, the use of a model is required, thus a model dependence arises. A possibility is to rely on microscopic Hartree-Fock-Bogoliubov (HFB) theoretical mass tables [Sam+02], which are based on the nuclear energy-density functional theory that is discussed in the general introduction.

In general, atomic masses are tabulated instead of the nuclear ones which can be calculated as

$$M'(A, Z)c^2 = M(A, Z)c^2 - Zm_ec^2 + B_e(Z), \tag{1.6}$$

with $M(A, Z)c^2 = \Delta\epsilon + Am_uc^2$ the atomic mass ($\Delta\epsilon$ is the mass excess, m_u is atomic mass unit), m_e the electron mass, and B_e the binding energy of atomic electrons depending solely on the number of protons Z according to the approximation proposed in [LPT03] (see their Eq. (A4)),

$$B_e(Z) = 1.44381 \times 10^{-5}Z^{2.39} + 1.55468 \times 10^{-12}Z^{5.35}. \tag{1.7}$$

1.1.1.2   Relativistic electron gas

In the outer crust, the mass densities are above $\sim 10^4$ g/cm^3 therefore the electrons are essentially free.
The expression of the energy density of a relativistic electron gas, with rest mass energy, at zero temperature can be calculated as

$$
\begin{aligned}
\varepsilon_e(n_e) &= \int_0^{k_e} \frac{k^2 dk}{\pi^2} c\sqrt{\hbar^2 k^2 + m_e^2 c^2} \\
&= \frac{P_r}{8\pi^2}\left[x_r(1 + 2x_r^2)\gamma_r - \ln(x_r + \gamma_r)\right],
\end{aligned}
\tag{1.8}
$$

with $P_r = m_e^4 c^5/\hbar^3$ the relativistic unit of the electron pressure, $x_r = \hbar k_e/(m_e c)$ the relativity parameter, and $\gamma_r = \sqrt{1 + x_r^2}$. k_e is the electron Fermi wave number given by

$$k_e = (3\pi^2 n_e)^{1/3}. \tag{1.9}$$

The derivation of Eq. (1.8) is given in Appendix A.
Above 10^7 g/cm^3, $x_r \gg 1$, thus electrons can be considered ultrarelativistic and Eq. (1.8) becomes

$$\varepsilon_e(n_e) = \frac{3}{4}n_e m_e c^2 x_r. \tag{1.10}$$

Taking the derivative of Eq. (1.8) with respect to the electron gas density yields the pressure,

$$
\begin{aligned}
P_e &= -\frac{\partial(V_{WS}\varepsilon_e)}{\partial V_{WS}} = n_e\frac{\partial\varepsilon_e}{\partial n_e} - \varepsilon_e \\
&= \frac{P_r}{8\pi^2}\left[x_r(1+2x_r{}^2)\gamma_r - \ln(x_r+\gamma_r)\right].
\end{aligned}
\tag{1.11}
$$

The exchanges and correlation corrections are neglected since they are known to be small in comparison to the kinetic energy of relativistic electrons. The expression of the exchange correction to the free energy density for a strongly degenerate electron gas is given in [HPY07] (see their Eq. (2.151)). We have checked that the inclusion of these corrections does not modify the results presented in this chapter.

1.1.2   The BPS model

The variational technique which is currently used to calculate the ground state of the outer crust was introduced by Baym, Pethick, and Sutherland in [BPS71].

The zero-temperature Gibbs free energy per nucleon is the quantity to be minimized at fixed pressure P under the condition of charge neutrality $n_e = Zn_N$, until the neutron drip sets in, the condition for which is $\mu_n = m_n c^2$, with μ_n the neutron chemical potential, and m_n the neutron mass.

The definition of the zero-temperature Gibbs free energy per nucleon is

$$
g = \frac{\varepsilon_{WS} + P}{n_B},
\tag{1.12}
$$

where $\varepsilon_{WS} = E_{WS}/V_{WS}$ is the energy density of the WS cell, and n_B is the baryon density given by $n_B = n_N A = A/V_{WS}$.

We can calculate the pressure as

$$
P = n_B{}^2\frac{\partial(\varepsilon_{WS}/n_B)}{\partial n_B}\bigg|_{Z,A},
\tag{1.13}
$$

yielding, using Eq. (1.1),

$$
P = P_e + \frac{1}{3}E_L n_N + \frac{1}{2}E_{zp}n_N.
\tag{1.14}
$$

Thus the expression of the zero-temperature Gibbs free energy per nucleon can be rewritten as

$$
g = \frac{M'(A,Z)c^2 + \frac{4}{3}E_L + \frac{1}{2}E_{zp} + Z\mu_e}{A},
\tag{1.15}
$$

where μ_e is the electron chemical potential given by

$$
\mu_e = \frac{\partial\varepsilon_e}{\partial n_e}.
\tag{1.16}
$$

Essentially, one fixes the pressure P, calculates for each nucleus (A,Z) the electronic density by solving numerically Eq. (1.14), then constructs a table (g, A, Z). The ground

state of the outer crust at pressure P then corresponds to the nucleus associated to the minimum value of g.

As explained in [Pea+18], the neutron chemical potential can be calculated through

$$\mu_n = g, \tag{1.17}$$

because the beta equilibrium equation $\mu_n = \mu_p + \mu_e$ holds throughout the star. Indeed, by exploiting the thermodynamic relation

$$\mathcal{G} = \varepsilon + P = \mu_n n_n + \mu_p n_p + \mu_e n_e, \tag{1.18}$$

together with the charge neutrality condition $n_e = n_p$, we obtain

$$\mathcal{G} = \mu_n n_n + (\mu_e + \mu_p)n_p, \tag{1.19}$$

where $\mathcal{G}$ is the zero-temperature Gibbs free energy density, and μ_p the proton chemical potential. In the case where the chemical equilibrium is established, that is if weak processes are at the equilibrium, we finally get

$$\mathcal{G} = \mu_n n_B. \tag{1.20}$$

One should stress that while minimizing the zero-temperature Gibbs free energy per nucleon at fixed pressure is less practical than simply minimizing the total energy density at constant baryon density, it makes it easier to study the transitions between layers. The pressure increases continuously with increasing depth in the star, thus a discontinuity in the density is the signature of a transition from a layer (A, Z) to another (A', Z'). Noting that the pressure in the outer crust is approximately equal to the pressure of the electron gas (the lattice and zero-point terms contribute to less than 5% to the total pressure in the bottom layers of the outer crust), we know that $n_e = n_p$ is continuous across the transition thus

$$\Delta n_B = n'_B - n_B \simeq n_p \left(\frac{A'}{Z'} - \frac{A}{Z} \right), \tag{1.21}$$

and the fractional change in the baryon mass density results

$$\frac{\Delta \rho_B}{\rho_B} \simeq \frac{\Delta n_B}{n_B} \simeq \frac{Z/A}{Z'/A'} - 1. \tag{1.22}$$

For this reason, it is more convenient to have the pressure as the independent variable. In this way we avoid to make a Maxwell construction to estimate the pressure at which the transition from (A, Z) to (A', Z') occurs.

The BPS model is still widely used to determine the ground state of the outer crust. However, at that time the authors took the values of nuclear binding energy from the outdated phenomenological macroscopic model of Myers and Swiatecki [MS65]. Moreover, they did not take into account the zero-point vibration energy, Eq. (1.3). In the last decades, considerable efforts have been made to measure nuclear masses near the neutron drip line [LPT03], as well as theoretical developments were achieved to construct microscopic mass tables [Sam+02]. It is therefore important to reevaluate the ground

state of the outer crust considering those experimental and theoretical advances. In this line, Haensel and Pichon studied the consequences of progress concerning the experimental determination of atomic masses in 1994 [HP94]. The authors found that the ground state of the outer crust can be determined exclusively by experimental masses in a fully model independent way up to $\rho_B \approx 10^{11}$ g/cm^3. From this density up to the neutron drip point, the phenomenological, liquid-drop based mass formula of Möller was used, the formalism of which is described in [MN88].

In the same spirit as [HP94], we calculate, in the following, the ground state of the outer crust using the present day knowledge on experimental masses of neutron rich nuclei [Hua+17; Wel+17] combined with state-of-the-art microscopic theoretical mass tables [GCP13].

1.1.3 Equilibrium composition and equation of state

We turn to the numerical results obtained applying the BPS method presented in 1.1.2. The ground state of the outer crust is calculated, beginning at $P = 3 \times 10^{-11}$, corresponding approximately to $n_B \approx 10^{-9}$ fm^{-3}, in order to ensure complete ionization and electron degeneracy. The pressure is increased from steps of $0.02P$ until the neutron drip point, defined by $\mu_n - m_n c^2 = 0$, is reached.

The ground-state composition and EoS of the outer crust of a cold non-accreting NS is reported in Table 1.1. The upper part of the table, $n_B < 3.84 \times 10^{-5}$ fm^{-3}, corresponding to $\rho_B < 6.39 \times 10^{10}$ g/cm^3, is exclusively determined by experimental data from the AME2016 [Hua+17]. Let us notice that the maximum mass density at which experimentally studied nucleus ^{80}Zn was present was found to be slightly lower in [HP94], $\rho_B = 5.44 \times 10^{10}$ g/cm^3. This is due to the fact that the determination of this value of density depends on the mass formula used, here HFB-24, for the neutron rich nuclides present in the bottom layers of the outer crust. From 3.84×10^{-5} fm^{-3}, matter becomes so neutron rich that the nuclear masses cannot be measured experimentally for now, thus a model dependence is expected to arise because the nuclear masses have to be extrapolated from laboratory nuclei. The nuclear mass model used to calculated the ground state here is HFB-24 [GCP13], constructed from the BSk24 functional following the Hartree-Fock-Bogoliubov method [Sam+02]. The BSk24 functional is part of a family of functionals labeled BSk22 to BSk26, consisting of unconventional effective Skyrme forces with extra t_4 and t_5 terms that behave as density-dependent generalizations of the usual t_1 and t_2 terms present in traditional Skyrme forces. The functionals BSk22-26 were fitted to the 2353 experimental masses of the AME2012 [Aud+12] and differ mainly by their symmetry energy S, defined here as the difference between the energy per nucleon of pure neutron matter (PNM) e_{PNM} and the energy per nucleon of symmetric nuclear matter (SNM) e_{SNM},

$$S(n) = e_{PNM}(n) - e_{SNM}(n), \tag{1.23}$$

with n the density of nuclear matter. To a first approximation, $S(n) \simeq E_{sym}$, E_{sym} being the symmetry energy per nucleon at the saturation density of nuclear matter $n = n_{sat} \approx 0.16$ fm^{-3}. This quantity is constrained to 32, 31, 30, and 29 MeV for BSk22, BSk23, BSk24, and BSk25, respectively. For BSk26, $E_{sym} = 30$ MeV as well but the

element	Z	N	Y_p	$n_{B,max}$ (fm^{-3})	P_{max} (MeV/fm^3)	$\mu_n - m_n c^2$ (MeV)	μ_e (MeV)
^{56}Fe	26	30	0.4643	4.97×10^{-9}	3.40×10^{-10}	-8.96	0.95
^{62}Ni	28	34	0.4516	1.56×10^{-7}	4.09×10^{-8}	-8.26	2.57
^{64}Ni	28	36	0.4375	8.07×10^{-7}	3.60×10^{-7}	-7.52	4.34
^{66}Ni	28	38	0.4242	9.27×10^{-7}	4.16×10^{-7}	-7.46	4.50
^{86}Kr	36	50	0.4186	1.85×10^{-6}	1.03×10^{-6}	-7.01	5.63
^{84}Se	34	50	0.4048	6.85×10^{-6}	5.64×10^{-6}	-5.87	8.59
^{82}Ge	32	50	0.3902	1.67×10^{-5}	1.77×10^{-5}	-4.82	11.41
^{80}Zn	30	50	0.3750	3.84×10^{-5}	5.10×10^{-5}	-3.58	14.86
^{78}Ni	28	50	0.3590	6.68×10^{-5}	1.01×10^{-4}	-2.63	17.61
^{126}Ru	44	82	0.3492	7.52×10^{-5}	1.12×10^{-4}	-2.47	18.15
^{124}Mo	42	82	0.3387	1.21×10^{-4}	2.04×10^{-4}	-1.54	21.05
^{122}Zr	40	82	0.3279	1.56×10^{-4}	2.75×10^{-4}	-1.03	22.69
^{121}Y	39	82	0.3223	1.63×10^{-4}	2.84×10^{-4}	-0.98	22.86
^{120}Sr	38	82	0.3167	1.95×10^{-4}	3.52×10^{-4}	-0.60	24.12
^{122}Sr	38	84	0.3115	2.37×10^{-4}	4.49×10^{-4}	-0.15	25.62
^{124}Sr	38	86	0.3065	2.56×10^{-4}	4.87×10^{-4}	0.00	26.14

Table 1.1: Ground state of the outer crust of a cold non-accreting neutron star. Experimental data from the 2016 Atomic Mass Evaluation [Hua+17] are used when available. Mass excesses of $^{77-79}$Cu are taken from [Wel+17]. Experimental masses are supplemented with masses from microscopic HFB-24 theoretical mass table [GCP13] (lower part). The last line corresponds to the neutron drip point. The following quantities are reported in the table: the element, the atomic number Z, the neutron number N, the proton fraction $Y_p = Z/A$ (A is the number of nucleons), the maximum baryon density $n_{B,max}$ at which the nuclide is found, the associated pressure P_{max}, the neutron chemical potential minus rest mass $\mu_n - m_n c^2$, and the electron chemical potential μ_e.

functional is fitted to the APR EoS of PNM [APR98], unlike BSk22-25 that are fitted to the stiffer LS2 EoS [LS08].

The first layer of the outer crust consists of a crystal lattice of ^{56}Fe, the mass per nucleon of which is the lowest among all nuclides. The sequence of nuclides is in good agreement with the results of [HP94]. One can note the persistence of magic numbers $Z = 28$ and $N = 50$ at low density, and $Z = 82$ at higher density. In particular, in [HP94] the $N = 82$ shell is found from $\rho_B = 9.64 \times 10^{10}$ g/cm^3 to 4.32×10^{11} g/cm^3, point of neutron drip (see Table 3.1 of [HPY07]). It is explained in [HPY07] that the apparent strong effect of the $N = 82$ shell in the bottom layers could be an artifact of the extrapolation using the mass formula of [MN88] and that further investigations on nuclear shell structure in the vicinity of the neutron drip point were required. Here we find two additional layers of strontium ($N = 84$ and $N = 86$) with respect to [HP94] results, and the layer of ^{118}Kr before the neutron drip is not observed.

At high density, a thin layer of odd-mass nuclei ^{121}Y is found with the HFB-24 mass model. It is interesting since the possibility of having odd nuclei in the ground state of the outer crust was not considered in the original calculation of BPS [BPS71]. Also, it is reported in [Pea+18] that ^{79}Cu is favored over ^{76}Ni, found for HFB-22 and HFB-25, in the case where the recent mass excess measurements of [Wel+17] are accounted for. This highlights the importance of measuring the mass of odd-nuclei. One could expect that the presence of odd-nuclei in the outer crust of NS leads to ferromagnetic phase transitions at low temperature. In return, it could generate a magnetic field and alter the existing field, and so the electron gas.

It can also be observed in Table 1.1 that the proton fraction $Y_p = Z/A$ always decreases with increasing depth. The neutronization of matter can be understood by the following reason. Neglecting the static-lattice energy as well as the zero-point quantum vibrations terms, we can write the zero-temperature Gibbs energy per nucleon as

$$g \simeq \frac{M'(A,Z)c^2 + V\varepsilon_e}{n_B V} + \frac{P}{n_B}. \tag{1.24}$$

Since the lattice does not contribute to the pressure, we have $P \simeq P_e = n_e \mu_e - \varepsilon_e$, yielding

$$g \simeq \frac{M'(A,Z)c^2}{A} + \frac{n_e}{n_B}\mu_e. \tag{1.25}$$

The charge neutrality is ensured in the unit cell, therefore $n_e/n_B = Z/A$ and we finally get

$$g \simeq \frac{M'(A,Z)c^2}{A} + \frac{Z}{A}\mu_e. \tag{1.26}$$

For $\rho_B \gg 10^{-7}$ g/cm^3, electrons are ultrarelativistic and the electron chemical potential is calculated by taking the derivative of Eq. (1.10),

$$\mu_e = \frac{\partial \varepsilon_e}{\partial n_e} = \frac{3}{4}\hbar c(3\pi^2)^{1/3} n_e^{4/3}. \tag{1.27}$$

Therefore, the electron chemical potential μ_e scales as $P^{1/4}$ ($P \propto n_e^{4/3}$). Then it appears that, with increasing pressure, it is energetically favorable to decrease the proton fraction $Y_p = Z/A$ in order to compensate the increase in the term $M'(A,Z)c^2/A$.

The neutron chemical potential monotonously increases with increasing density and at $n_B = 2.56 \times 10^{-4}$ fm^{-3}, corresponding to $P = 4.87 \times 10^{-4}$ MeV/fm^{-3}, the neutron drip is finally reached. It should be mentioned that the neutron drip density as well as pressure depend on the mass model, here chosen to be HFB-24.

The model dependence of the composition in the bottom layers of the outer crust (bottom part of Table 1.1) can be seen in Figure 1.1, where we represent the proton number Z and the neutron number N as a function of the baryon density n_B for four different mass models that reproduce with comparable accuracy the present experimental mass information: HFB-14 [GSP07], HFB-24, HFB-26 [GCP13], and FRDM [Mol+95] that supplement the experimental data. The model dependence is observed from $n_B \approx 2.5 \times 10^{-5}$ fm^{-3}, where the experimental mass data are not available. We recover similar sequences of nuclides with the different mass models, with the strong shell effect associated to
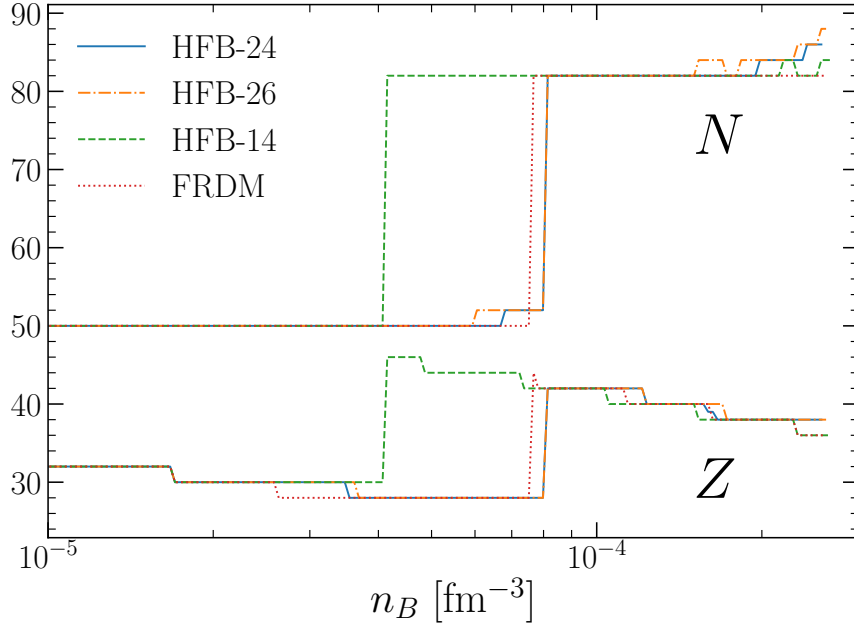
Figure 1.1: Variation with baryon density n_B of the equilibrium value of atomic number Z and neutron number N in the bottom layers of the outer crust for four different models: HFB-24, HFB-26 [GCP13], HFB-14 [GSP07], and FRDM [Mol+95].

$N = 50$ at low density and $N = 82$ in the bottom layers. A thin layer with $N = 52$ is also found for HFB-24 and HFB-26 just before the transition to $N = 82$. While this transition occurs in the vicinity of 8×10^{-5} fm^{-3} for HFB-24, HFB-26, and FRDM, it is found to happen at approximately 4×10^{-5} fm^{-3} for HFB-14. Different nuclides are found close to the neutron drip, depending on the model: ^{124}Sr is found for HFB-24, ^{126}Sr for HFB-26, ^{120}Kr for HFB-14, and ^{122}Kr for FRDM. The neutron drip density n_{ND} and pressure P_{ND} slightly depends on the model as well. These values are reported in Table 1.2.

The variation of pressure with baryon density, namely the EoS, is shown in Fig. 1.2 for the four mass models. The selected models give the same value of pressure up to $\approx 2.5 \times 10^{-5}$ fm^{-3}, as it is the case for the composition. At higher densities, we can perceive the small effect of the model, in particular at the transitions from a layer to another at which the pressure stays constant, but where a discontinuity is observed in the density.

1.2   Ground state of the inner crust

The neutron drip marks the onset of the inner crust, which is a system that cannot be reproduced in the laboratory since the dripped neutrons would evaporate, while they stay confined in the WS cell due the gravitational pressure. For this reason, the equilibrium

model	element	Z	N	n_{ND} (fm^{-3})	P_{ND} (MeV/fm^3)
HFB-24	^{124}Sr	38	86	2.56×10^{-4}	4.87×10^{-4}
HFB-26	^{126}Sr	38	88	2.62×10^{-4}	4.91×10^{-4}
HFB-14	^{120}Kr	36	84	2.67×10^{-4}	5.01×10^{-4}
FRDM	^{122}Kr	36	82	2.62×10^{-4}	4.99×10^{-4}

Table 1.2: Chemical element, atomic number Z, neutron number N, density n_{ND}, and pressure P_{ND} at the neutron drip point for four different mass models: HFB-24, HFB-26 [GCP13], HFB-14 [GSP07], and FRDM [Mol+95].
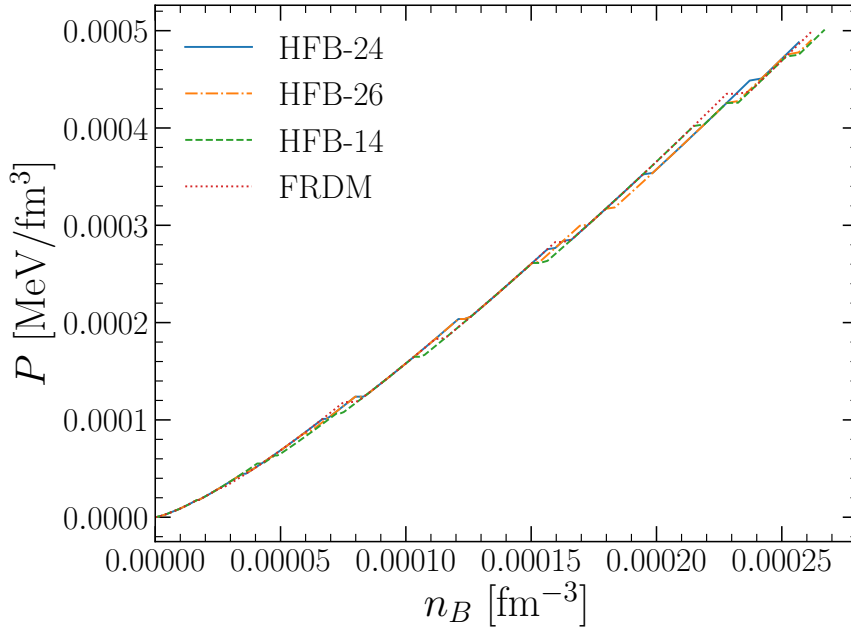
Figure 1.2: Variation with baryon density n_B of pressure P for four different models: HFB-24, HFB-26 [GCP13], HFB-14 [GSP07], and the FRDM [Mol+95].

composition and so the EoS in the inner crust are fully model dependent.

This section deals with the determination of the ground state of the inner crust. In 1.2.1, we present the metamodeling of the infinite nuclear matter EoS here used to calculate the energy of the neutron gas, and extended to finite nuclei within the so-called compressible liquid drop (CLD) approximation so as to describe the cluster energetics. The derivation of the system of equilibrium equations for the determination of inner-crust ground state is detailed in 1.2.2. The numerical method as well as results are presented afterwards, in 1.2.3. In 1.2.4 we add Strutinsky shell corrections on top of the CLD energy as an attempt to recover magic numbers in the free neutron regime. Nonspherical pasta phases in the bottom layers of the inner crust are considered in 1.2.5.
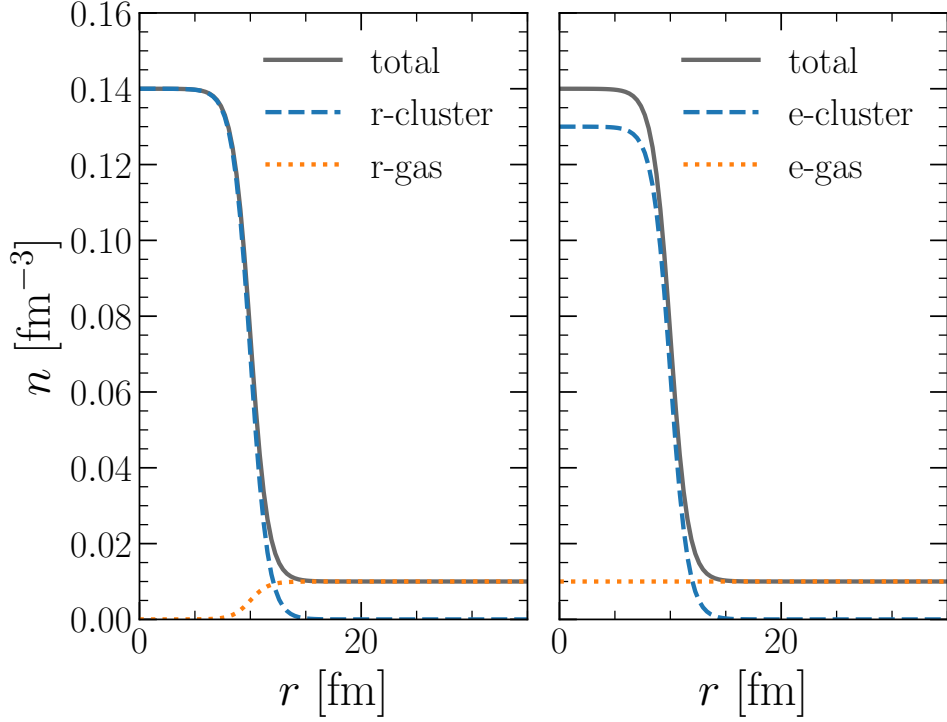
Figure 1.3: Wood-Saxon density profiles, for arbitrary values, within a WS cell in the free neutron regime. Blue dashed lines correspond to the cluster density (left, r-cluster; right, e-cluster), and orange dotted lines to the gas density. The total density profile is represented in gray solid lines.

Finally, the phase transition from the solid crust to the liquid core is investigated in 1.2.6.

1.2.1   Modeling the nuclear energy

Once the neutron dripline is reached, neutron start to drip out of nuclei but stay confined in the WS cell because of the gravitational pressure, whereas they would have been emitted in the laboratory. In the regime of the inner crust, we thus have, in each unit cell, a cluster immersed in an electron sea, and an ambient neutron gas.

There is an ambiguity regarding the characterization of the cluster-gas interface. One should ask whether the neutron gas penetrate the cluster or not. Hence, two classical representations can be introduced, namely the r-cluster and e-cluster representations [Pap+13], to interpret the distribution of the N_{WS} neutrons and Z_{WS} protons in the unit cell. In the former, the cluster occupy a volume at the center of the cell and is surrounded by the neutron gas. Evidently, there is a thin region where cluster and gas overlap given the fact that a sharp interface would be unrealistic. The r-cluster representation naturally emerges in the local density approximation in density functional theory. Indeed, if the energy is expressed as a function of the local density, then the cluster

corresponds to the dense part and the gas to the dilute one. This interpretation is used in most of the calculations at finite temperature to model supernovae, see for example the renowned Lattimer and Swesty EoS [LS91]. In the e-cluster representation, the gas penetrate the cluster. This interpretation appears spontaneously in single-particle developments. Indeed, in very neutron-rich clusters, beyond the neutron dripline, the bound states are occupied as well as the resonant and continuum states. All the unbound single-particle states that are occupied thus represents the neutron gas, characterized by a quasihomogeneous spatial distribution, the continuum wave functions being very similar to plane waves. The difference between the two representations is illustrated in Fig. 1.3. The cluster and gas density profiles, described by Woods-Saxon profiles with arbitrary values, are plotted along the WS cell radius in the r-cluster representation (left) and e-cluster representation (right). Woods-Saxon profiles are known to give a good description of medium-mass and heavy nuclei density profiles, and are commonly used in Thomas-Fermi (TF) and extended Thomas-Fermi (ETF) calculations [Ons+08; Pea+18]. In both representations, the total density profile (solid gray line) is the same. One can benefit from the advantage of both representations through the simple geometric relations

$$A_e = A\left(1 - \frac{n_g}{n_0}\right), \quad Z_e = A\left(1 - \frac{n_{g,p}}{n_{0,p}}\right), \tag{1.28}$$

where A_e (Z_e) is the number of nucleons (protons) in the e-cluster, A (Z) the number of nucleons (protons) in the r-cluster, n_g ($n_{g,p}$) the total (proton) gas density, and n_0 ($n_{0,p}$) the average total (proton) density inside the cluster. Since we do not consider the possibility of proton drip in the inner crust, we have $n_{g,p} = 0$, yielding $Z_e = Z$ and implying that the total gas density is equal to that of the neutron gas. Indeed, while free protons are expected at non-zero temperature, their presence at zero temperature remains uncertain [BBP71] and depends on the nuclear model. For some models, the proton drip could set in the very bottom layers of the crust, the classical condition for which is $\mu_p = U_p + m_p c^2$, where U_p corresponds to the proton single-particle field at the cell surface [Pea+18]. However, if nonspherical shapes are considered then it is found that protons remain in the cluster for most models.

At zero temperature, we write the WS cell energy E_{WS} in the r-cluster representation as

$$E_{WS} = E_{cl} + V_{WS}\varepsilon_e + (V_{WS} - V_{cl})\varepsilon_g + Z_{WS}(m_p - m_n)c^2 + A_{WS}m_n c^2 \tag{1.29}$$

where ε_g represents the energy density of the surrounding neutron gas of density n_g, $V_{cl} = A/n_0$ the volume of the cluster, V_{WS} that of the WS cell, and E_{cl} the energy of the cluster. The total number of protons Z_{WS} and nucleons A_{WS} inside the WS cell are given respectively by

$$Z_{WS} = A\frac{1-I}{2} \quad \text{and} \quad A_{WS} = A\left(1 - \frac{n_g}{n_0}\right) + n_g V_{WS}. \tag{1.30}$$

Let us notice that the number of protons inside the cell remains an integer number, as in the outer crust, unlike the number of neutrons that is noninteger because of the outside neutron gas.

As for the bottom layers of the outer crust, the determination of the ground state of the inner crust is fully model dependent. Therefore, the two necessary ingredients of the WS cell energy are the equation of state of PNM, and the energy of the cluster, which will be treated in the CLD approximation introduced by Baym, Bethe, and Pethick (BBP) in their pioneering work [BBP71].

1.2.1.1   Metamodeling of homogeneous nuclear matter

The ambient neutron gas in the WS cell is treated as homogeneous nuclear matter. In this limit, a large number of nucleons $A \longrightarrow \infty$ is contained in a large box. The system is entirely characterized by the neutron density n_n and the proton density n_p. Let us also introduce the total density $n = n_n + n_p$ and the asymmetry $\delta = (n_n - n_p)/n$. Two limit cases can be distinguished: pure neutron matter, where $n_p = 0$, and symmetric nuclear matter, where $n_n = n_p$. Beta-equilibrated matter corresponds to the matter inside the core of neutron stars and is treated in Section 1.3. Different methods have been proposed in order to evaluate the energy per nucleon of homogeneous nuclear matter. While considerable theoretical efforts have been devoted to ab initio approaches in the recent years [Gan+14], these calculations might become unreliable at suprasaturation densities. Also, the treatment of three-body forces, which are known to play a major role in the determination of the saturation properties of nuclear matter, remains a challenge [DHS16]. Another possibility is to derive the nuclear EoS from effective forces [Cha+98]. This second approach is very practical because of translational invariance but suffers from the possible introduction of artificial correlations among the parameter space. In the following we present the metamodeling technique [MHG18a; MHG18b]. As we will see, this technique allows to parametrize in a simple analytical way the energy per nucleon obtained in the different ab initio or effective approaches, as well as interpolate continuously between them. By largely exploring the parameter space of this metamodel (or model of models), constraints coming from experimental measurements can be directly implemented. Indeed, nuclear experiments give us knowledge on the properties of nuclear matter around the saturation density of symmetric nuclear matter n_{sat}, which is roughly the density of laboratory nuclei. For instance, the isoscalar Giant Monopole Resonance energy is correlated with the empirical parameter K_{sat}, which corresponds to the isoscalar modulus. The well-known nuclear EoS empirical parameters correspond in fact to the successive density derivatives of nuclear matter energy per particle of SNM and symmetry energy at saturation density, associated to the isoscalar (E_{sat}, K_{sat}, Q_{sat}, and Z_{sat}) and isovector channel (E_{sym}, L_{sym}, K_{sym}, Q_{sym}, and Z_{sym}), respectively. The symmetry energy is generally defined as

$$e_{HM}^{sym}(n) = \frac{1}{2} \frac{\partial^2 e_{HM}(n, \delta)}{\partial \delta^2} \bigg|_{\delta=0}, \tag{1.31}$$

where e_{HM} is the nuclear matter energy per nucleon in nuclear matter. In Table 1.3 are listed the value of each empirical parameter for the Skyrme-like SLy4 [Cha+98], BSk22, and BSk24 [GCP13], and relativistic DD-MEδ [Roc+11] functionals. Average values and associated uncertainties extracted from experimental analysis are also provided. It can be seen that the isovector parameters are in general less known with respect to the

Parameter	Unit	N	SLy4	BSk24	BSk22	DD-MEδ	Average	Uncertainty
E_{sat}	MeV	0	-15.97	-16.05	-16.09	-16.12	-15.8	0.3
n_{sat}	fm^{-3}	1	0.1595	0.1578	0.1578	0.1520	0.155	0.005
K_{sat}	MeV	2	230	246	246	219	230	20
Q_{sat}	MeV	3	-363	-274.5	-276	-748	300	400
Z_{sat}	MeV	4	1587	1184	1190	3950	-500	1000
E_{sym}	MeV	0	32.01	30.00	32.00	32.35	32	2
L_{sym}	MeV	1	46.0	46.4	68.5	52.8	60	15
K_{sym}	MeV	2	-120	-38	13	-118	-100	100
Q_{sym}	MeV	3	521	711	563	846	0	400
Z_{sym}	MeV	4	-3197	-4031	-3174	-3545	-500	1000
m^*_{sat}/m			0.69	0.80	0.80	0.69	0.75	0.1
$\Delta m^*_{sat}/m$			-0.19	0.20	0.20	-0.17	0.1	0.1

Table 1.3: Value of each of the empirical parameters, associated unit, and derivative order N for SLy4 [Cha+98], BSk24, BSk22 [GCP13], and DD-MEδ [Roc+11] functionals. Average values and uncertainties extracted from experimental analysis are taken from [MHG18a].

isoscalar ones for the same derivative order. For instance, the relative uncertainty on K_{sym} is about 100% while that of K_{sat} is less than 10%. It should also be stressed that high-order parameters $Q_{sat(sym)}$ and $Z_{sat(sym)}$ are poorly constrained by nuclear experiments.

The empirical parameters can be used in a Taylor expansion to estimate the nuclear matter EoS analytically up to $n \approx 2 - 3n_{sat}$ [MHG18a; MHG18b]. Limiting us to derivative order $N = 2$, we obtain

$$e_{HM}^{N=2}(n,\delta) = E_{sat} + \frac{1}{2}K_{sat}x^2 + \delta^2(E_{sym} + L_{sym}x + \frac{1}{2}K_{sym}x^2), \tag{1.32}$$

with $x = (n - n_{sat})/(3n_{sat})$ a function of the density. However, we should stress already that $N = 2$ is not sufficient for describing the EoS at subsaturation densities, and even less for suprasaturation densities. High-order parameters $Q_{sat(sym)}$ and $Z_{sat(sym)}$ are essential and carry the largest uncertainty as far as the bulk part of the EoS is concerned.

In a mean field approach, we can treat nucleons as independent particles, thus the kinetic part of the energy per particle of nuclear matter is given by the same functional form as a nonrelativistic Fermi gas (FG), that is

$$t_{HM}^{FG}(n,\delta) = \frac{1}{2}t_{sat}^{FG}(1+3x)^{2/3}\left[(1+\delta)^{5/3}\frac{m}{m_n^*} + (1-\delta)^{5/3}\frac{m}{m_p^*}\right], \tag{1.33}$$

where $t_{sat}^{FG} = 3\hbar^2/(10m)(3\pi^2/2)^{2/3}n_{sat}^{2/3}$ is the kinetic energy of SNM at the saturation density, $m = (m_n + m_p)/2$ is the mean nucleon mass, and m_n^* (m_p^*) is the neutron

(proton) effective mass. The Landau effective mass is introduced in order to take into account for the in-medium nuclear interaction that alters the mass of nucleons. It can be parametrized as $(q = n, p)$

$$\frac{m}{m_q^*} = \sum_{\alpha=0}^{1} m_{q,\alpha}(\delta)\frac{x^\alpha}{\alpha!} = 1 + (\kappa_{sat} + \tau_3\kappa_{sym}\delta)(1 + 3x), \quad (1.34)$$

with $\tau_3 = 1$ ($\tau_3 = -1$) for neutrons (protons). Two additional parameters κ_{sat} and κ_{sym}, related to the effective mass m_{sat}^* and isospin splitting Δm_{sat}^* at saturation density, are then introduced. They are defined at $n = n_{sat}$ as

$$\kappa_{sat} = \frac{m}{m_{sat}^*} - 1, \quad (1.35)$$

$$\kappa_{sym} = \frac{1}{2}\left(\frac{m}{m_n^*} - \frac{m}{m_p^*}\right). \quad (1.36)$$

In principle, it is possible to reproduce any EoS model with a Taylor expansion, considering an infinite number of parameters, $N \to \infty$, however the convergence would be very slow. In order to fasten the series convergence, one can add extra functional dependencies, which correspond to the true EoS in the limit of simplistic cases (independent particles, zero density limit), but which allow, by judicious choices of empirical parameters, to reproduce with precision realistic functionals. In this regard, the $\delta^{5/3}$ dependence is added by decomposing the energy per particle into a potential and kinetic part, yielding

$$e_{HM}^N(x, \delta) = t_{HM}^{FG}(n, \delta) + v_{MM}^N(n, \delta), \quad (1.37)$$

where v_{MM}^N is the potential energy per particle expressed as a Taylor expansion in the parameter x at $n = n_{sat}$,

$$v_{MM}^N(n, \delta) = \sum_{\alpha \geq 0}^{N}(v_\alpha^{is} + \delta^2 v_\alpha^{iv})\frac{x^\alpha}{\alpha!}. \quad (1.38)$$

The quadratic approximation for the isospin dependence of the potential energy has been made in Eq. (1.38), as suggested by microscopic calculations in [Vid+09]. The coefficients v_α^{is} and v_α^{iv} are mapped to the empirical parameters following

$$v_\alpha^{is} = \left.\frac{\partial^\alpha e_{HM}}{\partial x^\alpha}\right|_{n=n_{sat},\delta=0} \quad \text{and} \quad v_\alpha^{iv} = \left.\frac{\partial^\alpha e_{HM}^{sym}}{\partial x^\alpha}\right|_{n=n_{sat},\delta=0}, \quad (1.39)$$

yielding the isoscalar parameters:

$$v_0^{is} = E_{sat} - t_{sat}^{FG}(1 + \kappa_{sat}), \quad (1.40)$$

$$v_1^{is} = -t_{sat}^{FG}(2 + 5\kappa_{sat}), \quad (1.41)$$

$$v_2^{is} = K_{sat} - 2t_{sat}^{FG}(-1 + 5\kappa_{sat}), \quad (1.42)$$

$$v_3^{is} = Q_{sat} - 2t_{sat}^{FG}(4 - 5\kappa_{sat}), \quad (1.43)$$

$$v_4^{is} = Z_{sat} - 8t_{sat}^{FG}(-7 + 5\kappa_{sat}), \quad (1.44)$$

and isovector parameters:

$$v_0^{iv} = E_{sym} - \frac{5}{9}t_{sat}^{FG}[1 + (\kappa_{sat} + 3\kappa_{sym})], \tag{1.45}$$

$$v_1^{iv} = L_{sym} - \frac{5}{9}t_{sat}^{FG}[2 + 5(\kappa_{sat} + 3\kappa_{sym})], \tag{1.46}$$

$$v_2^{iv} = K_{sym} - \frac{10}{9}t_{sat}^{FG}[-1 + 5(\kappa_{sat} + 3\kappa_{sym})], \tag{1.47}$$

$$v_3^{iv} = Q_{sym} - \frac{10}{9}t_{sat}^{FG}[4 - 5(\kappa_{sat} + 3\kappa_{sym})], \tag{1.48}$$

$$v_4^{iv} = Z_{sym} - \frac{40}{9}t_{sat}^{FG}[-7 + 5(\kappa_{sat} + 3\kappa_{sym})], \tag{1.49}$$

Let us notice from Eq. (1.38) that the energy per particle does not converge to zero at zero density. This artifact, arising from the nature of the series expansion, can be fixed by introducing an exponential correction $u_\alpha^N(x)$ in the potential energy,

$$v_{MM}^N(n, \delta) = \sum_{\alpha \geq 0}^N (v_\alpha^{is} + \delta^2 v_\alpha^{iv})\frac{x^\alpha}{\alpha!}u_\alpha^N(x), \tag{1.50}$$

the expression of which is

$$u_\alpha^N(x) = 1 - (-3x)^{N+1-\alpha}\exp(-b(1 + 3x)), \tag{1.51}$$

where we have introduced an extra low-density parameter b. It was shown in [Ant+19] that for most applications this parameter can be fixed to a constant, $b = 10\ln(2)$.

Let us now turn to the derivatives of the energy. The expression of the symmetry energy, Eq. (1.31), reads

$$e_{HM}^{sym}(n) = \frac{5}{9}t_{sat}^{FG}(1 + 3x)^{2/3}[1 + (\kappa_{sat} + 3\kappa_{sym})(1 + 3x)] + \sum_{\alpha \geq 0}^N v_\alpha^{iv}\frac{x^\alpha}{\alpha!}u_\alpha^N(x). \tag{1.52}$$

For the chemical potential, we have

$$\mu_{HM,q}(n, \delta) = e_{HM}^N + \frac{1 + 3x}{3}\left(\frac{\partial e_{HM}^N}{\partial x}\right)_\delta + (\tau_3 - \delta)\left(\frac{\partial e_{HM}^N}{\partial \delta}\right)_x + m_q c^2, \tag{1.53}$$

The complete analytical expression of $\mu_{HM,q}$ is given in Appendix B. Finally, the pressure can be calculated through

$$P_{HM} = \sum_{q=n,p} n_q(\mu_{HM,q}(n, \delta) - m_q c^2) - n e_{HM}^N(n, \delta). \tag{1.54}$$

There are two main advantages that come with the metamodeling technique. Firstly, It is flexible enough to reproduce the different existing energy functional of nuclear matter with very good accuracy up to $n \approx 2 - 3n_{sat}$, and even higher densities with a proper redefinition of the third and fourth order parameters [MHG18a]. Since very often the parameters of the model to be mimicked do not coincide with the empirical parameters, we derive the latter by calculating the derivatives of the energy per particle
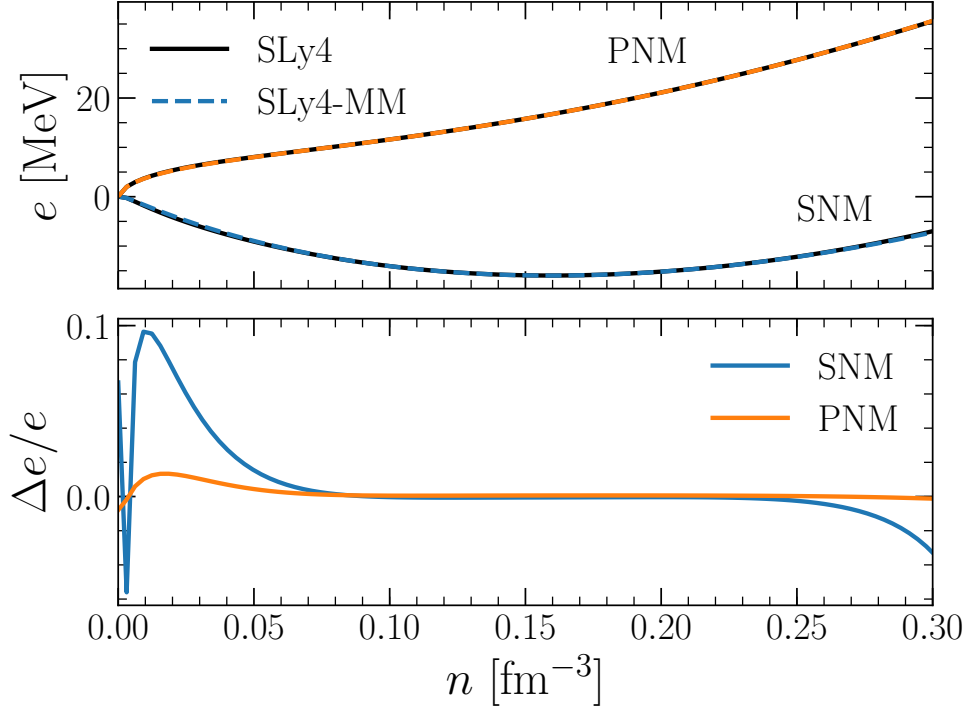
Figure 1.4: Energy per nucleon as a function of density for symmetric nuclear matter, $\delta = 0$, and pure neutron matter, $\delta = 1$ (upper panel), and the associated relative error $\Delta e/e = (e_{MM} - e)/e$ (lower panel) for the SLy4 functional, with $N = 4$ for the metamodel. In the top panel, black solid lines (dashed lines) correspond to the calculation with the exact functional (metamodel).

in nuclear matter at saturation density, following Eq. (1.39). In Fig. 1.4 is demonstrated the accuracy of the metamodeling technique for the SLy4 [Cha+98] functional with a Taylor expansion order $N = 4$. In the top panel, the energy per nucleon is calculated using the metamodeling technique (dashed lines) and the exact functional (black solid lines). A tiny deviation is observed at low density for the SNM, but overall a very good agreement is observed between the metamodel (labeled "SLy4-MM") and the exact functional (labeled "SLy4"). In the lower panel the relative error is represented for SNM and PNM. We can see that the error goes up to 10% for SNM at $n \approx 0.01$ fm^{-3} and rapidly drops to 0% at $n \approx 0.07$ fm^{-3}. At $n \approx 2n_{sat}$, a deviation appears due the extrapolation far from the saturation point. The deviation at low density can be reduced by adjusting the parameter b entering the low-density correction, Eq. (1.51) [Ant+19]. However, this small deviation is not expected to cause any issue for the determination of the inner crust ground state. Indeed, the relative error for PNM is lower that 2% at most, and, in the inner crust, the matter inside nuclei is very neutron rich and the ambient nucleon gas is exclusively constituted of free neutrons. This ability of mimicking existing realistic functionals will allow us to easily compare predictions of astrophysical

observables of different popular models.

Another asset of the metamodeling technique is that no correlation is assumed a priori among the empirical parameters due to the nature of the series expansion. Therefore, all density dependences of the nuclear EoS can be explored. In addition, it allows us to vary each empirical parameter independently of the others to carry out complete statistical analysis using Bayesian inference.

1.2.1.2 From homogeneous nuclear matter to finite nuclei in the CLD approximation

We now turn to the modeling of the energy of clusters present in the inner crust of cold neutron stars. We propose to extend the metamodeling of infinite nuclear matter to nuclei in order to take into account their surface properties, within the CLD approximation, originally introduced in [BBP71]. This approach is expected to be less accurate than microscopic Hartree-Fock (HF) [NV73] or (ETF) [Ons+08] calculations since quantum effects are neglected, though it proved its quality in the past by giving surprisingly good results, see for example [BBP71; LS91; DH00; DH01]. In particular, it appears that most of the macroscopic observables related to neutron stars, such as masses and radii, are not very sensitive to the crust composition, thus a qualitative evaluation of it is sufficient in that case. The compressible liquid drop model (CLDM) comes with multiple advantages. It is very fast from the computational point of view since the energy does not require to be integrated all along the cell volume. For this reason, it is powerful for complete statistical analyses such as the one presented in the next chapter. It is also a model that is flexible, giving us the opportunity to account for different geometries for example, as we consider in 1.2.5. Last but not least, because of the artificial decomposition of the nuclear cluster as a bulk term, a surface term, and a Coulomb term, we are able to identify the contributions of the different terms. For all these reasons, the CLDM is considered as a suitable alternative to semiclassical ETF and microscopic HF treatments, that additionally does not suffer from technical complications such as the definition of boundary conditions [NS09].

In the CLD approximation, the energy of the cluster reads

$$E_{cl} = e_{HM}(n_0, I)A + E_{surf} + E_{Coul}, \qquad (1.55)$$

where E_{surf} represents the nuclear surface energy, and E_{Coul} is the Coulomb energy, including the lattice correction and finite-size effects, written as follows in the WS approximation,

$$E_{Coul} = \frac{3}{5}\frac{e^2}{r_0^2}\eta_{Coul}(u)\frac{Z^2}{A^{1/3}} = \frac{3}{20}\frac{e^2}{r_0^2}\eta_{Coul}(u)A^{5/3}(1-I)^2, \qquad (1.56)$$

with

$$\eta_{Coul}(u) = 1 - \frac{3}{2}u^{1/3} + \frac{1}{2}u, \qquad (1.57)$$

a function of the volume fraction $u = n_e/n_{0,p}$, with $n_{0,p} = n_0(1-I)/2$ the average proton density inside cluster. Let us notice that, the factor $3/5 \times 3/2 = 9/10$ entering the lattice term can be replaced by the Mandelung constant for a body-centered cubic

lattice, $C_M = 0.895929255682$ (see Table 2.4 of [HPY07]).

The bulk term is taken from the metamodel, keeping the same empirical parameters as for the calculation of the neutron gas energy, thus insuring consistency between the crust and the core treatment. The bulk energy is evaluated at n_0, the average density inside the cluster, and I, its global asymmetry.

Let us now turn to the expression of the nuclear surface energy. Assuming that clusters are spherical, it is given by

$$E_{surf} = 4\pi r_0^2 A^{2/3}\sigma, \tag{1.58}$$

where $r_0 = (4\pi n_0/3)^{-1/3}$ is related to the cluster density n_0, and σ is the nuclear surface tension. The simplest parametrization of the surface tension one could use is a constant, $\sigma \approx 1.03$ MeV/fm^2, as in the liquid drop model. However, clusters in the inner crust are expected to be very neutron rich and it appears evident that the surface tension of very asymmetric nuclei should be different to that of symmetric nuclei. In addition, it does not account for the interaction of the nuclear surface with the outside neutron gas, yielding $\sigma \to 0$ as $I \to 1$. This leads us to consider another parametrization for σ which would depend on the asymmetry I and consider the interaction with the gas. It should be mentioned that the exact value of $\sigma(I)$ is model dependent, and the uncertainty is particularly important for extreme isospin values encountered in the inner crust. Indeed, no experimental data exist on the surface energy of nuclei beyond the dripline, which is in-medium modified by the presence of the neutron gas [DHM00]. We use the expression originally proposed by Ravenhall *et al.* [RPL83] on the basis of TF calculations at extreme isospin ratios, and later employed in different works on neutron star crust and supernovae modeling within the CLD approximation [LS91; NGL12; LRP93]:

$$\sigma(I) = \sigma_0 \frac{2^{p+1} + b_s}{Y_p^{-p} + b_s + (1 - Y_p)^{-p}}, \tag{1.59}$$

with $\boldsymbol{S} = \{\sigma_0, b_s, p\}$ the parameter space associated to the surface energy. The parameter $\sigma_0 = \sigma(I = 0)$ represents the surface tension of symmetric nuclei, and b_s and p are the parameters that govern the isospin dependence of the surface tension. The proton fraction is related to the asymmetry inside the cluster via $Y_p = (1 - I)/2$. Following [NGL12], we add a curvature term with the aim of having a better description of the nuclear surface and so of the composition of the inner crust in the ground state. For spherical clusters, the curvature energy reads

$$E_{curv} = 8\pi r_0 A^{1/3}\sigma_c, \tag{1.60}$$

where σ_c is the curvature tension related to the surface tension σ, Eq. (1.59),

$$\sigma_c = \sigma \frac{\sigma_{0,c}}{\sigma_0}\alpha(\beta - Y_p), \tag{1.61}$$

with $\alpha = 5.5$ as in [NGL12]. With the addition of the curvature energy comes two parameters added as extra dimensions to the surface parameter space, $\boldsymbol{S} = \{\sigma_0, b_s, \sigma_{0,c}, \beta, p\}$. For a given model of uniform matter, that is each given set of empirical parameters, the first four parameters can be fitted to experimental masses from the AME2016 [Hua+17]
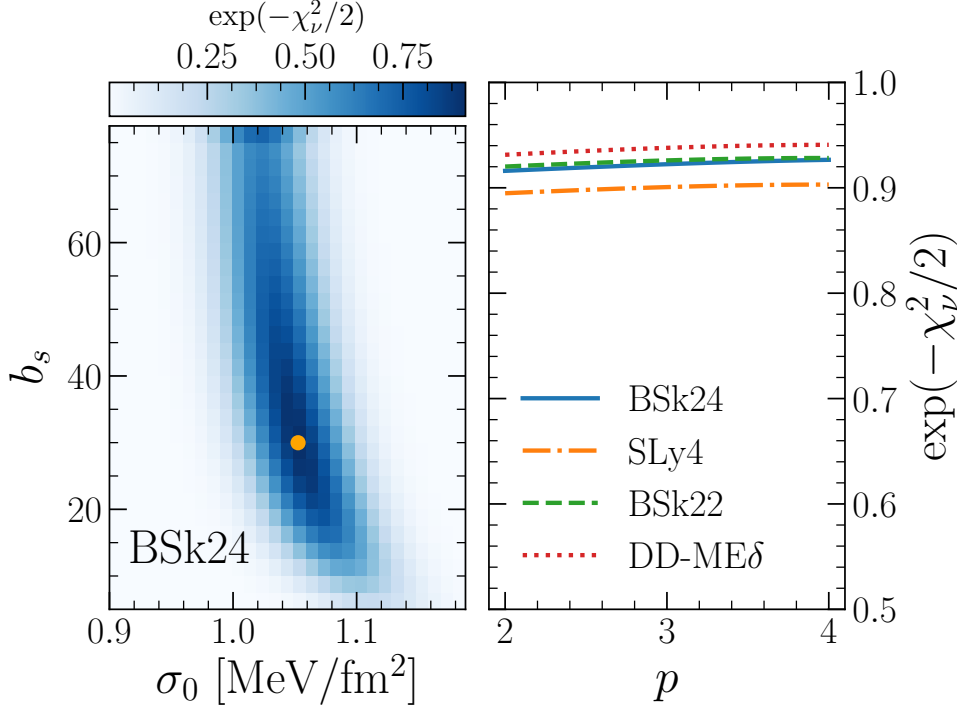
Figure 1.5: Left: Goodness of fit (color scale) as described by the reduced χ^2, in the space of the surface parameters (σ_0, b_s) for the BSk24 CLDM with fixed value of the p parameter, $p = 3$, for optimized curvature parameters σ_{0c} and β. The orange point indicates the optimal value. Right: Weight $\exp(-\chi_\nu^2/2)$ as a function of the parameter p, calculated for the optimal value of $(\sigma_0, b_s, \sigma_{0c}, \beta)$, for the selected CLDM: BSk24, SLy4, BSk22, and DD-MEδ.

for a fixed value of the parameter p. The quality of reproduction of the experimental nuclear binding energy E_{AME2016} is measured by the reduced χ^2, defined as

$$\chi_\nu^2 = \frac{\chi^2}{\nu} = \frac{1}{\nu} \sum_i \left(\frac{E_{cl}^{(i)}/A^{(i)} - E_{\mathrm{AME2016}}^{(i)}/A^{(i)}}{\sigma^{(i)}} \right)^2 , \tag{1.62}$$

where ν is the number of degrees of freedom, and the denominator corresponds to the systematic theoretical error, 0.1 MeV/A, such as to have $\chi_{min}^2 \approx 1$ over the parameter space sample [DNR14].

This point can be clearly understood by inspection of the left panel of Fig. 1.5, which shows the value of the weight function $\exp(-\chi_\nu^2/2)$, that is the goodness of fit, in the (σ_0, b_s) plane, for the BSk24 CLDM with $p = 3$, and curvature parameters already adjusted to experimental data. It is seen that the weight function is strongly peaked to the orange point, which indicates the optimal value for the parameters σ_0 and b_s. Conversely, we observe in the right panel of Fig. 1.5 that the error estimator χ_ν^2 is insensitive to the choice of the parameter p in a range going from 2 to 4, for four representative
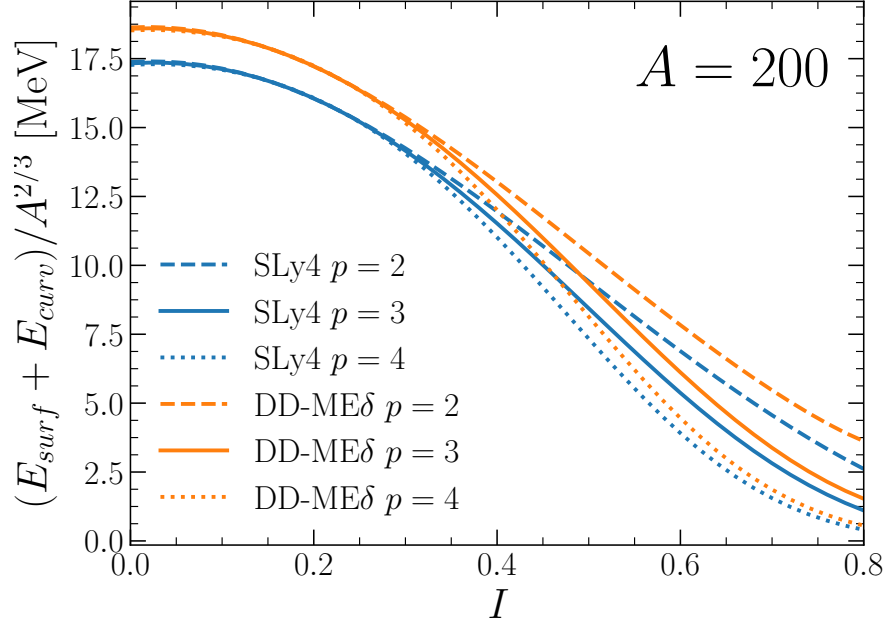
Figure 1.6: Variation with cluster asymmetry I of surface plus curvature energy per surface nucleon along the isobaric chain $A = 200$ for SLy4 [Cha+98] and DD-MEδ [Roc+11] CLDM at three selected values of parameter p: $p = 2$ (dashed lines), $p = 3$ (solid lines), and $p = 4$ (dotted lines).

functionals. This is understood from the fact that p modifies the asymmetry dependence of the surface energy only for extreme values of I where nuclear data are not available. This parameter is therefore not adjusted as the other parameters, in order to avoid poor extrapolations of σ. The value of p is selected around $p = 3$, which is the value used in the popular Lattimer and Swesty EoS [LS91]. We show in Fig. 1.6 the surface plus curvature energy per surface nucleon as a function of the asymmetry inside the cluster for two popular models, SLy4 [Cha+98] and DD-MEδ [Roc+11], in the CLD approximation. Different values for the parameter p are displayed in that figure. It is seen that p determines the behavior of the surface tension for extreme isospin values, and cannot be accessed from experimental nuclear physics data. In addition, since the selected popular models contain parameters that are adjusted to the same data, we cannot cannot consider their predictions at high isospin as reliable. For these reasons, we will keep p as a free parameter. In particular, from $I \approx 0.3$, we observe that a larger value of p leads to larger surface energy at fixed asymmetry. The model dependence of the surface tension is also observed in that figure and is particularly highlighted at low asymmetry where experimental measurements can still be performed.

Finally, we recall the final expression for the cluster binding energy in the CLD

approximation,

$$\begin{aligned}
E_{cl}(A, I, n_0, n_e) = \quad & e_{HM}(n_0, I)A \\
& +4\pi r_0^2 A^{2/3}\sigma(I) + 8\pi r_0 A^{1/3}\sigma_c(I) \\
& +\frac{3}{20}\frac{e^2}{r_0^2}\eta_{Coul}(I, n_0, n_e)A^{5/3}(1 - I)^2.
\end{aligned} \tag{1.63}$$

Let us notice that the energy does not depend on the neutron gas density via the surface term, as in [BBP71]. This dependence is in fact implicitly accounted for in the chosen parametrization of the surface tension, suggested from microscopic calculations in the WS cell [RPL83].

1.2.2 Variational formalism

The variational method for the calculation of the inner crust ground state with the CLDM was introduced in the pioneering work of BBP in their classical paper [BBP71]. Since then, huge progress has been made in constraining the nucleon-nucleon (NN) effective interaction. For this reason, subsequent works using the same formalism with CLDM based on more realistic nuclear functionals followed. For instance we can mention the popular calculations of Douchin and Haensel (DH) [DH00; DHM00] with the SLy4 effective force [Cha+98]. Following those works, we use the same variational method as BBP, and we present it in the following.

Using the Lagrange multipliers method, the ground state of the inner crust is obtained by minimizing the zero-temperature free energy density of the WS cell at fixed baryon density n_B under the condition of charge neutrality, $n_e = n_p$. The minimization is carried out with respect to the set of variables A, I, n_0, n_p, and n_g. Let us notice that, in principle, one should minimize the Gibbs free energy at constant pressure, as for the outer crust. However, it would be very heavy from the computational point of view to do so in the free neutron regime. Fortunately, it is demonstrated that the error introduced by minimizing at constant baryon density instead of pressure is negligible [Pea+12]. The auxiliary function to be minimized is defined as

$$\begin{aligned}
\mathcal{L}(A, I, n_0, n_p, n_g) \quad = \quad & \frac{E_{WS}}{V_{WS}} - \mu n_B \\
= \quad & \frac{E_{cl}}{V_{WS}} + \varepsilon_e + \left(1 - \frac{A}{n_0 V_{WS}}\right)\varepsilon_g \\
& +n_p\Delta m_{pn}c^2 - n_B(\mu - m_n c^2),
\end{aligned} \tag{1.64}$$

with $\Delta m_{pn} = m_p - m_n$ the difference between the proton and neutron mass, and μ the Lagrange multiplier.
The volume of the cell can be calculated as

$$V_{WS} = \frac{Z}{n_p} = \frac{A}{n_p}\frac{1 - I}{2}, \tag{1.65}$$

and the baryon density is given by

$$
\begin{aligned}
n_B &= \frac{A_{WS}}{V_{WS}} \\
&= \frac{2n_p}{1-I}\left(1 - \frac{n_g}{n_0}\right) + n_g.
\end{aligned}
$$
(1.66)

Replacing these quantities in Eq. (1.64), it results

$$
\begin{aligned}
\mathcal{L}(A, I, n_0, n_p, n_g) &= \frac{2n_p}{A(1-I)}E_{cl} + \varepsilon_e + \left(1 - \frac{2n_p}{n_0(1-I)}\right)\varepsilon_g + n_p\Delta m_{pn}c^2 \\
&\quad - \frac{2n_p}{1-I}\left(1 - \frac{n_g}{n_0}\right)(\mu - m_nc^2) - n_g(\mu - m_nc^2).
\end{aligned}
$$
(1.67)

Let us first minimize with respect to A:

$$
\begin{aligned}
\left.\frac{\partial\mathcal{L}}{\partial A}\right|_{I,n_0,n_p,n_g} &= 0 \\
\frac{2n_p}{A(1-I)}\frac{\partial E_{cl}}{\partial A} - \frac{2n_p}{A^2(1-I)}E_{cl} &= 0 \\
\frac{\partial E_{cl}}{\partial A} - \frac{E_{cl}}{A} &= 0,
\end{aligned}
$$
(1.68)

which is equivalent to

$$
\frac{\partial(E_{cl}/A)}{\partial A} = 0.
$$
(1.69)

We can go trough this equation using the definition of the cluster energy, Eq. (1.63), yielding

$$
-\frac{1}{3}\times 4\pi r_0^2\sigma A^{-4/3} - \frac{2}{3}\times 8\pi r_0\sigma_c A^{-5/3} + \frac{2}{3}\times\frac{3}{20}\frac{e^2}{r_0}\eta_{Coul}A^{-1/3}(1-I)^2 = 0
$$

$$
4\pi r_0^2\sigma A^{2/3} + 2\times 8\pi r_0\sigma_c A^{1/3} - 2\times\frac{3}{20}\frac{e^2}{r_0}\eta_{Coul}A^{5/3}(1-I)^2 = 0,
$$

or simply,

$$
E_{surf} + 2E_{curv} = 2E_{Coul}.
$$
(1.70)

This equation corresponds to the well-known Baym virial theorem with an additional curvature term with respect to the equation originally found in [BBP71]. It is interesting to notice that only the surface, the curvature, and the Coulomb energy are involved in this first equilibrium condition.

Minimizing with respect to the neutron gas density n_g, one obtains:

$$
\left.\frac{\partial\mathcal{L}}{\partial n_g}\right|_{A,I,n_0,n_p} = 0
$$

$$
\left(1 - \frac{2n_p}{n_0(1-I)}\right)\frac{\partial\varepsilon_g}{\partial n_g} + \frac{2n_p}{n_0(1-I)}(\mu - m_nc^2) - (\mu - m_nc^2) = 0,
$$
(1.71)

giving us the expression of the Lagrange multiplier, which can be identified with the chemical potential of the gas, including the rest mass energy,

$$\mu = \frac{\partial \varepsilon_g}{\partial n_g} + m_n c^2 \equiv \mu_g. \tag{1.72}$$

We now turn to the minimization with respect to average cluster density n_0:

$$\left. \frac{\partial \mathcal{L}}{\partial n_0} \right|_{A,I,n_p,n_g} = 0$$

$$\frac{2n_p}{A(1-I)} \frac{\partial E_{cl}}{\partial n_0} + \frac{2n_p}{n_0^2(1-I)} \varepsilon_g - \frac{2n_p n_g}{n_0^2(1-I)}(\mu - m_n c^2) = 0$$

$$\frac{n_0^2}{A} \frac{\partial E_{cl}}{\partial n_0} - n_g(\mu - m_n c^2) + \varepsilon_g = 0. \tag{1.73}$$

Using well-known thermodynamical relations, we define $P_{cl} \equiv (n_0^2/A)(\partial E_{cl}/\partial n_0)$, and $P_g = n_g(\mu_g - m_n c^2) - \varepsilon_g$. Therefore, Eq. (1.73) simply results in

$$P_{cl} = P_g, \tag{1.74}$$

which can be interpreted as a pressure equilibrium condition between the cluster and the outside neutron gas. We can derive the expression of the cluster pressure from the CLD energy, Eq. (1.63), yielding

$$P_{cl} = P_{HM}(n_0, I) - \frac{2}{3} n_0 \frac{E_{surf}}{A} - \frac{1}{3} n_0 \frac{E_{curv}}{A} + n_0 \frac{E_{coul}(u=0)}{A} \left(\frac{2}{3} + \frac{1}{2} u^{1/3} - \frac{1}{2} u \right). \tag{1.75}$$

The minimization with respect to the global asymmetry inside the cluster I yields

$$\left. \frac{\partial \mathcal{L}}{\partial I} \right|_{A,n_0,n_p,n_g} = 0$$

$$\frac{2n_p}{(1-I)^2} \left(\frac{E_{cl}}{A} + \frac{1-I}{A} \frac{\partial E_{cl}}{\partial I} - \frac{\varepsilon_g}{n_0} - \left(1 - \frac{n_g}{n_0} \right)(\mu - m_n c^2) \right) = 0$$

$$\frac{E_{cl}}{A} + \frac{1-I}{A} \frac{\partial E_{cl}}{\partial I} - \frac{\varepsilon_g}{n_0} - \left(1 - \frac{n_g}{n_0} \right)(\mu - m_n c^2) = 0, \tag{1.76}$$

resulting in

$$\frac{E_{cl}}{A} + \frac{1-I}{A} \frac{\partial E_{cl}}{\partial I} + \frac{P_g}{n_0} = \mu - m_n c^2. \tag{1.77}$$

Due to the presence of the outside neutron gas, the neutron chemical potential of the cluster is modified with respect to the usual expression in the vacuum $\mu_n^{vac} = \partial E_{cl}/\partial N$. We define the neutron and proton chemical potential of the cluster as

$$\mu_p^{cl} = \left. \frac{\partial E_{cl}}{\partial Z} \right|_N + m_p c^2 \quad \text{and} \quad \mu_n^{cl} = \left. \frac{\partial E_{cl}}{\partial N} \right|_Z + \frac{P_g}{n_0} + m_n c^2, \tag{1.78}$$

where the derivatives are taken at constant n_0, n_p, and n_g. Consequently, we can work out Eq. (1.77) to find a chemical equilibrium conditions between the neutrons of the cluster and those of the gas,

$$\mu_n^{cl} = \mu_g. \tag{1.79}$$

Finally, we minimize the auxiliary function, Eq. (1.64) with respect to the proton density n_p inside the WS cell,

$$\left.\frac{\partial \mathcal{L}}{\partial n_p}\right|_{A,I,n_0,n_g} = 0$$

$$\frac{E_{cl}}{A} + \frac{n_p}{A}\frac{\partial E_{cl}}{\partial n_p} + \frac{1-I}{2}\left(\frac{\partial \varepsilon_e}{\partial n_p} + \Delta m_{pn}c^2\right) - \frac{\varepsilon_g}{n_0} - \left(1 - \frac{n_g}{n_0}\right)(\mu - m_n c^2) = 0. \tag{1.80}$$

By identifying common terms with Eq. (1.76), we recover the well-known beta equilibrium condition,

$$\frac{2}{A}\left(\frac{\partial E_{cl}}{\partial I} - \frac{n_p}{1-I}\frac{\partial E_{cl}}{\partial n_p}\right) - \Delta m_{pn}c^2 = \frac{\partial \varepsilon_e}{\partial n_p}, \tag{1.81}$$

or in terms of chemical potentials,

$$\mu_n^{cl} = \mu_p^{cl} + \mu_e + \Delta\mu, \tag{1.82}$$

where $\Delta\mu$ represents the modification due to the excluded-volume interaction with the neutron gas, and the electrostatic interaction between protons in the cluster and the background electrons. It is given by

$$\Delta\mu = \frac{P_g}{n_0} + \frac{2}{A(1-I)}n_p\frac{\partial E_{Coul}}{\partial n_p}. \tag{1.83}$$

One can remark that only the Coulomb energy enters in the derivative with respect to the proton density n_p. This derivative can be evaluated analytically from Eq. (1.56) as

$$\frac{\partial E_{Coul}}{\partial n_p} = \frac{3}{20}\frac{e^2}{r_0^2}A^{5/3}(1-I)\frac{1}{n_0}\left(1 - \left(\frac{2n_p}{n_0(1-I)}\right)^{-2/3}\right). \tag{1.84}$$

Finally, a possible set of mechanical and chemical equilibrium equations is

$$\frac{\partial(E_{cl}/A)}{\partial A} = 0, \tag{1.85}$$

$$\frac{n_0^2}{A}\frac{\partial E_{cl}}{\partial n_0} = P_g(n_g), \tag{1.86}$$

$$\frac{E_{cl}}{A} + \frac{1-I}{A}\frac{\partial E_{cl}}{\partial I} + \frac{P_g(n_g)}{n_0} = \mu_g(n_g) - m_n c^2, \tag{1.87}$$

$$\frac{2}{A}\left(\frac{\partial E_{cl}}{\partial I} - \frac{n_p}{1-I}\frac{\partial E_{cl}}{\partial n_p}\right) - \Delta m_{pn}c^2 = \mu_e(n_p), \tag{1.88}$$

or, equivalently Eqs. (1.70), (1.74), (1.79), and (1.82), respectively. This system of four coupled differential equations can be solved numerically, as explained in 1.2.3.1, in order to obtain the equilibrium composition and so the EoS in the free neutron regime. Let us mention that taking alternatives set of variables leads to the same equilibrium equations [HPY07; Viñ+17].

1.2.3   Results

We now turn to the results of the minimization. The building of the numerical code is presented first and the numerical results, such as the ground-state composition and EoS of the inner crust, afterwards.

1.2.3.1   Numerical code

During the thesis, an open-source C library, NSEoS, has been built in relation to the physics of NS [Car17a]. Here we focus on the numerical methods used to solve the inner crust equilibrium equations in order to estimate the composition and EoS in the free neutron regime. Those methods can be found in the module `crust` of the library.

The ground state of the inner crust at baryon density n_B is determined by solving numerically the system of four coupled differential equations, Eqs. (1.85), (1.86), (1.87), and (1.88). To do so, we use a root-finding algorithm, Broyden's method [Bro65], which is similar to the popular Newton's method. In Broyden's method, the 16 partial derivatives entering the 4×4 Jacobian matrix are replaced with finite differences. While the derivatives can be evaluated analytically from the CLD expressions with ease, using finite differences makes it easier to identify the effect of the different contributions entering the WS cell energy. This point will be covered in greater detail in Chapter 3. The Jacobian matrix is not computed at each iteration but is only evaluated at the first iteration then simply rank-one updated. In order to avoid an unreliable estimation of the equilibrium composition $\{A_{eq}, I_{eq}, n_{0,eq}, n_{p,eq}, n_{g,eq}\}$ due to the accumulation of errors, the maximum number of iterations is fixed to $N_{iter}^{max} = 1000$. In addition, the backstepping technique is employed to avoid nonphysical solutions, such as negative values for A or $|I| > 1$, that could result in errors when reinjected in the equilibrium equations. For instance, if at a given iteration, a spurious value of A is obtained, then we replace it by the previous value A_{old} plus a smaller step $\Delta A' < \Delta A$, until we get a physical value. Finally, let us mention that as for Newton's method, Broyden's method requires an initial guess for the composition.

We proceed as follows. The calculation starts at the neutron drip density n_{ND}. A natural choice for the initial guess is to take the last solution for the ground state of the outer crust, with reasonable values $A_{guess} = 36$, $I_{guess} = 0.3$, $n_{0,guess} = 0.15$ fm^{-3}, and $n_{g,guess} = 10^{-6}$ fm^{-3}. Then, the proton density is calculated as

$$n_{p,guess} = (n_B - n_{g,guess}) \left(1 - \frac{n_{g,guess}}{n_{0,guess}} \right) \frac{1 - I_{guess}}{2}. \tag{1.89}$$

To continue, we make use of Broyden's method described previously to evaluate the equilibrium composition A_{eq}, I_{eq}, $n_{0,eq}$, and $n_{g,eq}$. The process is then repeated with n_B increasing in steps of $\Delta n_B = 10^{-4}$ fm^{-3}. At each new value of n_B, the guess is updated to coincide with the last equilibrium composition, ensuring faster convergence of the algorithm. At a reasonable value of baryon density, $n_B = 10^{-3}$ fm^{-3}, we start to check whether it is beneficial or not to have a phase transition from clusterized matter to homogeneous matter. The calculation is stopped once the crust-core (CC) interface is reached, approximately for $n_B \approx n_{sat}/2$. The CC transition from the crust side is discussed in details in 1.2.6.
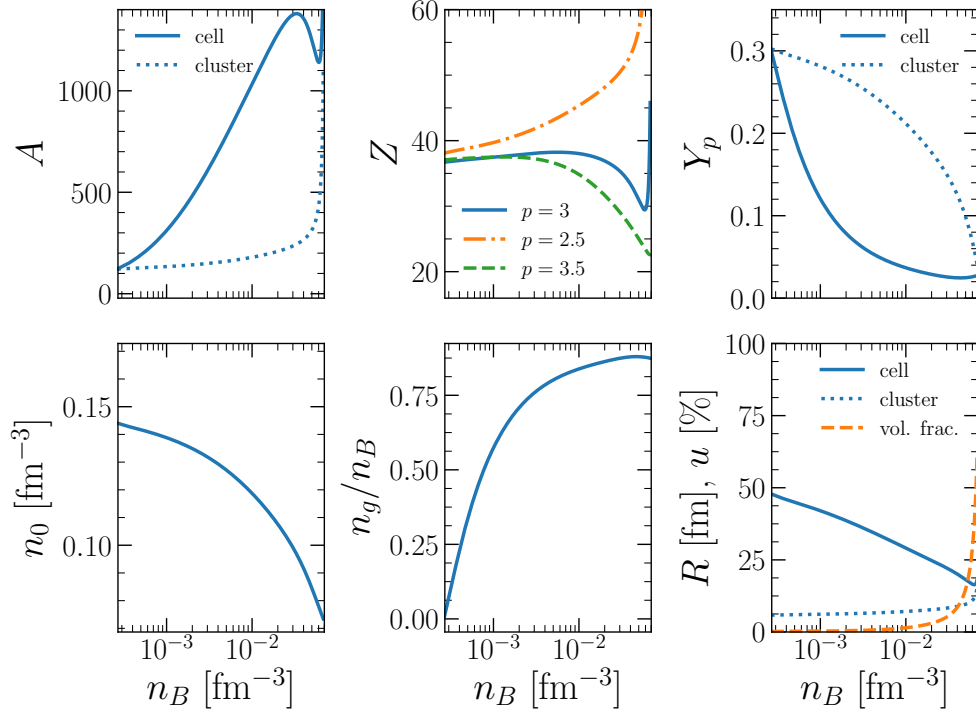
Figure 1.7: Variation with baryon density n_B of the equilibrium value of mass number A, atomic number Z, proton fraction Y_p, average cluster density n_0, neutron gas density to baryon density ratio n_g/n_B, radius R, and volume fraction u in the inner crust, for BSk24 CLDM with $p = 3$. Solid (dotted) lines correspond to the results for the cell (cluster). In the upper-mid panel, three values of the parameter p are selected: $p = 2.5$, $p = 3$, and $p = 3.5$.

1.2.3.2   Equilibrium composition

Fig. 1.7 shows the evolution with baryon density n_B of the equilibrium composition of the inner crust. The empirical parameters entering the bulk part of the CLDM energy correspond to the BSk24 effective force [GCP13], and the surface parameter p is fixed at the educated value $p = 3$, which appears to be a reasonable value for Skyrme-type functionals, as we will discuss in 1.2.6.

It is found that the number of nucleons inside the cluster A as well as inside the WS cell A_{WS} monotonously increases with increasing density, going up to ≈ 700 and ≈ 1500, respectively, at high density. The number of free neutrons $N_g = A_{WS} - A$ can also be inferred. It is obviously equal to zero at the neutron drip density, since $A = A_{WS}$. The behavior of A and A_{WS} is in agreement with other CLD calculations, such as the one of BBP [BBP71] and that of DH [DH00]. The later study reports a value of $A \approx 600$ at the CC interface, using the SLy4 functional, while BBP report a much higher value of $A = 7840$ (see their Table 1). Let us notice that the presence of such heavy spherical nuclei at the crust bottom raises the question of stability with respect to deformation and

fission, as explained in [DH00]. In particular, nuclear fission, the approximate condition for which is $R_p/R_{WS} \gtrsim 1/2$ [BW39; PR95], R_p being the proton radius, could occur at high density. In 1.2.5, we show that considering nonspherical geometries can stabilize the large clusters. It is important to stress that the composition, in particular A and Z, is very sensitive to the isospin dependence of the surface tension at extreme isospin ratios.

The variation with baryon density of the equilibrium value of Z is also represented in Fig. 1.7. We find $Z \approx 40$ all along the inner crust with $p = 3$, which is in a surprisingly good agreement with microscopic results. In particular, in the early work of Negele and Vautherin (NV) [NV73] is derived a set of nonlinear equations for the single particle wave functions of nucleons, using the density-matrix expansion for a realistic NN interaction. NV observed a predominance of $Z = 40$ at low density, and $Z = 50$ at high density. Subsequent works within the semiclassical ETF [Gor+05] and finite-temperature extended Thomas-Fermi plus Strutinsky integral (TETFSI) [Ons+08; Pea+18] also predict $Z = 40$ in the inner crust. As far as CLD calculations are concerned, DH find that the equilibrium value of Z is almost constant in the vicinity of ≈ 40 throughout the inner crust, whereas BBP find monotonically increasing values of Z. Once again, it should be stress out that Z is very sensitive to the isospin dependence of the surface tension. In particular, it is observed by varying the parameter p that governs the behavior of the surface tension at extreme isospin values. We can see that a lower surface tension, $p = 3.5$, favors smaller atomic number Z, and in general lighter clusters, unlike $p = 2.5$ that leads to heavier clusters.

As in the outer crust, we find that the proton fraction inside the cell Y_p continuously decreases in the free neutron regime, dropping from ≈ 0.3 at the neutron drip point to ≈ 0.03 at the edge of the crust. With increasing density, clusters also becomes more and more asymmetric, I going up to ≈ 0.85 in the bottom layers.

Clusters are found to be more and more dilute with n_B increasing. At the neutron drip density, we get $n_0 \approx 0.145$ fm^{-3}, which is close to the saturation density of SNM of the BSk24 functional, $n_{sat} = 0.1578$ fm^{-3}. At the CC interface, the cluster density is as low as $n_0 \approx 0.07$ fm^{-3}, which is comparable to the neutron gas density, represented is the lower-mid panel. It is seen that the ratio n_g/n_B rapidly reaches $\approx 75\%$ at $n_B = 2 \times 10^{-3}$ fm^{-3} then stays approximately constant at higher densities.

The equilibrium radius of the spherical WS cell R_{WS} and of the spherical cluster R_{cl} are also displayed in Fig. 1.7. As DH, we observe that R_{WS} monotonically decreases unlike R_{cl} that slowly increases with increasing depth. Therefore, nuclei becomes closer and closer, eventually becoming close enough to touch each other at some point, creating a very large cluster, ultimately leading to homogeneous matter. We can also understand this by calculating the volume fraction $u = (R_{cl}/R_{WS})^3 = 2n_p/(n_0(1 - I))$ (orange dashed line). We find that the cluster fills up to 60% of the WS cell volume at the CC interface. This feature combined with the virial theorem, Eq. (1.70), outlines the fact that lattice and finite-size contributions to the Coulomb energy are crucial for the determination of the ground state of the inner crust.
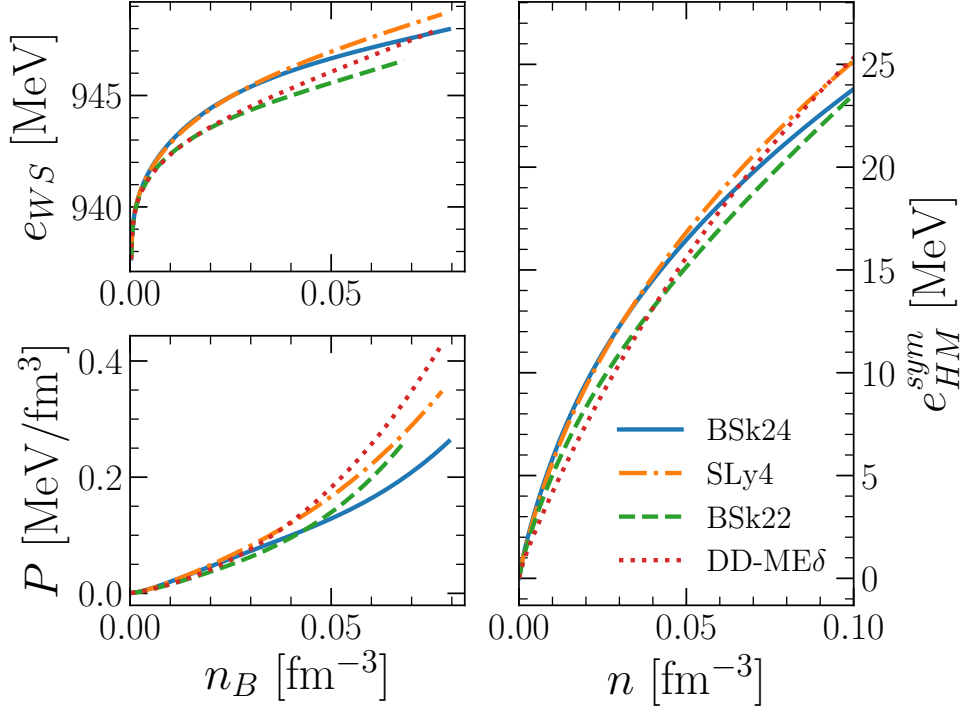
Figure 1.8: Left: Equilibrium value of the energy per nucleon of the WS cell $e_{WS} = E_{WS}/A_{WS}$ (upper panel), and pressure P (lower panel) as a function of the baryon density n_B in the inner crust for four selected CLDM: BSk24, SLy4, BSk26, and DD-MEδ. Right: Variation of symmetry energy e_{HM}^{sym}, Eq. (1.52), with density n, for the four models.

1.2.3.3 Equation of state

In Fig. 1.8, the equilibrium energy per nucleon of the WS cell $e_{WS} = E_{WS}/A_{WS}$ is plotted as a function of the baryon density n_B for different CLDM, based on the relativistic model DD-MEδ, and on three Skyrme-type interactions: SLy4, BSk22, and BSk24. It is observed that e_{WS} depends on the nuclear model. In particular, it is known to be correlated with the symmetry energy, with higher symmetry leading to higher e_{WS}, at subnuclear densities [Pea+18]. This trend can be verified by looking at the right panel of the figure, that shows the symmetry energy, Eq. (1.52), as a function of density for the four models considered here.

Fig. 1.8 also shows the variation with the baryon density of pressure P, commonly referred to as the EoS, in the inner crust. We demonstrate in Appendix C that the total pressure, defined by the first law of thermodynamics as

$$P = n_B^2 \frac{de_{WS}}{dn_B}, \tag{1.90}$$

can be expressed as

$$P = P_g + P_e + P_L, \tag{1.91}$$

at the equilibrium composition, where P_L is the lattice contribution to the total pressure. Using this expression rather than finite differences to estimate the derivative, Eq. (1.90), is more reliable and has the advantage to be faster from the computational point of view. In addition, it allows identifying the different contributions to the pressure. In the inner crust, the pressure is no longer dominated by the relativistic electron gas but by the ambient neutron gas [Car17b]. At subnuclear densities, we observe that the EoS is also correlated with the symmetry energy. In particular, the higher the empirical parameter E_{sym}, which is the symmetry energy at $n = n_{sat}$, the stiffer is the EoS. The value of E_{sym} for each model is reported in Table 1.3.

1.2.4 Strutinsky shell corrections to the CLD energy

In the CLD approximation, shell effects, which are known since the pioneering work of BPS [BPS71] to be essential to correctly evaluate the outer-crust composition at zero temperature, are lost. In this same limit microscopic calculations have shown that the neutron shell effects become vanishingly small beyond the neutron drip point [Cha06; Cha+07], but proton shell effects persist in the inner crust.

There are different ways to include shell corrections to the CLD energy. The simplest approach is to use an empirical formula, such as the one proposed by Myers and Swiatecki [MS66] which is accurate for reproducing masses of laboratory nuclei. However, a limitation of their method is that it requires a priori a list of magic numbers, which are obviously not known in the regime of the inner crust. Let us recall that NV find a persistence of $Z = 40$ while it is not considered as a magic number in ordinary nuclei. A more suitable alternative is to calculate shell corrections using the Strutinsky method [Ons+08]. Fortunately, Strutinsky shell corrections were calculated for modern BSk functionals, and are tabulated in [Pea+18] (see Supplementary data). We therefore add these corrections on top of the CLD energy for the corresponding models.

We now turn to the numerical method, proceeding as follows. The energy density is the quantity to be minimized at constant baryon density for a fixed number of protons inside the WS cell. We derive the system of equilibrium equations using the Lagrange multipliers method, as in 1.2.2, yielding

$$\frac{\partial E_{cl}}{\partial A} - \frac{E_{cl}}{A} = \frac{1-I}{2}\left(\mu_e(n_p) + \frac{2np}{A(1-I)}\frac{\partial E_{cl}}{\partial n_p} - \frac{2}{A}\frac{\partial E_{cl}}{\partial I} + \Delta m_{pn}c^2\right), \tag{1.92}$$

$$\frac{\partial E_{cl}}{\partial A} + \frac{1-I}{A}\frac{\partial E_{cl}}{\partial I} + \frac{P_g(n_g)}{n_0} = \mu_g(n_g) - m_n c^2, \tag{1.93}$$

$$\frac{n_0^2}{A}\frac{\partial E_{cl}}{\partial n_0} = P_g(n_g). \tag{1.94}$$

Let us notice that beta equilibrium is not imposed anymore since Z is fixed, causing a modification of Eq. (1.92) with respect to the virial theorem with curvature term, Eq. (1.85). For a given n_B, the minimization is carried out for each tabulated Z using
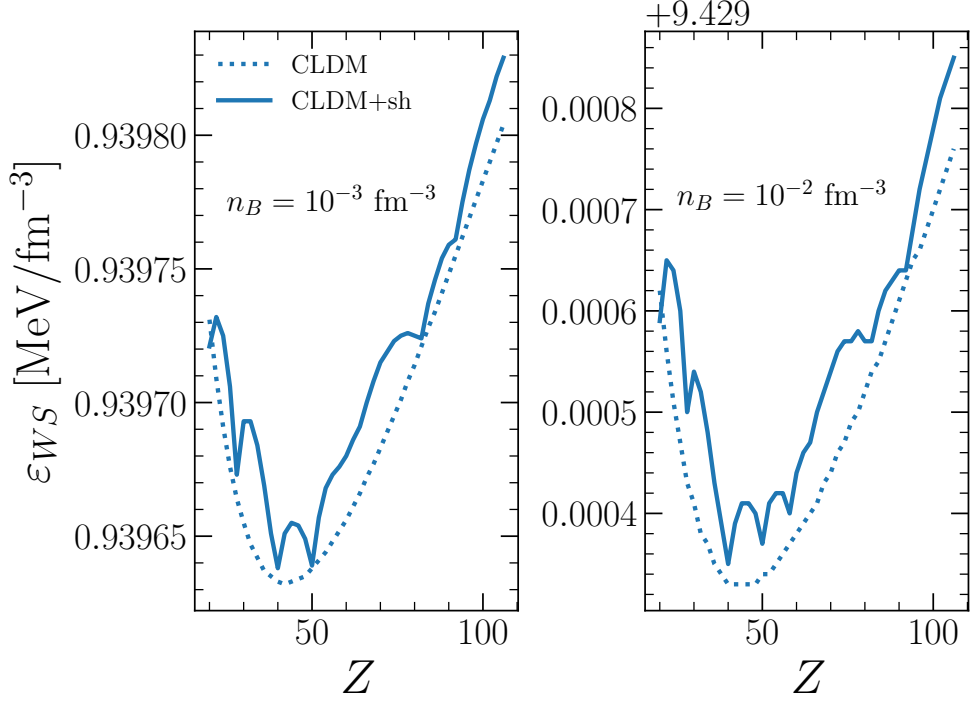
Figure 1.9: WS cell energy density as a function of number of protons Z at two different densities in the inner crust for BSk24 CLDM with (solid lines) and without (dotted lines) Strutinsky shell corrections on top of the CLD energy. In the right panel, the constant value 9.429 MeV/fm^3 is subtracted from the WS cell energy density.

Broyden's method. The proton Strutinsky shell corrections are then added perturbatively to the CLD energy by interpolation among values of the table, which gives the shell energy per nucleon for a given (n_B, Z). The WS energy density including shell corrections thus reads

$$\varepsilon_{WS}(n_B, Z) = \varepsilon_{WS}^{CLD}(n_B, Z) + n_B \Delta e_{sh}(n_B, Z), \qquad (1.95)$$

where ε_{WS}^{CLD} is the smooth part of the WS energy density at the equilibrium, and Δe_{sh} is the interpolated shell energy per nucleon. The value of Z that minimizes the energy density of matter is naturally defined as the equilibrium value.

Fig. 1.9 shows the variation of the WS energy density as a function of Z at two selected values of baryon density n_B, for BSk24 CLDM. As expected, the pure CLD results, represented in dotted lines, are close to those including Strutinsky shell corrections, represented in solid lines, for closed-shell configurations, while remarkable differences exist for all other values of Z. This feature confirms the importance of a proper account of the shell structure. At $n_B = 10^{-3}$ fm^{-3}, a competition between $Z = 40$ and $Z = 50$ can be observed, with $Z = 40$ being slightly favored. However, it should be stressed that the difference in energy density is about 10^{-6} MeV/fm^{-3}, which is expected to be lower
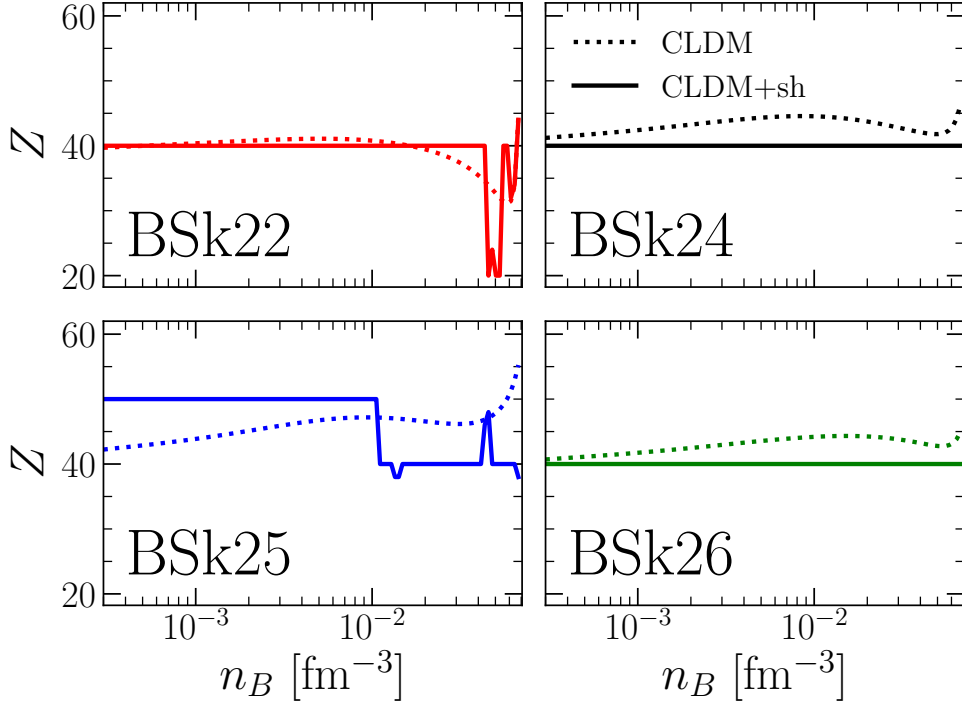
Figure 1.10: Equilibrium value of Z as a function of baryon density n_B in the inner crust for BSk22, BSk24, BSk25, and BSk26 CLDM with (solid lines) and without (dotted lines) Strutinsky shell corrections on top of the CLD energy.

than the precision reached by our modeling. It is observed that the shell closure $Z = 40$ is also favored over $Z = 50$ and $Z = 58$ at $n_B = 10^{-2}$ fm^{-3}.

Our results for the equilibrium value of Z in the inner crust using BSk22, BSk24, BSk25, and BSk26 CLDM with (solid lines) and without (dotted lines) Strutinsky shell corrections can be seen in Fig. 1.10. It can be observed that magic numbers are recovered when shell corrections are added on top of the CLD energy. In particular, remarkable stability at $Z = 40$ is seen for BSk24 and BSk26, as well as $Z = 20$ and $Z = 40$ for BSk22, in a very good agreement with Fig. 12 of [Pea+18]. A small difference only appears for the BSk25 model, reflecting the limitations of the CLD approach. For this functional, after the plateau at $Z = 50$, also obtained with extended Thomas-Fermi plus Strutinsky integral (ETFSI) calculations of [Pea+18] for the same functional, the equilibrium number of protons drops to $Z = 40$ in our case, instead of increasing as in [Pea+18]. However, we stress that the authors find a second minimum at $Z = 40$, and the energy difference between the two minima is of the order of 10^{-3} MeV [Pea+19].

Let us recall that surface and curvature parameters σ_0, b_s, σ_{0c}, and β are so far fitted to experimental masses of nearly symmetric nuclei from the AME2016 [Hua+17] with a fixed value of the parameter p that governs the behavior of the surface tension at extreme isospin values. Therefore the shell energy is implicitly accounted for in

the surface tension by underestimating the value of σ_0, that is the surface tension of symmetric nuclei. This results in predicting slightly overbound nuclei with the CLD approach, but overall in a better description of spherical nuclei. However, we face an issue when adding Strutinsky shell corrections to the CLD energy, since we do not want to double-count the shell energy. To address this problem, we fit the surface and curvature parameters to the ETF results for each functional [Pea19], keeping the parameter p fixed to the value $p = 3$ [Car+20], which gives an accurate reproduction of the CC transition points obtained in [Pea+19].

1.2.5   Nonspherical pasta phases

We have assumed so far that the inner crust only consists of spherical clusters. However, at high density just before the CC transition, nuclei are almost close enough to touch each other, and thus the lattice energy significantly reduces the Coulomb energy. Consequently, matter could in principle arrange itself into exotic structures, sometimes referred to as nuclear "pasta". In particular, from the density at which the volume fraction exceeds $1/2$, it is expected that nuclei turn inside out, therefore forming neutron bubbles immersed in a proton-rich phase (the former cluster) [BBP71]. Furthermore, molecular dynamics simulations, in which a large number of interacting nucleons are let evolving in a very large box, predict the appearance of complex structures for $Y_p \approx 0.1$, which is comparable to the typical value in the bottom layers of the inner crust of neutron stars [Wat+03]. It should be stressed that these exotic phases of matter could constitute half of the crust mass [LRP93]. It is therefore straightforward to imagine that various astrophysical phenomena, such as the cooling process by neutrino emission, can be affected by their existence [WM11].

One of the virtue of the CLD approach is that different geometries for nuclear clusters can be considered in a simple way, allowing for the study of the pasta phases [RPL83; LS91; LRP93; NGL12]. Let us first recall the virial theorem with curvature term, here expressed in term of the surface, curvature, and Coulomb energy densities,

$$\varepsilon_{surf} + 2\varepsilon_{curv} = 2\varepsilon_{Coul}. \tag{1.96}$$

Following [RPL83; NGL12], the general expression for the surface energy density is

$$\varepsilon_{surf} = \frac{ud\sigma}{r}, \tag{1.97}$$

and that of the curvature energy density is

$$\varepsilon_{curv} = \frac{ud(d-1)\sigma_c}{r^2}, \tag{1.98}$$

where the surface tension σ and curvature tension σ_c are independent of the dimensionality, and therefore given by Eqs. (1.59) and (1.61), respectively. The Coulomb energy density reads

$$\varepsilon_{Coul} = 2\pi(eY_p n_0 r)^2 u\eta_{Coul,d}(u), \tag{1.99}$$

with $\eta_{Coul,2} = \frac{1}{4}\left[\ln\left(\frac{1}{u}\right) + u - 1\right]$ for $d = 2$, and $\eta_{Coul,d}(u) = \frac{1}{d+2}\left[\frac{2}{d-2}\left(1 - \frac{du^{1-2/d}}{2}\right) + u\right]$ otherwise.

In the previous expressions, r represents the radius (half-width in the case of planar geometry) of clusters or holes, u the volume fraction occupied by the cluster (hole), n_0 the density of the dense phase, and Y_p its associated proton fraction. The expression of the volume fraction is different depending on whether we have clusters or holes:

$$u = \begin{cases} (n_B - n_g)/(n_0 - n_g) & \text{for clusters,} \\ (n_0 - n_B)/(n_0 - n_g) & \text{for holes.} \end{cases} \tag{1.100}$$

The parameter $d = \{3, 2, 1\}$ is related to the dimensionality, with $d = 3$ for spheres and bubbles, $d = 2$ for cylinders and tubes, and $d = 1$ for plates. In the former case, we naturally recover the expressions Eqs. (1.58), (1.60), and (1.56). Also, let us note that nuclei and bubble phases are identical as far as plates are concerned.
Replacing these quantities in Eq. (1.96), we obtain an equation for the cluster (hole) radius/half-width,

$$4\pi(eY_pn_0)^2\eta_{Coul,d}(u)r^4 - d\sigma r - 2d(d-1)\sigma_c = 0, \tag{1.101}$$

which has to be solved numerically. Let us notice that, neglecting the curvature term, the virial theorem reduces to $\varepsilon_{surf} = 2\varepsilon_{Coul}$, thus the expression of the r is analytical,

$$r = \left(\frac{d\sigma}{4\pi(eY_pn_0)^2\eta_{Coul,d}(u)}\right)^{1/3}. \tag{1.102}$$

In order to find the most stable phase at a given baryon density, we proceed as follows. The composition is first calculated at a given n_B in the spherical nuclei case ($d = 3$) following 1.2.2. Then, keeping the same composition, the radius/half-width r is evaluated for the five different phases by solving numerically Eq. (1.101). Finally, since the bulk and electron contributions to the WS cell are independent of the dimensionality, the equilibrium phase is the one that minimizes $\varepsilon_{surf} + \varepsilon_{curv} + \varepsilon_{Coul}$. Let us notice that this method has to be considered as an approximation since we do not consider the dimensionality dependence of the surface plus curvature energy in the minimization. This is similar to the so-called "coexisting phase method" employed in several works [Ava+08; Ava+10; Gra+17].

In the left panel of Fig. 1.11, we represent the WS energy density as a function of the baryon density for the five phases, using our CLDM to calculate the surface and curvature energy for the BSk24 functional. It is clearly seen that the spheres dominates up to $n_B \approx 0.05$ fm^{-3}, which is in good agreement with the semiclassical ETF results for this force [PCP20]. From this density, we find cylinders up to $n_B \approx 0.065$ fm^{-3}, before observing a transition to plates. Then, the differences in energy density become so small that the possible transition to another phase cannot be distinguished in the figure. However, one could expect the usual sequence, that is a transition to tubes eventually followed by one to bubbles before the final transition to homogeneous matter [RPL83], here marked by the black dashed lines.

The right panel of Fig. 1.11 shows the equilibrium phase as a function of n_B for four CLDM: BSk24, SLy4, BSk22, and DD-MEδ. While model dependence is observed, it is interesting to notice that the sequence spheres $\rightarrow$ cylinders $\rightarrow$ plates $\rightarrow$ tubes is
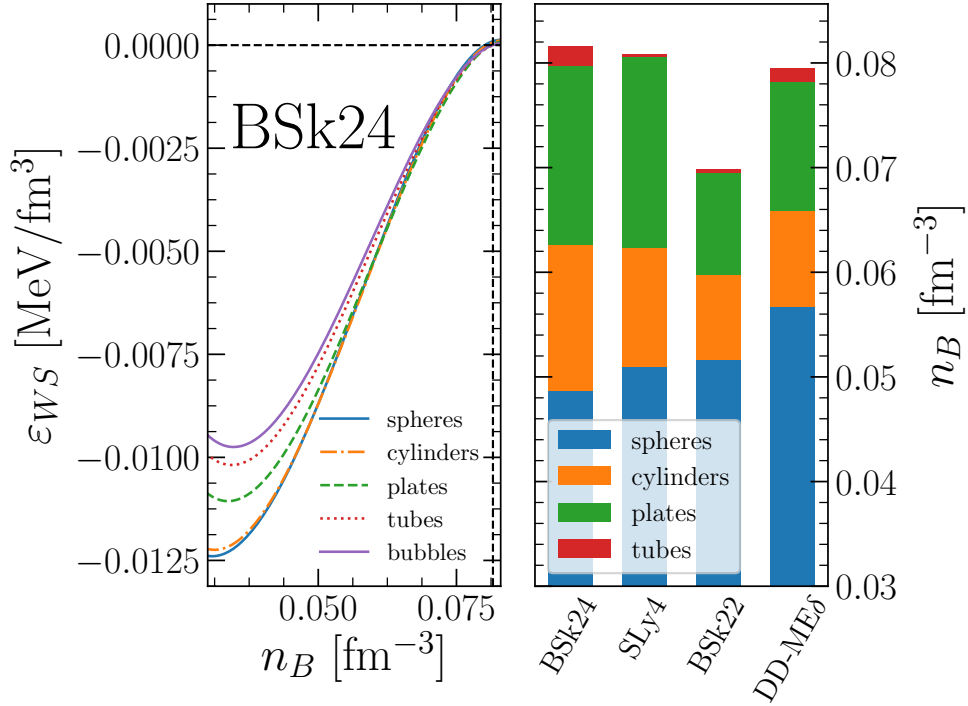
Figure 1.11: Left panel: energy density of matter as a function of baryon density for the five phases, using BSk24 CLDM. The black dashed lines mark the CC transition point. Right panel: equilibrium phase as a function of baryon density for four selected CLDM: BSk24, SLy4, BSk22, and DD-MEδ. For these calculations, the surface parameter p is fixed to the value $p = 3$.

recovered for every model. Another shared feature is that the transition to homogeneous matter is found before the appearance of bubbles. Let us remark that pasta phases are observed for SLy4 here, while previous CLD and TF calculations for this functional have predicted that the sphere is the most favorable shape at all densities up to the CC transition point [DH00; Viñ+17]. This contradiction can be understood by the fact that we are dealing with very tiny differences in energy density (all the shapes are very close), in a region where the matter is extremely neutron rich, thus where the nuclear surface tension is poorly constrained. In particular, we observed that varying the value of the surface parameter p can affect the sequence of pasta phases.

1.2.6   Crust-core transition from the crust side

It is well known that a phase transition from a solid crust to a liquid core takes place at some ≈ 1 km from the surface of the star, corresponding to subsaturation densities. A precise estimation of this transition point is necessary in order to evaluate the crust mass, thickness and moment of inertia, and so to understand phenomena involving NS,

such as glitches, that are irregularities in the their rotational motion [Esp+11]. In that sense, a Bayesian analysis of the CC transition has been performed [CGM19a] and is presented in details in Chapter 2.

The simplest approach for computing the phase transition is from the core side, in which the transition is defined as the density point where homogeneous nuclear matter (NM) at beta equilibrium becomes unstable with respect to density fluctuations. Two versions of this technique can be distinguished: the so-called thermodynamical [Gon+17] and dynamical [PRL95; Ant+19] methods.
The former method consists in evaluating the thermodynamical spinodal, that is the instability point of NM with respect to the liquid-gas (LG) phase transition. The only necessary nuclear physics input for this method is the energy functional of homogeneous NM, which can is well constrained through nuclear experiments and/or ab initio calculations in the vicinity of the nuclear saturation density n_{sat}. While it appears as a substantial advantage, it is known that the dynamics of the CC transition is very different from the LG one [DCG07; Duc+07; DMC08], thus applying this method results in an overestimation of the CC transition density and pressure. Indeed, the CC transition is expected to take place at approximately $\approx n_{sat}/2$, where the energy density of clusterized matter overcomes that of uniform NM [BBP71]. Since Coulomb, surface, and curvature terms, that are crucial for determining the equilibrium composition in the inner crust, vanish in homogeneous NM, they no not contribute to the determination of the LG thermodynamical spinodal.
In the dynamical method, finite-size density fluctuations are added, thus it is expected to give a better estimation of the CC transition and pressure. It should be stressed that the isovector gradient terms, which are needed in addition to the EoS with respect to the thermodynamical method, play a nonnegligible role for the determination of the dynamical spinodal, the location of which also depends on the many-body formalism adopted [DMC08].

While the dynamical method gives a better estimation of the CC transition point in comparison with the thermodynamical one, one should remark that the spinodal decomposition scenario is not compatible with the equilibrated crust in which matter is not uniform but composed of clusters immersed in a sea of electrons and neutrons. For this reason, the CC transition point is here computed from the crust side, by comparing the energy density of the two competing phases in beta equilibrium. The equation for the CC transition density n_t is thus

$$\varepsilon_{WS}^{crust}(n_t) = \varepsilon_{npe}(n_t), \tag{1.103}$$

where ε_{WS}^{crust} is the equilibrium energy density in the WS cell in the inner crust, and ε_{npe} is the equilibrium energy density of matter in the outer core, which consists of homogeneous *npe* matter, studied in Section 1.3. The CC transition point is computed in the following for several nuclear models, using the metamodeling technique extended to finite nuclei in the CLD approximation, Eq. (1.63), to calculate the WS cell energy density in the inner crust, and keeping the same empirical matter for the description of uniform *npe* matter. One should stress the importance of having a unified EoS for the crust and the core [DH01] to estimate correctly the CC transition point. Indeed, it was shown that matching a crust and core EoS based on different nuclear models induce
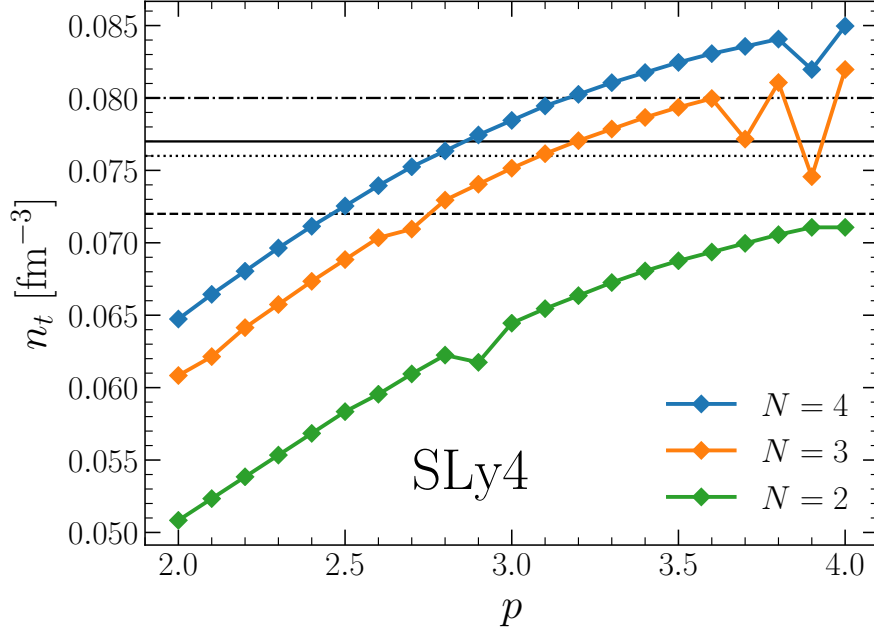
Figure 1.12: Crust-core transition density as a function of the surface parameter p with truncation order $N = 2$, $N = 3$, and $N = 4$, for SLy4 CLDM. The black horizontal bars represent different evaluations of n_t for the SLy4 functional found in the literature: $n_t = 0.072$ fm^{-3} [Viñ+17] (dashed line) and $n_t = 0.077$ fm^{-3} [DH00] (solid line) in the CLDM approximation, $n_t = 0.076$ fm^{-3} [Viñ+17] (dotted line) in the TF approximation, and $n_t = 0.080$ fm^{-3} [Viñ+17] (dashdotted line) with the dynamical method.

an uncertainty on the determination of the CC transition point, consequently inducing an uncertainty in the crustal observables, which can be as large as 30% for the crust thickness [For+16].

Let us mention that pasta phases are not considered here, since we have checked that their presence does not affect the estimation of the CC transition density and pressure.

In Fig. 1.12, we show the variation with surface parameter p of n_t for SLy4 CLDM. For each value of p, the surface and curvature parameters are fitted to experimental masses from the AME2016. The CC transition density is estimated for different values of the truncation order N in the density development, Eq. (1.50). A convergence feature is observed from $N = 2$ to $N = 4$, almost achieved at $N = 3$. We can see that truncating at $N = 2$ leads to a substantial underestimation of about $\approx 20\%$ of the transition density. This observation highlights the importance of keeping high-order parameters beyond (Q_{sat}, Q_{sym}) ($N = 3$), and (Z_{sat}, Z_{sym}) ($N = 4$) in the Taylor expansion.

A positive correlation is seen between the isovector surface parameter p and n_t: the higher the value of p the higher the transition density. This can be understood from the fact that a low value of p leads to a higher surface tension at extreme isospin values, thus it makes the cluster less bound and consequently the uniform npe matter becomes
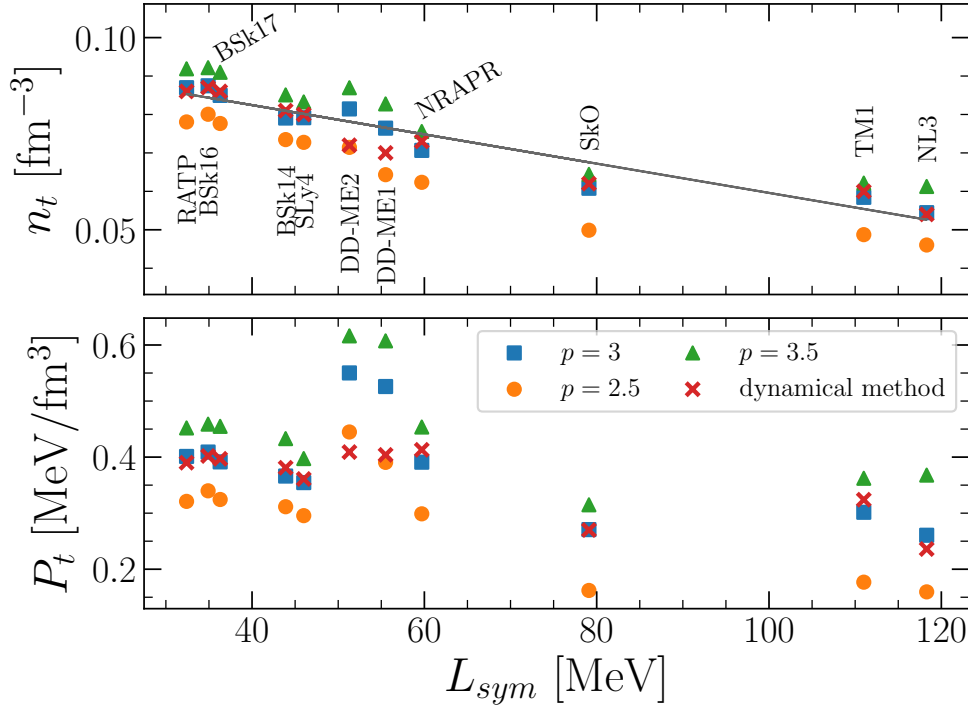
Figure 1.13: Crust-core transition density n_t (upper panel) and pressure P_t (lower panel) as a function of L_{sym} for several interactions. The crosses are the transition points calculated in [Duc+11] using the dynamical spinodal. The circles, squares, and triangles correspond respectively to our estimation of the transition points with $p = 2.5$, $p = 3$, and $p = 3.5$. The gray line is the linear regression curve fitted to the $p = 3$ results.

the favorable phase at lower density.

Different estimations of the CC transition density for the SLy4 functional found in the literature are reported in Fig. 1.12 (black lines), with n_t ranging from 0.072 fm^{-3} [Viñ+17], in the CLD approximation, to 0.089 fm^{-3} [Duc+11] (not represented in the figure), with the thermodynamical method. It is interesting to observe that the two different CLDM calculations of the literature based on SLy4 functional, reported in the figure, give a different estimation of n_t, with 0.072 fm^{-3} in [Viñ+17], and 0.077 fm^{-3} in [DH00]. This stresses once again the importance of the treatment of the isovector surface tension for the determination of the CC transition point.

The effect of the varying the low-density parameter b on n_t is also evaluated in [CGM19a]. It is found that while it does not significantly affect the transition density in comparison with N and p, it should be kept as an additional EoS parameter in any statistical analysis in order to make a quantitative prediction of the CC transition point. The introduction of the parameter b in the parameter space is, in fact, an effective manner to account for the effect of orders $N > 4$, which is not important.

Fig. 1.13 shows our estimations of the transition density n_t and pressure P_t as a func-

tion of the slope of the symmetry energy L_{sym} for a set of relativistic and nonrelativistic functionals, in comparison with the dynamical spinodal calculations of [Duc+11]. It is seen that the value $p = 3$ is in good agreement with the dynamical results for most of the models. For DD-ME2, the lower value needed for p is supported by the TF calculations in [GPA12].

As in [Viñ+17], an anticorrelation is observed between L_{sym} and n_t. Using a linear regression to model the relationship between L_{sym} and our estimation of n_t with $p = 3$, we find $n_t = -3.807 \times 10^{-4} L_{sym} + 0.098$ fm^{-3}, for a root mean square error of 3.094×10^{-3} fm^{-3}. This is linear equation for n_t is in very good agreement with Eq. (17) of [Duc+11]. This downwards tendency with increasing values of L_{sym} is not clearly observed for the transition pressure. We will see in Chapter 2 that the relation between those two quantities is less explicit because P_t rather depends on K_{sym}, which is logical because the pressure requires the calculation of one more derivative in comparison to the energy density that defines n_t.

1.3   Matter of the core

In the very bottom layers of the inner crust, clusters are so large and asymmetric that the CLD energy per nucleon, Eq. (1.63), becomes equal to that of infinite nuclear matter, marking the CC interface. While the composition and structure of the core close to the saturation density are well known, various scenarios have been proposed in the literature [Oer+17] concerning the relevant degrees of freedom above $2 - 3n_{sat}$.

This section deals with the matter of the core. In 1.3.1 we derive the system of variational equations for the ground state of the outer core. The model dependence of the composition and EoS is then explored. In particular, we focus on apparent correlations with the symmetry energy. The matter inside the inner core is finally discussed in 1.3.2.

1.3.1   Outer core: homogeneous *npeμ* matter

From the CC transition point, previously discussed in 1.2.6, up to $n_B \approx 2n_{sat}$, the matter of the core consists of a uniform plasma of neutrons, protons, electrons, and eventually muons, hereafter referred to as *npeμ* matter (or *npe* if muons are not present). This region of the star corresponds to the outer core. The energy density of *npeμ* matter reads

$$\varepsilon_{npe\mu}(n_B, \delta, n_e, n_\mu) = \varepsilon_{HM}(n_B, \delta) + \varepsilon_e(n_e) + \varepsilon_\mu(n_\mu) + n_B \frac{1-\delta}{2} \Delta m_{pn} c^2 + n_B m_n c^2, \ (1.104)$$

with $\varepsilon_{HM} = ne_{HM}$ the energy density of nuclear matter given by the metamodel, Eq. (1.37). The expression of energy density of the relativistic muon gas $\varepsilon_\mu(n_\mu)$ is the same as that of the relativistic electron gas, and it is derived in Appendix A.

1.3.1.1   Variational equations

Following 1.2.2, the system of differential equations determining the equilibrium composition and EoS in the outer core is determined by minimizing the energy density of

matter, Eq. (1.104), at constant baryon density under the condition of overall charge neutrality, which now reads

$$n_B \frac{1 - \delta}{2} = n_e + n_\mu. \tag{1.105}$$

since muons may exist in this region of the star. Muons are present in the outer core if the electron chemical potential exceeds the muon rest-mass energy, that is $\mu_e \gtrsim m_\mu c^2$. As far as variational variables are concerned, a reasonable choice appears to be the asymmetry δ and the muon density n_μ. Let us first minimize the energy density of matter with respect to δ,

$$\left. \frac{\partial \varepsilon_{npe\mu}}{\partial \delta} \right|_{n_\mu} = 0$$

$$2\frac{\partial e_{HM}}{\partial \delta} - \Delta m_{pn} c^2 - \mu_e = 0. \tag{1.106}$$

We can easily identify this equation with the well-known beta equilibrium condition. Indeed, using the definition of the neutron and proton chemical potentials, Eq. (1.53), we obtain

$$\mu_n = \mu_p + \mu_e. \tag{1.107}$$

We now turn to minimization with respect to the muon density,

$$\left. \frac{\partial \varepsilon_{npe\mu}}{\partial n_\mu} \right|_\delta = 0$$

$$\mu_\mu - \mu_e = 0, \tag{1.108}$$

where we have introduced the muon chemical potential $\mu_\mu = \partial \varepsilon_\mu / \partial n_\mu$. This equation corresponds to the chemical equilibrium between muons and electrons, and has to be satisfied if muons are present. These two equations, Eq. (1.107) and (1.108), express the equilibrium with respect to the weak interaction processes. Let us remark that each time we mention electrons and muons, we are always referring to their net number, that is particles minus antiparticles.

From the numerical point of view, we use Broyden's method to solve the beta equilibrium equation, Eq. (1.107), starting from the transition density n_t. The initial guess for the asymmetry δ_{guess} is taken to be the value of the global asymmetry inside the WS cell at the CC transition point, which is approximately ≈ 0.9. At each new step of baryon density, the value of δ_{guess} is updated with the last equilibrium solution, and we check if $\mu_e \gtrsim m_\mu c^2$. In the case of $npe\mu$ being energetically favorable, Eq. (1.108) is added as a supplementary equation to be solved, setting the initial guess for the muon density to $n_{\mu,guess} = 10^{-5}$ fm^{-3}. The calculation is stopped when the baryon density reach $\approx 2n_{sat}$, from which the composition of matter becomes less certain.

1.3.1.2   Equilibrium composition and equation of state

In Fig. 1.14, the proton fraction $Y_p = (1-\delta)/2$ and muon fraction $Y_\mu = n_\mu/n_B$ are plotted as a function of the baryon density for the four nuclear models BSk24, SLy4, BSk22, and DD-MEδ, the empirical parameters of which are listed in Table 1.3. The variation
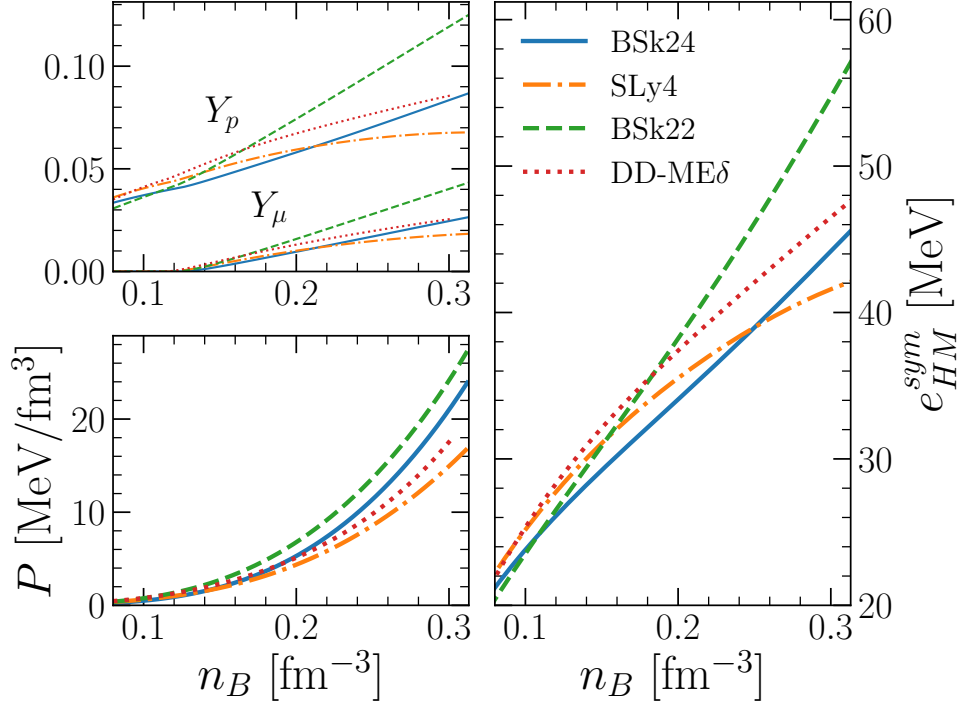
Figure 1.14: Left: Proton fraction Y_p and muon fraction Y_μ (upper panel), and pressure P (lower panel) as a function of the baryon density n_B in the outer core for four selected models: BSk24, SLy4, BSk22, and DD-MEδ. Right: Variation with baryon density of the symmetry energy e_{HM}^{sym}, Eq. (1.52), for the four models.

n_B of the electron fraction Y_e can be deduced from the charge neutrality condition, Eq. (1.105). Surprisingly, it is observed that the proton fraction rises with n_B in the outer core, while it monotonously decreases in the crust. A strong correlation between the proton fraction and the symmetry energy, represented in the right panel for the four models, is seen. One can relate the two quantities using the beta equilibrium condition. Indeed, we can easily go through Eq. (1.107) assuming a quadratic expansion for the NM energy per nucleon,

$$e_{HM}(n_B, \delta) \simeq e_{HM}(n_B, \delta = 0) + \delta^2 e_{HM}^{sym}(n_B). \tag{1.109}$$

In that case, the beta equilibrium condition reads

$$4\delta e_{HM}^{sym}(n_B) - \Delta m_{pn} c^2 = \mu_e(n_e), \tag{1.110}$$

and we can thus express the proton equilibrium proton fraction as a function of the symmetry energy,

$$Y_p = \frac{1}{2} - \frac{\mu_e(n_e) + \Delta m_{pn} c^2}{8 e_{HM}^{sym}(n_B)}. \tag{1.111}$$

From this equation it is clear that the higher the symmetry energy, the higher the proton fraction, which is the trend observed in the figure.

The density from which muons are present is also shown in the upper left panel. It appears that we are dealing with *npe* matter up to $n_B \approx 0.12$ fm^{-3}, and it is seen that the threshold density for the appearance of muons, when $\mu_e \gtrsim m_\mu c^2$, is not very sensitive to the nuclear model.

Fig. 1.14 also shows the pressure as a function of the density (lower left panel). In the outer core, we can write the pressure as

$$P(n_B) = P_{HM}(n_B, \delta) + P_e(n_e) + P_\mu(n_\mu), \qquad (1.112)$$

where δ, n_e, and n_μ are the equilibrium values at n_B. The expression of the nuclear contribution P_{HM} is given by Eq. (1.54). The electron and muon contributions to the total pressure, respectively P_e and P_μ, share the same expression, Eq. (1.11), which is that of a relativistic Fermi gas. A strong model dependence is observed for the pressure at suprasaturation densities, reflecting the large uncertainties associated to the isovector parameters beyond E_{sym}, as reported in the last column of Table 1.3.

1.3.2 Inner core

From the crust-core interface up to $n_B \approx 2n_{sat}$, it is commonly accepted that matter is exclusively composed of neutrons, protons, electrons, and muons. At higher densities however, the composition of matter becomes uncertain and different scenarios have been considered in the literature for the structure and composition of the inner core [Oer+17]. The presence of hyperons at suprasaturation densities has been considered in many studies, and its effect on the EoS and subsequently on NS observables has been evaluated [Bed+12; For+15]. In particular, the presence of hyperons softens the high-density EoS and thus lowers the maximum mass of neutron stars. As a consequence, many models fail to satisfy the NS mass constraint of $\approx 2M_\odot$ [Dem+10; Ant+13], leading to the so-called "hyperon puzzle" [ZH13]. In fact, the measurement of $\approx 2M_\odot$ NS also rules out most of the models that include a phase transition to quark matter or a boson condensate in the inner core, because the EoS is softened by the introduction of any additional degree of freedom without an interaction. Let us however mention a recently proposed EoS with a quark-hadron crossover at high density that allows a maximum mass of $2.35M_\odot$ [Bay+19] and agrees with the constraints on NS properties inferred from the GW170817 event [Abb+18; Abb+19].

We propose here to extrapolate the *npeμ* matter at higher densities, in the inner core. The different studies that consider hyperons and satisfy the maximum mass constraint show that the hyperon-nucleon and hyperon-hyperon are such that, if hyperons exist, they are not abundant and can be neglected as a first approximation, at least in the EoS energetics (see [Oer+17] and references therein). Since the metamodeling does not make any assumption regarding the degrees of freedom, but that the functional is based on a Taylor expansion, we can assume that the technique can be safely extended at high density in the aim of calculating static properties, such as the EoS or the mass-radius relation. The only thing that could invalidate it would be the presence of a large first-order phase transition, that is a large discontinuity in the EoS. Thus,

the only hypothesis that is made here is considering that there is no such transition. Actually, even a transition to quark matter could be smooth. Indeed, several works consider pasta phases in the hadron-quark phase transition, with the effect of washing out discontinuities [MTC09; YMT09; YMT11; Yas+14]. Finally, this is equivalent to a null hypothesis: since the metamodeling allows to control uncertainties, a disagreement with astrophysical observations would be the sign of new physics, indicating either the existence of a first-order phase transition or an alternative theory of gravity. Let us recall that the metamodeling technique gives an accurate reproduction of existing nuclear models up to $\approx 2 - 3n_{sat}$ (metamodeling ELFc in [MHG18a]), as we have verified in Fig. 1.4. A solution for achieving faster convergence at high density, the metamodeling ELFd, is proposed in [MHG18a]. It is based on a reevaluation of the high-order empirical parameters parameters Q_{sat}, Q_{sym}, and Z_{sat}, Z_{sym}, by imposing a high-density point at which the energy per nucleon and the pressure are known for a given functional. This is encouraged by the fact that the impact of these parameters is very small in the vicinity of the saturation density. We will use this technique when we will want to reproduce existing hadronic models.

1.4 Unified metamodeling of the equation of state

As previously discussed, matching a crust and core based on different nuclear models can lead to large uncertainties associated with the CC transition density and pressure, which are the quantities for the determination of the crust observables. In particular, it was shown in [For+16] that it can lead to an error as large as $\approx 30\%$ for the crust thickness and $\approx 4\%$ for the radius. The main justification for working with nonunified EoS is that the core is responsible of most of the NS mass, thus one could simply match any crust EoS, for instance that of BPS in the outer crust [BPS71] plus that of BBP in the inner crust [BBP71], with its core EoS based on a different nuclear interaction. This is indeed sufficient if one is interested in observables such as the maximum mass. However, it obviously leaves a large freedom in the matching procedure. In addition, this amounts to consider that the crust segment is not model dependent, while we have clearly seen in 1.2.3.3 that the crust EoS is sensitive to the nuclear model, and is in particular correlated with the symmetry energy. It is therefore preferable to describe the crust and core in a unified manner.

Several unified EoS for cold non-accreting NS have been proposed in the literature. For instance, the well-known DH EoS [DH01] is based on the Skyrme SLy4 effective interaction [Cha+98]. In the inner crust, the authors use a version of the CLDM to calculate the energy of finite nuclei, the bulk term of which is given by the SLy4 functional in the infinite NM limit, which is also used to describe the outside neutron gas, and at high density to calculate the $npe\mu$ matter energetics in the core. Let us notice that the EoS of the outer-crust ground state is taken from [HP94] in this work.

More recently, a series of unified EoS based on modern BSk functionals [GCP13] has been proposed [Pea+18]. In this work, the ground state of the outer crust is determined by application of the microscopic HFB method [Sam+02], and the ground state of the inner crust is calculated within the ETFSI approximation [Ons+08]. Also, a set of unified EoS were built within a relativistic mean-field approach (RMF) in [For+16].
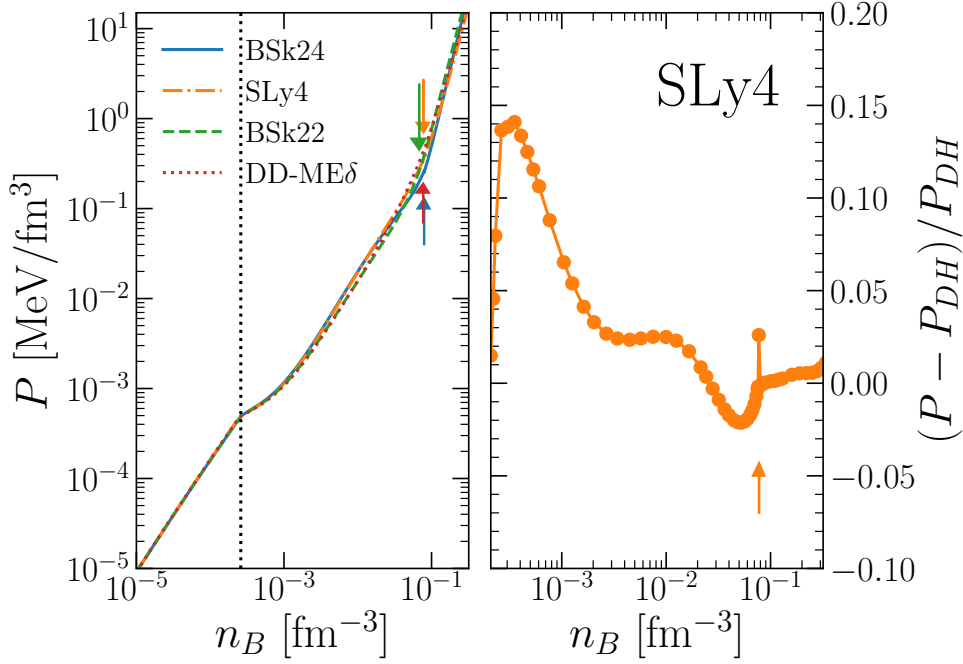
Figure 1.15: Left: Pressure as a function of baryon density in the different regions of a NS for BSk24, SLy4, BSk22, and DD-MEδ. Crust and core are described in a unified manner, with the metamodeling technique. The black dotted line marks the onset of the inner crust, and arrows indicate the CC transition density for the different models. Right: Relative difference $(P - P_{DH})/P_{DH}$ with DH unified EoS for SLy4 [DH01] as a function of n_B. The arrow indicates our estimation of the CC transition density for SLy4.

One obvious reason explaining why crust and core matter are not consistently treated using the same microscopic interaction is that it is less trivial to evaluate the ground state of the inner crust in comparison to the ground state of matter in the core. Indeed, one can evaluate the inner-crust ground state within different many-body approaches, either using the CLDM, the semiclassical ETFSI method, or full HF calculations. While the two last methods are expected to be more precise with respect to the CLD approximation as far as the composition is concerned, they can become computationally heavy if one wants to compute the EoS for many nuclear models. In addition, these more microscopic methods can only be extended to finite temperature in the SNA, whereas the CLD approximation allows distributions of clusters, that exist at $T > 0$, to be considered. In view to provide a unified and thermodynamically consistent treatment of the crust and core of cold non-accreting NS, we propose to compute the EoS within the metamodeling approach that we have presented throughout this chapter. For a given nuclear model, in other words a given set of empirical parameters $\boldsymbol{P_\alpha}$, we proceed as follows. The EoS in the outer crust is evaluated by application of the BPS method presented in 1.1.2, using

the present day knowledge on experimental masses [Hua+17] supplemented by state-of-the-art microscopic HFB theoretical mass tables [GCP13] up to the neutron-drip point. The EoS in the inner crust is then calculated by solving the system of four differential equations, Eqs. (1.85), (1.86), (1.87), and (1.88). The metamodeling technique, discussed in 1.2.1.1, is used to calculate the neutron gas energy. The concept of metamodeling of homogeneous NM is extended to finite nuclei in the CLD approximation in order to evaluate the cluster energy, the bulk term of which is calculated with the same empirical parameters as the neutron gas. Finally, from the CC transition point, discussed in 1.2.6, the core EoS is computed by solving the two chemical equilibrium equations Eqs. (1.107) and (1.108). Again, the empirical parameters are the same as those used in the inner crust. Within such an approach, one can compute the unified EoS for any nuclear model. In addition, this method is not expensive from the computational point of view, which will allow us to make comprehensive statistical evaluations of the model uncertainties in Chapter 2.

The left panel of Fig. 1.15 shows the resulting unified EoS for the four nuclear models considered in this chapter: BSk24, SLy4, BSk22, and DD-MEδ. The neutron-drip point is represented by the vertical dotted line, and arrows indicate the CC transition density for each model.

The relative difference between the DH EoS [DH01] and our EoS for SLy4 is represented as a function of the baryon density in the right panel of Fig. 1.15. It is seen that the overall difference is smaller than 10% in the inner crust. The slight disagreement at low density comes from the fact that the onset of the inner crust is marked at $n_{ND} = 2.0905 \times 10^{-4}$ fm^{-3} in the DH EoS (calculated in [HP94]), which is low in comparison with our estimation of the neutron drip density, $n_{ND} = 2.503 \times 10^{-4}$ fm^{-3}. Let us notice that the parametrization of the surface tension in both studies is different, therefore it might explain the difference between the two EoS at higher densities in the inner crust, in addition to the slight error introduced by the metamodel. In the core, we can observe that the relative difference is smaller that 1%.

1.5   Conclusion

In this chapter, we have first evaluated the ground state of the outer crust, which is obtained by the application of the BPS method, using recent experimental masses [Hua+17; Wel+17] supplemented by state-of-the-art microscopic HFB theoretical mass tables. We have shown that the outer-crust composition and so the EoS are entirely determined by the present day knowledge on experimental masses up to $n_B \approx 3 \times 10^{-5}$ fm^{-3}. At higher densities, we have observed the persistence of $N = 82$ for each of the four mass models considered.

We have proposed a version of the CLDM based on the metamodeling technique [MHG18a; MHG18b]. We have seen that the metamodel offers the possibility to reproduce any functional of nuclear matter very precisely, with a unique functional form. The parametrization of surface tension was suggested from microscopic calculations in the free neutron regime [RPL83], and surface and curvature parameters are fitted to experimental masses. We have used the CLDM to calculate the ground state of the inner crust, which is obtained by minimizing the energy density of matter at constant baryon

density under the condition of overall charge neutrality. We have therefore derived a system of four coupled differential equations, corresponding to chemical and mechanical equilibrium conditions, that we have solved numerically using Broyden's method. The ground-state composition of the inner crust for BSk24 empirical parameters was presented, and a very good agreement with more microscopic approaches was observed concerning the value of $Z \approx 40$. We have also seen that the proton fraction is continuously decreasing, as in the outer crust. The inner crust EoS was computed and a positive correlation with the empirical parameter E_{sym} was revealed. We have shown that magic numbers, that vanish within the CLD approach, can be recovered by adding perturbatively Strutinsky shell corrections on top of the CLD energy. In this way, a very good agreement with ETFSI calculations was observed for recent BSk functionals [Pea+18]. With the CLDM, we have explored the possible presence of nonspherical pasta phases in the bottom layers of the inner crust, finding the sequence spheres → cylinders → plates → tubes for each of the four model considered: BSk24, SLy4, BSk22, and DD-MEδ. We have shown that the transition point to homogeneous matter is very sensitive to the surface tension at extreme values of isospin, the behavior of which is governed by the isovector surface parameter p. Unfortunately, this parameter cannot be accessed from empirical nuclear physics data, which are limited to values around $I \lesssim 0.3$. We have seen that the CC transition density and pressure results of the literature for the dynamical spinodal [Duc+11] are globally nicely reproduced by our calculation from the crust with $p \approx 3$. We have also confirmed the correlation of the transition density n_t with the empirical parameter L_{sym} already observed in previous works.

We have derived the equilibrium equations characterizing the ground state of matter in the core, which consists of $npe\mu$ matter up to $n_B \approx 2n_{sat}$. The strong correlation between the symmetry energy and the proton fraction was explained. We have found that muons appear in the vicinity of $n_B \approx 0.12$ fm^{-3} for each model. As in previous works [WFF88; DH01], we have extrapolated the npeμ model to higher densities, since the hyperon-hyperon and hyperon-nucleon interactions remain currently poorly constrained.

Finally, we have stressed that building unified EoS is essential to properly estimate crustal observables. In that sense we have proposed a metamodeling of the EoS of cold non-accreting NS, where the crust and core are treated in a uniform manner, that is with the same empirical parameters. Using the SLy4 empirical parameters, we have shown that the relative difference with the DH EoS is smaller than 10% in the inner crust and 1% in the core.

In Chapter 2, we will exploit the second advantage of the metamodeling technique, namely the fact that no artificial correlations are introduced a priori among the empirical parameters, to carry out complete statistical analyses that will allow us to settle the model dependence of the results.

Chapter 2

Bayesian inference of neutron star observables

This chapter deals with the determination of NS observables within the Bayesian framework.

Pulsars were identified to rotating NS which produce pulsed emission, soon after their chance discovery in 1967 by Jocelyn Bell [Hew+68]. Five decades later, we have now observed about 2000 of them, and numerous techniques have been developed to measure their characteristic observables. For instance, precise measurements of NS masses can be performed using the relativistic Shapiro delay effect [Dem+10; Ant+13; Cro+20], the ambitious NICER program is expected to give a strong constraint on the NS radii in the near future [GAO12], and the first detection of gravitational waves (GW) from the coalescence of two NS, the GW170817 event, has provided a constraint on the tidal deformability of NS [Abb+17; Abb+18; Abb+19]. All those experimental data can be used to better constrain the nuclear EoS. Reciprocally, there has been a lot of efforts invested recently in the development of the chiral effective field theory (EFT) [DHS16] with the aim of providing new constraints on the low-density EoS, which can ultimately be translated into theoretical constraints on NS observables [CGM19a; CGM19b]. The Bayesian framework is particularly appealing for making realistic predictions for NS observables. It allows to update our prior beliefs on the EoS parameters with the constraints arising from the multiple sources mentioned above.

The plan of the chapter is as follows. In Section 2.1, global properties and crustal observables are calculated for several characteristic EoS by solving the equations of hydrostatic equilibrium in general relativity. The connection between the crust moment of inertia and the glitch phenomenon is explained. The EoS parameters parameters are determined within the Bayesian framework in 2.2, given the present day constraints on nuclear physics, NS observables, and physical requirements. In particular, correlations among the empirical parameters are explored. General predictions for NS observables are proposed in 2.3, using the joint posterior distribution of EoS parameters. We confront our predictions with different constraints inferred from the GW170817 event. The CC transition density and pressure as well as the fraction crust moment of inertia are evaluated. The full crustal origin of Vela pulsar glitches is discussed. Finally, conclusions

are given in Section 2.4.

Contents

2.1 From the equation of state to neutron star observables

The stellar EoS, the determination of which was studied thoroughly in Chapter 1, is the fundamental ingredient to build NS models. It enters into the basic equation for calculating macroscopic observables relevant to NS, that is so-called Tolman-Oppenheimer-Volkoff (TOV) equation, which describes the hydrostatic equilibrium for a spherically symmetric star in the framework of general relativity [Tol39; OV39].

This section deals with the estimation of NS observables for several popular EoS calculated within the metamodeling technique introduced in Chapter 1. In 2.3.1, we first solve the hydrostatic equilibrium equations so as to determine the mass-radius relation. The thickness and mass of the crust are also evaluated. The calculation of the NS moment of inertia in the slow rotation approximation is performed in 2.1.2. In particular, we show how the fraction of crust moment of inertia is connected to the observation of pulsar glitches. In 2.1.3, we finally compute the tidal deformability, which describes how much the NS is deformed by tidal forces, arising, for instance, when two NS orbit each other.

2.1.1 Masses and radii

From the observational point of view, it is easier for astronomers to measure the mass of a NS entering into a binary system. There are several types of binaries: x-ray binaries, double NS binaries, radio pulsar–white dwarf binaries, and radio pulsar–nondegenerate star binaries. Depending on the type of binary, different techniques are used to infer the NS mass [HPY07]. For example, in a pulsar binary system, various phenomena, such as the relativistic Shapiro delay [Sha64], can be measured via pulsar timing, which consists of the regular monitoring of the rotation of a pulsar over long periods (years to decades). The relativistic Shapiro delay is a phenomenon from which precise masses for both a millisecond pulsar and its companion can be inferred [Dem+10; Cro+20]. Let us notice however that it is only observed in a small subset of high-precision, highly inclined binary pulsar systems.
Measuring NS radii with high precision is a more challenging task, and it constitutes one of the goals of the ambitious NICER mission [GAO12]. This observable can be extracted from the analysis of thermal emission from neutron star surfaces, or x-ray emission from accreting neutron stars in binaries.

In the following, we turn to the theoretical prediction of NS masses and radii. The hydrostatic equilibrium equations in general relativity are first solved in order to represent the mass-radius relation for several popular EoS, which are then confronted to NS mass measurements. The estimation of the crustal thickness and mass is discussed afterwards.

2.1.1.1 Mass-radius relation

Theoretically, the NS masses and radii correspond to the solution of the hydrostatic equilibrium equations, which are, in general relativity for spherical and nonrotating

stars [Tol39; OV39],

$$\frac{dP}{dr} = -\frac{G\rho_B m}{r^2}\left(1 + \frac{P}{\rho_B c^2}\right)\left(1 + \frac{4\pi P r^3}{mc^2}\right)\left(1 - \frac{2Gm}{rc^2}\right)^{-1}, \qquad (2.1)$$

$$\frac{dm}{dr} = 4\pi r^2 \rho_B, \qquad (2.2)$$

$$\frac{d\Phi}{dr} = -\frac{1}{\rho_B c^2}\frac{dP}{dr}\left(1 + \frac{P}{\rho_B c^2}\right)^{-1}, \qquad (2.3)$$

where G is the gravitational constant, P the pressure, $\rho_B c^2$ the energy density, and $m(r)$ the is the gravitational mass inside the sphere of radius r, defined within the Schwarzschild metric $ds^2 = c^2 dt^2 e^{2\Phi} - e^{2\lambda}dr^2 - r^2(d\theta^2 + \sin^2\theta d\phi^2)$. The function $\Phi(r)$ corresponds to the gravitational potential, and $\lambda(r)$ is related to the enclosed mass $m(r)$ through

$$e^{-\lambda} = \sqrt{1 - \frac{2Gm}{rc^2}}. \qquad (2.4)$$

Eq. (2.1) is the TOV equation of hydrostatic equilibrium. The integration of Eq. (2.2) from $r = 0$ to the boundary $r = R$, R being the NS radius, gives the total gravitational mass $M = m(R)$ of the star. Eq. (2.3) is a relativistic equation for the metric function $\Phi(r)$. Here, we focus on solving Eqs. (2.1) and (2.2), which gives the profiles $P(r)$, $\rho_B(r)$, and $m(r)$ for a given EoS, $P(\rho_B)$, the determination of which was discussed in detail in Chapter 1.

In view of solving the hydrostatic equilibrium equations for a given tabulated EoS, one first have to choose an arbitrary value for the central density $\rho_{B,c}$ and interpolate the central pressure $P_c = P(\rho_{B,c})$, corresponding to $r = 0$, with the associated boundary condition $m(r = 0) = 0$. Then, using a Runge-Kutta method, one integrate up to $r = R$, defined as $P(r = R) = 0$ (our numerical condition is $P < 5 \times 10^{-4}$ MeV/fm^3, which is a sufficiently low value of the pressure). At each new step of pressure, one has to interpolate the mass density ρ_B in the table. In the end, for a given value of central density $\rho_{B,c}$, one obtains the profiles $P(r)$, $\rho_B(r)$, and $m(r)$, and therefore a value for the NS mass M and radius R. The typical values of these observables are $M = 1.4 M_\odot$ and $R = 10$ km [HPY07].

In fact, the central density inside a specific NS is not known, and is expected to range from $\approx 4.6 \times 10^{14}$ g/cm^3 to $\approx 4 \times 10^{15}$ g/cm^3. For this reason, we are rather interested in the mass-radius relation, which can be obtained by calculating M and R, following the numerical method previously explained, for this range of central mass densities.

Let us recall that one has to redefine the high-order parameters $Q_{sat(sym)}$ and $Z_{sat(sym)}$ in order to reproduce existing functionals at densities greater than $2n_{sat}$ with the meta-modeling technique. This corresponds to the ELFd technique introduced in [MHG18a].

The left panel of Fig. 2.1 shows the mass-radius relation for several popular EoS based on Skyrme-type functionals BSk24, SLy4, and BSk14, and relativistic models PKDD and TM1, calculated within the metamodeling technique. A strong model dependence is observed, with radii of canonical NS ranging from $R_{1.4} = 11.5$ km for BSk14 to $R_{1.4} = 14.5$ km for TM1. More specifically, it is seen that the radius is positively correlated to the slope of the symmetry energy L_{sym}. The value of the empirical parameters associated

Parameter	Unit	N	BSk14	PKDD	TM1
E_{sat}	MeV	0	-15.85	-16.27	-16.26
n_{sat}	fm^{-3}	1	0.1586	0.1495	0.1450
K_{sat}	MeV	2	239	261	281
Q_{sat}	MeV	3	-359	-119	-285
Z_{sat}	MeV	4	1435	4213	2014
E_{sym}	MeV	0	30.00	31.19	36.94
L_{sym}	MeV	1	43.9	79.5	111.0
K_{sym}	MeV	2	-152	-50	34
Q_{sym}	MeV	3	389	-28	-67
Z_{sym}	MeV	4	-2191	-1315	-1546
m^*_{sat}/m			0.80	0.65	0.71
$\Delta m^*_{sat}/m$			0.03	-0.08	-0.09

Table 2.1: Value of each of the empirical parameters, associated unit, and derivative order N for BSk14 [GSP07], PKDD [Lon+04], and TM1 [SKT95] functionals.

to BSk14, TM1, and PKDD are reported in Table 2.1, whereas those of BSk24 and SLy4 can be found in Table 1.3.

The bands correspond to the measured masses of the two most massive pulsars observed to the present day. The mass of PSR J0348+0432 was precisely estimated to $(2.01 \pm 0.04)M_\odot$ [Ant+13], and the very recent relativistic Shapiro delay measurements of PSR J0740+6620 led to $2.14^{0.10}_{-0.09}M_\odot$ (68.3% credibility interval) [Cro+20]. Naturally, if an EoS cannot insure such high masses, it should not be considered as reliable, in particular at high density, since the maximum mass is determined by the stellar core EoS. In particular, it is seen that the maximum mass corresponding to the BSk14 functional, $1.8M_\odot$, is lower than the measured mass of PSR J0348+0432. Also, while the SLy4 EoS satisfy this constraint, the maximum mass for this EoS, $2.05M_\odot$, is lower than that of PSR J0740+6620. This outline the fact that measuring the mass of pulsars is important, because it provides a strong constraint on the stellar matter EoS. Similarly, the NICER telescope is expected to provide, for years to come, a constraint on the NS radii with a precision of 5%. Ultimately, in the ideal case where one could accurately measure the mass and radius of one neutron star, it would be possible to determine the EoS by positioning the point in the $M - R$ diagram.

The mass-radius relation for the SLy4 EoS is represented in the right panel of Fig. 2.1. The solid orange line corresponds to $M(R)$ for the SLy4 EoS calculated within the meta-modeling technique, and the dashed black line is the calculation based on the DH EoS for SLy4 functional. A perfect agreement is observed between the two curves, reflecting the small error on the EoS, illustrated in Fig. 1.15.

The dotted orange line shows the mass-radius relation for the SLy4 EoS without considering the clustering of matter at low density, that is assuming that the NS star interior consists of $npe\mu$ matter at all densities. In that case, for a canonical NS, we find $R_{1.4} = 11.1$ km, which is almost 1 km lower with respect to the result with a crust EoS.
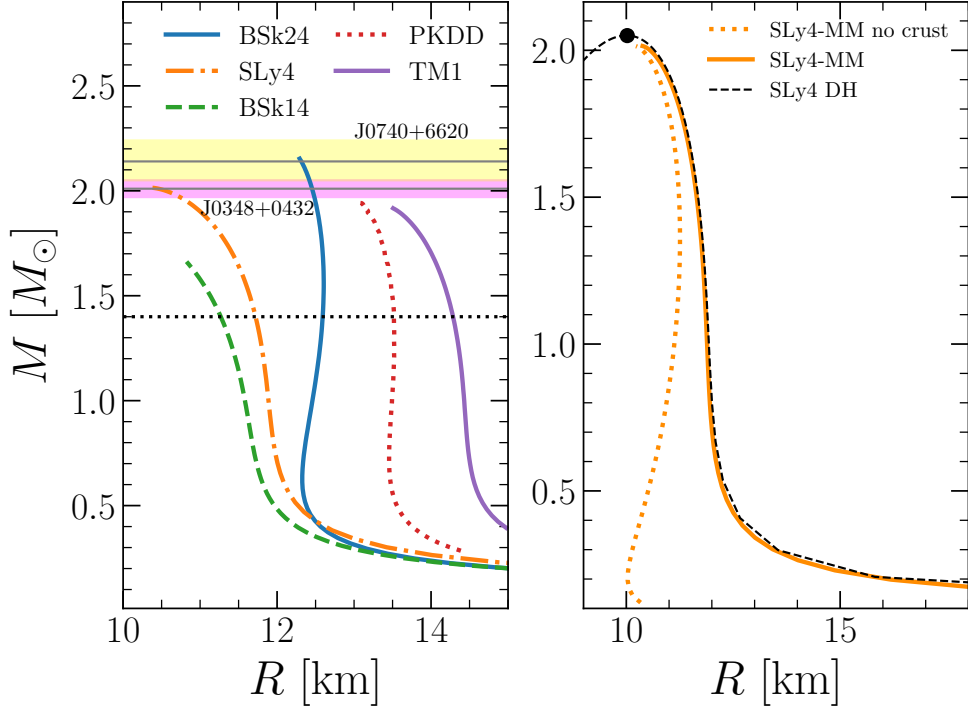
Figure 2.1: Left: Mass-radius relation for several popular EoS calculated with the meta-modeling technique. The black dotted line marks the NS canonical mass, that is $1.4 M_\odot$. The magenta band represents the measured mass of PSR J0348+0432, $(2.01 \pm 0.04) M_\odot$ [Ant+13], and the yellow band that of PSR J0740+6620, $2.14^{+0.10}_{-0.09} M_\odot$ (68.3% credibility interval) [Cro+20]. Right: Mass-radius relation for the DH EoS for SLy4 functional (black dashed line), and the SLy4 EoS calculated with the metamodeling technique (solid orange line). The black circle indicates the maximum mass.

Moreover, this difference is found to be larger with decreasing mass. This shows that the crust EoS is essential to properly predict NS radii. However, we can see that the NS maximum mass is entirely determined by the stellar core EoS.

The black point marks the maximum mass for the SLy4 EoS, $M_{max} = 2.05 M_\odot$. Let us notice that the branch left to the point is unstable, because from this point the mass decreases with central density increasing.

2.1.1.2   Crust thickness and mass

As explained in Chapter 1, a precise estimation of the CC transition point is required as far as crustal properties are concerned. In particular, the transition pressure P_t is essential for the determination of the thickness and mass of the crust, given respectively by $l_{crust} = R - R_{core}$ and $M_{crust} = M - M_{core}$, with R_{core} (M_{core}) the radius (mass) of the stellar core. Indeed, in order to calculate the core radius and mass, which are involved in
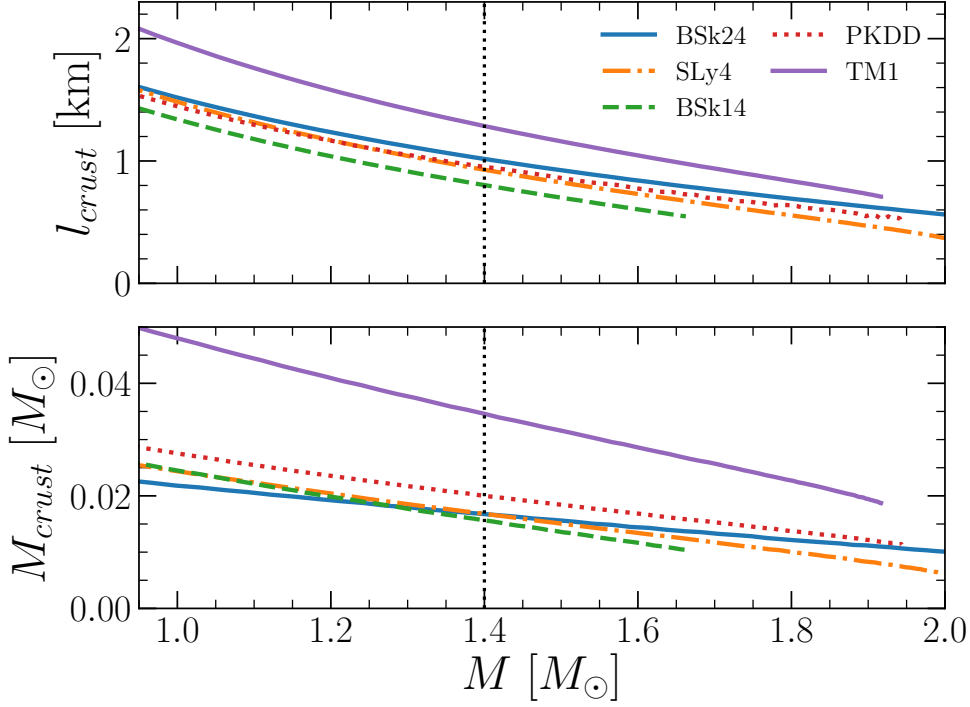
Figure 2.2: Crust thickness l_{crust} (upper panel) and mass M_{crust} (lower panel) as a function of the NS mass M for several popular EoS calculated within the metamodeling technique. The black dotted line marks the NS canonical mass, that is $1.4 M_\odot$.

the calculation of the crustal observables, one has to integrate the hydrostatic equilibrium equations, Eqs. (2.1) and (2.2), from $r = 0$ to $r = R_{core}$, defined as $P(r = R_{core}) = P_t$.

Fig. 2.2 shows the variation with NS mass of crust thickness l_{crust} and mass M_{crust} for the same EoS as in Fig. 2.1. As previously, the high-order empirical parameters are reevaluated to calculate the EoS entering the TOV equation. However, the transition pressure is calculated using the values of $Q_{sat(sym)}$ and $Z_{sat(sym)}$ directly derived from the selected functionals. The reason is that, as showed in Fig. 1.12, the determination of CC transition point is sensitive to orders $N > 2$.

We find the interesting result that the crust is thicker for low-mass neutron stars, and in consequence that the M_{crust} drops continuously with increasing NS mass. At $M = 1.4 M_\odot$ (black dotted line), we observe that the crust is ≈ 1 km thick, and that the crust mass is approximately $0.02 - 0.04 M_\odot$, which is $(1.5 - 3)\%$ of the total mass. Once again, a model dependence is observed. Nonetheless, the correlation of the crust thickness with the slope of the symmetry energy is not clear. In Fig. 2.1, we have seen that the radius of the star is positively correlated with L_{sym}. In fact, the same is true for the core radius, explaining why the correlations cancel in the crust thickness $l_{crust} = R - R_{core}$.

2.1.2   Moment of inertia within the slow rotation approximation

We now turn to the calculation of the moment of inertia within the slow rotation approximation [Har67]. In fact, this approximation is not only applicable to slowly rotating pulsars but is also reliable for most of them. Indeed, while many observed pulsars show rapid rotation [SLL13], their structure is almost not altered by it since centrifugal forces are small in comparison to the gravity, $R^3\Omega^2/(GM) \ll 1$, Ω being the angular frequency. For instance, let us consider a rapidly rotating pulsar with $\Omega = 1000$ s^{-1} and canonical values for its mass and radius, $M = 1.4M_\odot$ and $R = 10$ km. In that case, we find $R^3\Omega^2/(GM) \approx 0.025$.

In the following, we first calculate the total moment of inertia and the fraction of it contained in the NS crust for several popular EoS. Then, we explain the connection between the fraction of crust moment of inertia and the glitch behavior exhibited by some pulsars [Esp+11].

2.1.2.1   Total moment of inertia and fraction contained in the crust

In a slowly rotating NS, the total moment of inertia is given by [Har67]

$$I = \frac{8\pi}{3}\int_0^R dr\, r^4 \left(\rho_B + \frac{P}{c^2}\right)\frac{\bar{\omega}}{\Omega}e^{-\lambda-\Phi}, \tag{2.5}$$

where we have introduced the rotational drag function $\bar{\omega}(r)$, which satisfies

$$\frac{d}{dr}\left(r^4 j \frac{d\bar{\omega}}{dr}\right) = -4r^3\bar{\omega}\frac{dj}{dr}, \tag{2.6}$$

with $j = e^{-\Phi-\lambda}$. Eq. (2.6) satisfy the following boundary conditions at the surface and center of the NS, respectively:

$$\frac{1}{\Omega}\bar{\omega}(r = R) = 1 - \frac{2GI}{R^3c^2} \quad \text{and} \quad \left.\frac{d\bar{\omega}}{dr}\right|_{r=0} = 0. \tag{2.7}$$

One can translate Eq. (2.6) into a first-order differential equation by introducing $w = (1/\Omega)d\ln\bar{\omega}/d\ln r$, yielding

$$\frac{dw}{dr} = \frac{4\pi G}{c^2}\frac{(P + \rho_B c^2)(4 + w)r^2}{rc^2 - 2Gm} - \frac{w}{r}(3 + w), \tag{2.8}$$

with the boundary condition $w(r = 0) = 0$. This equation is solved together with Eqs. (2.1) and (2.2) in order to calculate the total moment of inertia, which can be rewritten as

$$I = \frac{c^2}{G}\frac{w(R)R^3}{6 + 2w(R)}. \tag{2.9}$$

The fraction of crust moment of inertia can also be calculated as [LHS19]

$$\begin{aligned}\frac{I_{crust}}{I} &= 1 - \frac{I_{core}}{I} \\ &= 1 - \left(\frac{R_{core}}{R}\right)^3\frac{w(R_{core})}{w(R)}\exp\left[-\int_{R_{core}}^R \frac{w(r)}{r}dr\right],\end{aligned} \tag{2.10}$$

Figure 2.3: Moment of inertia I (upper panel) and fraction of crust moment of inertia I_{crust}/I (lower panel) as a function of the NS mass M for several popular EoS calculated within the metamodeling technique. In the upper panel, the black dotted line marks the NS canonical mass, that is $1.4 M_{\odot}$. In the lower panel, the minimum values needed to justify Vela glitches with (Delsate *et al.* [Del+16] and Andersson *et al.* [And+12]) and without (Link *et al.* [LEL99]) crustal entrainment are represented.

where we have introduced the moment of inertia of the core I_{core}, defined by the integration of Eq. (2.5) up to the core radius $R = R_{core}$.

The total moment of inertia is plotted as a function of the NS mass in the upper panel of Fig. 2.3 for EoS based on Skyrme-type functionals BSk24, SLy4, and BSk14, and relativistic models PKDD and TM1. For $M = 1.4 M_{\odot}$, it is found that I ranges from $\approx 1.2 \times 10^{45}$ g cm^2 for the soft BSk14 EoS to $\approx 2 \times 10^{45}$ g cm^2 for the very stiff TM1 EoS. This shows the strong dependence on the EoS. More particularly, an apparent positive correlation with L_{sym} is observed. It is seen that the model dependence is even larger for high-mass NS.

The lower panel of Fig. 2.3 shows the variation with NS mass of I_{crust}/I for the same EoS. It is seen that the more massive a NS is, the less moment of inertia it stores in its crust, which follows the trends observed in Fig. 2.2. This was predictable from the sensitivity of crustal properties to the CC transition pressure. Given the selected EoS, the value of I_{crust}/I at $M = 1.4 M_{\odot}$ ranges from $\approx 2\%$ for BSk14 to $\approx 5\%$ for TM1, showing once again the dramatic dependence on the EoS.

2.1.2.2 Connection to pulsar glitches

The so-called pulsar glitches are sudden jumps in the rotational frequency of a compact star. They are thought to originate from an abrupt transfer of angular momentum from the liquid interior, acting as an angular momentum reservoir, to the solid crust of the star due to the unpinning of the superfluid vortices from the crystal lattice [AI75]. This occurs when the differential lag between the slower solid crust and faster superfluid vortices reach some threshold and can no longer be sustained, so as to recover a close equilibrium between the two. Eventually, stresses start to build up again, ultimately leading to another glitch event.

At the time of writing, 555 glitches have been observed in 190 pulsars through high-precision pulsar timing [Esp+11; Jod]. For a given glitcher, three quantities are usually measured: its spin frequency Ω, its average spin-down rate $\dot{\Omega}$, and its glitch activity parameter $\mathcal{A}$, defined as

$$\mathcal{A} = \frac{1}{t} \sum_{i=1}^{N} \frac{\Delta \Omega_i}{\Omega}, \tag{2.11}$$

where $\sum_i \Delta \Omega_i / \Omega$ represents the cumulative spin-up rate over the N glitches occurring during a time t.

It was demonstrated in [LEL99] that the ratio of the moment of inertia associated to the neutron superfluid which drives the glitches I_{sf} to the moment of inertia of the solid crust – plus any portion of the star strongly coupled to it – I_c must satisfy

$$\frac{I_{sf}}{I_c} \geq \frac{\Omega}{|\dot{\Omega}|} \mathcal{A} \equiv \mathcal{G}, \tag{2.12}$$

where we have introduced the coupling parameter $\mathcal{G}$. In view of relating the observational constraint $\mathcal{G}$ to the fractional moment of inertia I_{crust}/I to ultimately set a constraint on the stellar EoS, we assume that the angular momentum reservoir is confined to the neutron superfluid coexisting with the crystal lattice of the inner crust. In that case, we have $I_c = I - I_{res} \simeq I$ and $I_{crust} \simeq I_{sf}$, yielding [LEL99]

$$\frac{I_{sf}}{I_c} \simeq \frac{I_{crust}}{I} \geq \mathcal{G}. \tag{2.13}$$

In reality, the neutron superfluid is strongly coupled to the solid crust due to nondissipative entrainment effects [Cha13], limiting the amount of angular momentum that can be transferred during a glitch event. The importance of the entrainment coupling is related to the neutron effective mass m_n^* in the inner crust, which is proportional to the ratio of unbound neutrons to those that are not entrained, $m_n^* \equiv m_n n_g / n_g^c$. Taking into account the entrainment effects, the previous constraint, Eq. (2.13), then becomes [And+12]

$$\frac{I_{crust}}{I} \geq \mathcal{G} \frac{\langle m_n^* \rangle}{m_n}, \tag{2.14}$$

with $\langle m_n^* \rangle$ the average effective neutron mass. It should be stressed that systematic calculations of m_n^* throughout the NS crust are very costly from the computational point of view and that, following [And+12; PFH14], we adopt the value $\langle m_n^* \rangle / m_n = 4.3$, which

is inferred from the results of [Cha12]. Naturally, one recover the expression without crustal entrainment in the case of $\langle m_n^* \rangle = m_n$. We should stress that the importance of the effect of crustal entrainment, that is the value of the average neutron effective mass throughout the solid crust, is currently under debate [MU16; WP17].

The Vela pulsar (PSR B0833-45) is one of the most active glitchers known, with glitches occurring four times per decade on average. Since the beginning of its monitoring, almost than 50 years ago, it has exhibited 20 glitches in total [Jod], allowing for a precise estimation of the corresponding the coupling parameter, $\mathcal{G}_{\text{Vela}} = (1.62 \pm 0.03) \times 10^{-2}$ [Ho+15]. This can be translated into a constraint for the fraction of crust moment of inertia,

$$\left(\frac{I_{crust}}{I}\right)_{\text{Vela}} \geq (1.62 \pm 0.03) \times 10^{-2} \frac{\langle m_n^* \rangle}{m_n} \approx 0.07. \tag{2.15}$$

In other words, in the standard picture where the angular momentum reservoir is exclusively confined to the neutron superfluid permeating the inner crust, the crust must store more than 7% (with entrainment effects included) of the total moment of inertia in order to justify the large glitches occurring in the Vela pulsar.

The Vela constraints on I_{crust}/I are displayed in the lower panel of Fig. 2.3. Neglecting entrainment effects [LEL99], it is seen that the constraint is easily satisfied. For BSk14 EoS, which is the softest EoS here, it leads to $\approx 1.6 M_\odot$ for the maximum mass of Vela. Now including crustal entrainment with $\langle m_n^* \rangle / m_n = 4.3$ [And+12], it is not clear, due to dependence on the EoS, whether the superfluid neutron in the crust can carry enough angular momentum to explain Vela glitches. For the three nonrelativistic Skyrme-based EoS that we consider, we see that the constraint is unlikely to be satisfied, because it would require Vela mass to be very low, $M_{\text{Vela}} \lesssim 0.9 M_\odot$. While theoretically plausible [HPY07], such low-mass NS have never been observed to this day. On the other hand, it is observed that very stiff EoS such as TM1 can be consistent with the constraint [PFH14]. Finally, given the constraint on the fractional moment of inertia calculated with the present largest estimation of crustal entrainment [Del+16] (black thick line), we find that the inferred mass of Vela is at most $\approx 0.85 M_\odot$ for the stiff TM1 EoS and $\approx 0.65 M_\odot$ for the soft EoS based on Skyrme functionals. Clearly the question "*Is the crust enough?*" deserves further investigations. In that sense, it will be addressed in 2.3.3 in the context of a complete statistical analysis [CGM19b].

2.1.3 Tidal deformability

The tidal deformability describes how much a body is deformed by tidal forces, which arise when two massive bodies orbit each other. The simplest example corresponds of course to the Moon causing the tides observed in Earth's oceans. The detection of gravitational radiation emitted by inspiraling binary NS is possible using ground-based GW detectors such as LIGO and Virgo. Shortly before merging, once the relative distance between the stars is small enough, the tidal distortion of the NS becomes so large that, in some cases (in strongest signals), it becomes possible to infer the tidal deformability from the GW signal. Theoretically, the tidal deformability parameter is the observable which makes the link between the EoS and the gravitational signal. In that sense, GW observations can ultimately provide new constraints on the EoS. In

particular, the first detection of GW from the coalescence of two NS, the GW170817 event, has yielded a value for the tidal deformability of a $1.4M_\odot$ NS [Abb+18].

Let us consider a static, spherically symmetric NS, placed in a static external quadrupolar tidal field $\mathcal{E}_{tid}$. The induced quadrupole moment of this star is given by

$$Q_{tid} = -\lambda\mathcal{E}_{tid}, \tag{2.16}$$

where λ is the tidal deformability, which is related to the so-called tidal Love number k_2 by

$$\lambda = \frac{2}{3}k_2\left(\frac{Rc^2}{G}\right)^5. \tag{2.17}$$

Let us also define the dimensionless tidal deformability,

$$\Lambda = \frac{\lambda}{M^5} = \frac{2}{3}k_2\beta^{-5}, \tag{2.18}$$

where we have introduced the compactness of the star $\beta = GM/(Rc^2)$. Similarly to the moment of inertia in the slow rotation approximation, k_2 can be obtained from the solution of the following first-order differential equation [Hin+10],

$$
\begin{aligned}
\frac{dy}{dr} =\ & -\frac{y^2}{r} - \frac{y-6}{r-2Gm/c^2} \\
& -\frac{4\pi G}{c^2}r^2\frac{(5-y)\rho_B + (9+y)P/c^2 + (P+\rho_B c^2)/c_s^2}{r-2Gm/c^2} \\
& +\frac{1}{r}\left[\frac{2G}{c^2}\frac{(m+4\pi pr^3/c^2)}{r-2Gm/c^2}\right]^2,
\end{aligned}
\tag{2.19}
$$

where we have introduced the speed of sound $c_s = \sqrt{\partial P/\partial\rho_B}$, and that must satisfy the boundary condition $y(r=0) = 2$. This equation together with the hydrostatic equilibrium equations, Eqs. (2.1) and (2.2), are solved simultaneously. The tidal Love number reads

$$k_2 = \frac{8}{5}\beta^5(1-2\beta)^2[2-y(R)+2\beta(y(R)-1)]/a, \tag{2.20}$$

with

$$
\begin{aligned}
a =\ & 6\beta[2-y(R)+\beta(5y(R)-8)] \\
& +4\beta^3[13-11y(R)+\beta(3y(R)-2)+2\beta^2(1+y(R))] \\
& +3(1-2\beta)^2[2-y(R)+2\beta(y(R)-1)]\ln(1-2\beta).
\end{aligned}
\tag{2.21}
$$

Fig. 2.4 shows the variation with NS mass of k_2 for the several popular EoS that we consider in this chapter. The tidal Love number measures how easily the bulk of the matter in a NS is deformed. In the case of the mass being concentrated at the center of the star, the tidal deformation is small, and so is k_2. In agreement with [Hin+10], we find that k_2 lies in the range $\approx 0.05 - 0.15$. The relative difference between the present EoS is of the order of $\approx 35\%$ for $M = 1.4M_\odot$, showing once again the dramatic
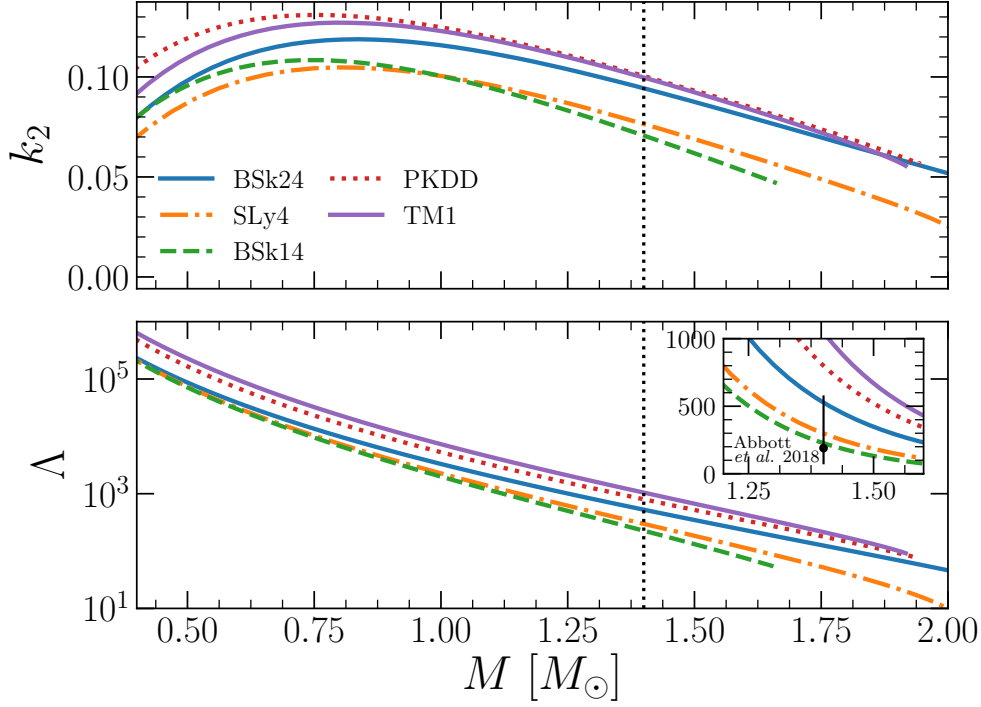
Figure 2.4: Tidal Love number k_2 (upper panel) and dimensionless tidal deformability Λ (lower panel) as a function of the NS mass M for several popular EoS calculated within the metamodeling technique. The black dotted line marks the NS canonical mass, that is $1.4 M_\odot$. In the inset of the lower panel, the value $\Lambda_{1.4} = 190^{+390}_{-120}$ (at 90% level) inferred from GW170817 event is represented [Abb+18].

dependence on the EoS. Let us point out that the tidal Love number is very sensitive to the description of the crustal component of the EoS [PF19].

The dimensionless tidal deformability is plotted as a function of M in the lower panel of Fig. 2.4. In the mass range considered, it is seen that the more massive the NS is, the less it gets deformed when orbiting another massive compact object. In the inset, we show the value of the dimensionless tidal deformability for a $1.4 M_\odot$ NS inferred from the GW170817 event, $\Lambda_{1.4} = 190^{+390}_{-120}$ at the 90% level. We can observe that the EoS which predict the largest tidal effects, PKDD and TM1, are unlikely. One can notice the tug or war between the tendency of wanting soft EoS, typically based on nonrelativistic Skyrme-type functionals, which predict small tidal deformations, and wanting very stiff EoS, typically based on relativistic models, to explain the glitch phenomenon as a transfer of angular momentum from the neutron superfluid confined in the crystal lattice to the solid crust.

2.2 Bayesian determination of the equation of state parameters

In recent years, there has been a lot of efforts invested in the development of the chiral EFT [DHS16] with the aim of providing new constraints on the low-density EoS. As we have already discussed, the maximum observed mass of NS [Ant+13; Cro+20] establishes a stringent constraint on the EoS. Furthermore, and for the same reason, future observations of GW signatures associated to binary NS mergers with LIGO and Virgo, and radius measurements from NICER will beneficial. Bayesian inference is a statistical method which allows to account both for the present day knowledge on nuclear physics and NS observables for predicting the stellar matter EoS.

This section deals with the Bayesian determination of the EoS parameters. The general formalism of Bayesian inference is recalled and its application for constraining the EoS is explained in 2.2.1. In 2.2.2, we give the prior distribution of EoS parameters and a sensitivity analysis of the CC transition point is carried out afterwards. The likelihood function, based on constraints on nuclear physics observables, constraints on NS observables, and physical requirements, is constructed in 2.2.3. Finally, we present the posterior distribution of empirical parameters in 2.2.4. A particular attention is paid to the correlations among parameters.

2.2.1 Principle of Bayesian inference

The core of Bayesian inference is based on well-known Bayes' theorem, which provides an expression for the conditional probability (or posterior probability) of A given B,

$$P(A|B) = \frac{P(B|A)P(A)}{P(B)}. \tag{2.22}$$

In this equation, $P(B|A)$ is the conditional probability of B given A, $P(A)$ is the prior probability of A, and $P(B)$ that of B. In the model form of Bayes' theorem, one replaces B by data, A with a parameter set $\boldsymbol{X}$, and P with probability density functions (PDF) p, resulting in [SS06]

$$p(\boldsymbol{X}|\text{data}) = \frac{p(\text{data}|\boldsymbol{X})p(\boldsymbol{X})}{p(\text{data})}. \tag{2.23}$$

The denominator is not a distribution but a normalization constant which makes sure that the posterior distribution $p(\boldsymbol{X}|\text{data})$ is a true probability distribution, by ensuring that the sum of the distribution is equal to 1. It is given by

$$p(\text{data}) = \int p(\text{data}|\boldsymbol{X})p(\boldsymbol{X})d\boldsymbol{X}. \tag{2.24}$$

The model-based formulation of Bayes' theorem, Eq. (2.23), is therefore often written as

$$p(\boldsymbol{X}|\text{data}) \propto p(\text{data}|\boldsymbol{X})p(\boldsymbol{X}). \tag{2.25}$$

The marginal one- and two-parameter posterior distributions can be extracted from the posterior distribution. Then are defined respectively as

$$p(X_j|\text{data}) = \left\{\prod_{i\neq j}\int dX_i\right\} p(\boldsymbol{X}|\text{data}), \qquad (2.26)$$

$$p(X_j, X_k|\text{data}) = \left\{\prod_{i\neq j,k}\int dX_i\right\} p(\boldsymbol{X}|\text{data}). \qquad (2.27)$$

Let us describe the different components of Bayesian inference. The prior distribution $p(\boldsymbol{X})$ represents our knowledge or bias on the model parameters. It can thus be more or less informative. $p(\text{data}|\boldsymbol{X})$ is the likelihood of observing the data given the model parameters $\boldsymbol{X}$. It is determined from the data comparison between the model and the measurement via an error estimator. In that sense, the link between the data and the model parameters is encoded in the likelihood distribution. Multiplying the prior by the likelihood function, one obtains the unnormalized joint posterior PDF, which corresponds to the conditional distribution of model parameters $\boldsymbol{X}$ given the data. Let us notice that the prior distribution affects the posterior distribution.

Bayesian inference is an appealing statistical method in the sense that it allows to calculate the joint posterior distribution of model parameters using prior beliefs updated with the likelihood. In the context of NS physics, and from the nuclear physicist point of view, it allows for instance to update our knowledge on the nuclear EoS by taking into consideration the data arising from various astrophysical observations, that are for example the NS mass inferred from Shapiro delay or the tidal deformability from GW measurements. Conversely, one can account for nuclear physics constraints in the prediction of macroscopic observables related to NS. In our case, we first generate a large number of EoS, each of them being defined by a set of parameters $\boldsymbol{X}$, to numerically sample the prior parameter distribution. Then, we filter those EoS through constraints, which arise from physical requirements, astrophysical observations, and ab initio calculations of SNM and PNM. This gives us the joint posterior distribution of model parameters, from which we can finally calculate the posterior EoS and make general predictions for NS observables. Those predictions are presented in Section 2.3.

Let us describe the parameter set $\boldsymbol{X}$. Our calculation of the stellar EoS is based on the metamodeling of nuclear matter energy [MHG18a] introduced in 1.2.1.1. The empirical parameters E_{sat}, n_{sat}, K_{sat}, Q_{sat}, Z_{sat}, E_{sym}, L_{sym}, K_{sym}, Q_{sym}, and Z_{sym} – which we recall are given by the successive derivatives of the NM energy at saturation density in isoscalar and isovector sectors – therefore enter into the parameter set. The parameter b is also added in order to explore different functional behaviors close to the $n \to 0$ limit. The parameter b, together with the isoscalar effective mass m^*_{sat}/m and isospin splitting $\Delta m^*_{sat}/m$, completes the parameter space, associated to the description of bulk matter. In the solid crust, the metamodeling technique is supplemented by a surface plus curvature term in order to describe the surface properties of finite nuclei. Thus, one could consider adding the surface and curvature parameters, respectively σ_0, b_s, p, and σ_{0c}, β, as extra parameters to $\boldsymbol{X}$. However, we have seen in Fig. 1.5 that the χ^2 function, which evaluates the goodness of the fit of those parameters to experimental nuclear masses given BSk24 empirical parameters and $p = 3$, is strongly peaked on a

Parameter	Unit	N	Min	Max
E_{sat}	MeV	0	-17	-15
n_{sat}	fm^{-3}	1	0.15	0.17
K_{sat}	MeV	2	190	270
Q_{sat}	MeV	3	-1000	1000
Z_{sat}	MeV	4	-3000	3000
E_{sym}	MeV	0	26	38
L_{sym}	MeV	1	10	80
K_{sym}	MeV	2	-400	200
Q_{sym}	MeV	3	-2000	2000
Z_{sym}	MeV	4	-5000	5000
m^*_{sat}/m			0.6	0.8
$\Delta m^*_{sat}/m$			0.0	0.2
b			1	10

Table 2.2: Minimum value and maximum value of each of the parameters of parameter set $\boldsymbol{X}$. The associated unit and derivative order N are also reported.

given set $\boldsymbol{S} = \boldsymbol{S_{opt}}$. We expect this feature to be recovered for every model and we therefore choose to not include the surface and curvature parameters in $\boldsymbol{X}$ but to take the set $\boldsymbol{S_{opt}}$ that minimizes χ^2, as explained in 1.2.1.2. It is important to stress that, even if we keep only the optimized values for the surface and curvature parameters for each parameter set, a large parameter space is explored because of the large variation of the bulk properties and the physical correlation between surface and bulk due to the fit to experimental data. We consider two choices for the value of the parameter p, which determines the behavior of the surface tension for extreme isospin values. Either it is fixed to the educated value $p = 3$, or $p = \{2.5, 3, 3.5\}$ is selected for each set of empirical parameters. The latter option is considered for the determination of observables that are sensitive to the CC transition point, which we have seen is strongly correlated to the isovector properties of the surface tension.

2.2.2 Prior distribution of equation of state parameters

We now discuss the prior distribution of empirical parameters. We first give insights concerning the selected intervals for the flat prior. A sensitivity analysis of the CC transition point is performed afterwards.

2.2.2.1 Flat prior compatible with empirical constraints

The prior distribution of $\boldsymbol{X}$ is given by an uncorrelated ansatz and an uniform distribution of each parameter within the interval specified in Table 2.2,

$$p(\boldsymbol{X}) = \prod_{i=1}^{2(N+1)+3} \mathcal{U}(X_i^{min}, X_i^{max}; X_i), \tag{2.28}$$

where the parameter X_i is uniformly distributed from X_i^{min} to X_i^{max}. The use of a flat prior means that all possible values of $\boldsymbol{X}$ inside the intervals are equally likely a priori.

The range of variation for the model parameters reflect the degree of uncertainty on the EoS parameters, as measured by their variation in the functionals which reproduce successfully low energy nuclear physics data [MHG18a]. We can distinguish three groups of empirical parameters, depending on how well they are experimentally constrained. The first group consists of the low-order isoscalar parameters E_{sat}, n_{sat}, K_{sat}, the symmetry energy at saturation density E_{sym}, as well as the effective mass m_{sat}^* and isospin splitting $\Delta m_{sat}^*/m$. These parameters are rather well determined by nuclear experiments, with associated relative uncertainties lower than 15%. The second group consists of the parameters that are still poorly determined by nuclear experiments. The uncertainties on the isoscalar skewness Q_{sat}, the slope of the symmetry energy L_{sym}, and the isovector incompressibility K_{sym} are very large, yet one can expect a better accuracy to be reached in the near future. In particular, the determination of L_{sym} is an highly topical issue nowadays [Li+14]. Finally, the last group concerns the parameters which are inaccessible by nuclear experiments to the present day, that is the isovector sqewness Q_{sym} as well as the parameters of order $N = 4$, Z_{sat} and Z_{sym} In consequence, we explore very large ranges for these parameters.
The choice of the interval for the low-density parameter, $b = [1, 10]$, is discussed thoroughly in [Ant+19].

2.2.2.2   Sensitivity analysis of the crust-core transition point[*]

Let us recall that one of the advantages of the metamodeling approach is that all the EoS model parameters, such as the empirical parameters, are a priori uncorrelated. It is therefore possible to vary each one of them independently of the others, which is not feasible using specific functional behaviors such as Skyrme, Gogny, or the different versions of RMF, as discussed in detail in [MHG18a; MG19]. Indeed, common functionals describing infinite NM have a smaller number of parameters compared to the metamodel, which creates a priori correlations that are not fully controlled. If we take the example of Skyrme forces, the density dependence of SNM is controlled by only three parameters, which are fixed to reproduce the coordinates of the saturation point: n_{sat}, E_{sat}, and K_{sat}. Thus, the isoscalar skewness Q_{sat} is correlated with the three other parameters, and it turns out that this correlation is not the same, for instance, in Skyrme, Gogny, or in RMF functionals [MG19]. A similar argument applies to the symmetry energy: when the density dependence of the symmetry energy is governed by a single parameter as assumed in heavy ion transport models, an isosoft behavior at suprasaturation density is necessarily associated to an isostiff behavior at subsaturation density, while more complicated behaviors are possible [MG19]. The independent variation of the different empirical parameters allows a simple determination of the most influential parameters impacting a given observable under study.

Such a sensitivity analysis is presented in Fig. 2.5 for the CC transition density n_t and transition pressure P_t. The reference metamodel used in the sensitivity analysis can

---
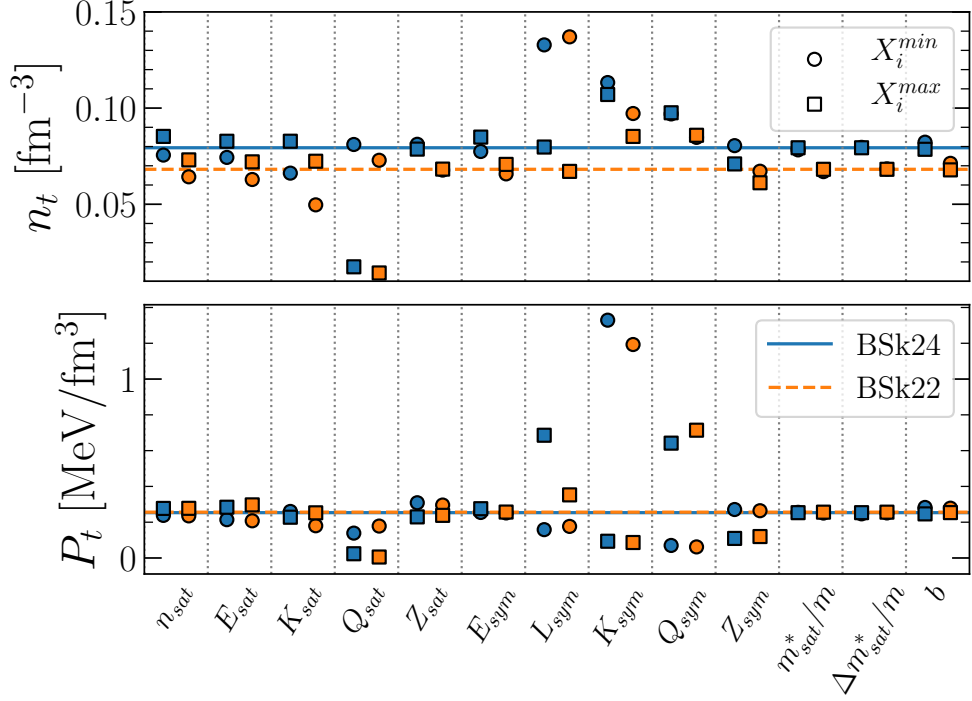
Figure 2.5: Sensitivity analysis of the transition density n_t (upper panel) and transition pressure P_t (lower panel) with respect to EoS parameters. $p = 3$ is fixed and two different reference point are chosen: BSk24 parameters (solid blue lines) and BSk22 parameters (orange dashed lines). For each parameter, the symbols on left (blue) correspond to BSk24 and those on right (orange) to BSk22. Circles and squares are respectively associated to the minimum value X_i^{min} and maximum value X_i^{max} of the parameter, which are listed in Table 2.2.

have an influence. For this reason, the sensitivity analysis varying one by one the EoS parameters is performed around two different reference parameter sets $\boldsymbol{X_{ref}}$, namely the parameter set corresponding to the BSk24 functional (solid blue lines), and the one corresponding to the BSk22 functional (dashed orange lines). For both of them, we fix $p = 3$ as well as $b = 10 \ln(2)$.

The range of variation for each of the EoS parameters correspond to the intervals for the prior distribution $p(\boldsymbol{X})$ specified in Table 2.2. Let us however notice that some sets produce nonviable EoS, for which a solution for the CC transition point cannot be found. This occurs in particular when varying the value of the isovector incompressiblity parameter K_{sym} with BSk24 as reference parameter set. Indeed, we find an extremely soft behavior for the symmetry energy for the minimum value $K_{sym}^{min} = -400$ MeV. In that very situation, we increase the minimum value of the parameter to $K_{sym}^{min} \approx -300$ MeV so as to find a solution for n_t and P_t.

The symbols in Fig. 2.5 give the transition density and pressure domain obtained

when the EoS parameters are one by one varied around the reference model, within the interval of Table 2.2. More specifically, circles and squares are respectively associated to the minimum value and maximum value of each parameter. Since the uncertainty on the different parameters is not the same, the relative distance between circles and squares is a qualitative measurement of the propagation of the uncertainty on the transition point brought by each parameter. We can see that the sensitivity of each parameter depends on the value of the other parameters, that is on the chosen reference set $\boldsymbol{X_{ref}}$. Still, universal trends clearly emerge. We can see that the CC phase transition, at variance with the standard liquid-gas of SNM, is virtually insensitive to isoscalar parameters. Even if extremely large variations of Q_{sat} and Z_{sat} are considered, see Table 2.2, the influence of the isoscalar parameters in the transition pressure is almost negligible, and it is a bit larger for n_t but still smaller than the isovector parameters. This underlines the importance of the energetics of the neutron gas on the transition point. Concerning the isovector sector, we can see that L_{sym} is the most important parameter as far as the transition density is concerned. This result is in agreement with previous findings by many authors [Duc+11] and was already anticipated in 1.2.6. The symmetry energy at saturation E_{sym} and the effective mass splitting $\Delta m^*_{sat}/m$ do not play any role on the transition, which can be partially explained by the fact that these parameters are already relatively well constrained. The transition density and pressure show also a great sensitivity to the isovector incompressibility parameter K_{sym}. This can explain why the transition pressure exhibits an irregular behavior when plotted as a function of L_{sym} (see Fig. 1.13): the different functionals considered in the literature have very different values of K_{sym}, which blurs the correlation with L_{sym}. This effect is also amplified by the fact that, depending on the reference point, the dependence of P_t with L_{sym} is not monotonic. Finally, we can notice that the influence of the fully unknown high-order derivatives Q_{sym} and Z_{sym}, though less important than the one of L_{sym}, is not negligible and comparable to the one of the isovector surface energy parameter p that can be inferred from Fig. 1.13. We have checked that similar conclusions can be drawn if the sensitivity analysis is performed using the definition of the transition point from the dynamical spinodal [Ant+19].

2.2.3 Determination of the likelihood function

The likelihood function corresponds to the probability of observing the data given the model parameters $\boldsymbol{X}$. In the context of our analysis, it is defined as

$$p(\text{data}|\boldsymbol{X}) = w_{LD}(\boldsymbol{X}) \times w_{HD}(\boldsymbol{X}) \times p_{\text{AME2016}}(\boldsymbol{X}). \qquad (2.29)$$

In this expression, w_{LD} and w_{HD} are strict filters that concentrate on constraining the low-density EoS and high density EoS, respectively. Both filters are given by sharp δ functions that output 1 if the constraint is satisfied, and 0 otherwise. Constraints on nuclear physics observables, yielding the filter w_{LD} and the probability p_{AME2016} are presented in 2.2.3.1. In 2.2.3.2, we present the constraints corresponding to the filter w_{HD}, which are associated to general physical requirements and measurements of NS observables.
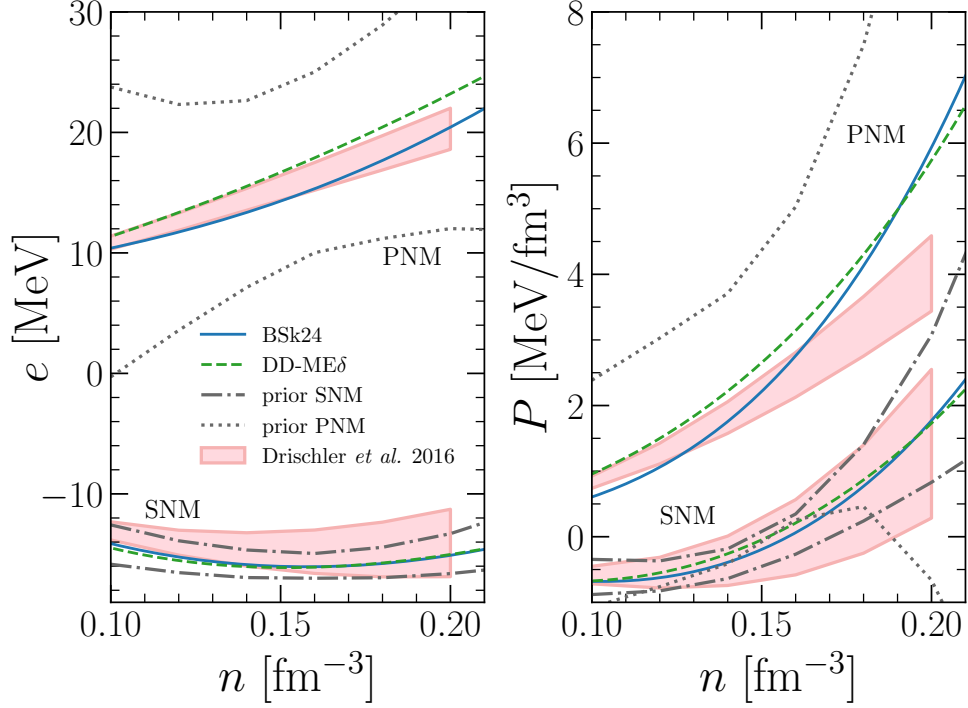
Figure 2.6: Energy per nucleon (left panel) and pressure (right panel) as a function of density for both SNM and PNM from chiral ETF calculations of [DHS16] (pink bands). The predictions of BSk24 and DD-MEδ functionals are represented in solid blue lines and dashed green lines, respectively. The gray lines give the minimum and maximum values of the prior distribution.

2.2.3.1   Constraints on nuclear physics observables

Let us concentrate first on the strict filter w_{LD}, hereafter referred to as low-density (LD) filter. It is introduced to verify whether the metamodel associated to a set of parameter $\boldsymbol{X}$ is compatible with the recent chiral EFT calculations for SNM and PNM by Drischler *et al.* [DHS16]. The authors have calculated the energy per particle for several values of isospin at low density within the many-body perturbation theory, based on a set of seven different Hamiltonians with chiral NN and three-nucleon interactions.

The resulting predicted bands for energy per nucleon as well as pressure of SNM and PNM are shown in Fig. 2.6 (pink bands), together with the predictions of the popular BSk24 (solid blue lines) and DD-MEδ (green dashed lines) functionals. The pressure band is calculated by taking the density derivative of the energy per nucleon for the seven Hamiltonians, thus only few density dependencies of the pressure are explored. This can explain why even realistic models such as BSk24 are not compatible with the theoretical band for the pressure of PNM above $\approx n_{sat}$. It is therefore debatable whether we should add the chiral EFT bands for pressure of NM in our list of constraints defining our pass-band filters w_{LD}. In the following, we will not consider this particular constraint

by default, yet we will still investigate how it affects the posterior distribution EoS in 2.3. In the context of the pass-band filter w_{LD}, the chiral ETF predicted bands are widened by 5% in order to account for other existing ab initio calculations in an effective manner. In addition, we will not apply the filter in the low-density region $n < 0.10$ fm^{-3} because the width of the band becomes extremely small, causing numerical issues.

The minimum values and maximum values of the prior distribution are also represented in Fig. 2.6 (gray lines). Let us notice that one can the infer the posterior band graphically by the comparison with the chiral ETF bands. Interestingly, the graphically inferred posterior band of the prior energy per nucleon and pressure of SNM around saturation density is narrower than the one corresponding to the ab initio calculation. The reason is that low energy nuclear physics experiments provide strong empirical constraints for SNM [MHG18a], which have been embedded effectively in the intervals for the empirical parameters of the prior distribution in Table 2.2. The same is not true for the PNM case. Indeed, the present day knowledge on the empirical parameters of the isovector sector is insufficient. For this reason, we can see that the corresponding ab initio bands are very thin in comparison to the prior distribution.

We now turn the calculation of the probability p_{AME2016}, which describe the ability of the CLDM defined from a parameter set $\boldsymbol{X}$, to fit the measured nuclear masses of the AME2016 [Hua+17]. The goodness of fit is evaluated by the reduced χ^2, Eq. 1.62. We can define the associated likelihood probability as

$$p_{\text{AME2016}}(\boldsymbol{X}) = \exp\left[-\frac{1}{2}\chi_\nu^2(\boldsymbol{X})\right].\tag{2.30}$$

2.2.3.2 Physical requirements and constraints on neutron star observables

The filter w_{HD}, hereafter referred to as high density (HD) filter, is applied subsequently to the LD filter w_{LD}. It imposes general physical constraints to the global density behavior of the functional, as follows:

- the positiveness of the symmetry energy at all densities,

- the stability of the EoS,

- the causality condition, $0 < c_s/c < 1$,

- the maximum observed NS mass, $M_{max}(\boldsymbol{X}) \geq M_{max}^{obs}$,

where $M_{max}(\boldsymbol{X})$ is the maximum mass supported by the EoS calculated for a parameter set $\boldsymbol{X}$, and M_{max}^{obs} is the maximum observed NS mass. By default we choose $M_{max}^{obs} = 1.97 M_\odot$, which corresponds to a 1σ conservative estimate, based on the observation of PSR J0348+0432 [Ant+13]. Let us however notice that it does not correspond to the mass of the heaviest NS observed to the present day [Cro+20]. The reason is that the observation of PSR J0740+6620 with $M = 2.14^{+0.10}_{-0.09} M_\odot$ is very recent and it was not yet published at the time of this study.

The possibility of a negative symmetry energy at high density was sometimes mentioned in the literature [Li17; WFF88]. However, extremely soft functionals are generally incompatible with the maximum mass constraint, thus relaxing the condition of the positiveness of the symmetry energy will not alter our results.

Finally, let us notice that we do not include the constraint on the tidal deformability inferred from the GW170817 event [Abb+17] in the w_{HD} filter, the reason being that we are interested in confronting our results with the observations of LIGO and Virgo.

2.2.4 Posterior distribution of equation of state parameters

We now turn to the description of the joint posterior distribution of equation of state parameters. The effect of the different filters on marginalized one-parameter probabilities both for isoscalar and isovector parameters is analyzed in 2.2.4.1. Correlations among empirical parameters are extracted from the Bayesian analysis in 2.2.4.2.

2.2.4.1 Marginalized one-parameter posterior distributions of empirical parameters

The marginal one-parameter probabilities can be evaluated from the joint posterior distribution $p(\boldsymbol{X}|\text{data})$ using Eq. (2.26). The generated PDF for isoscalar and isovector empirical parameters of orders $N \leq 3$ are shown in Fig. 2.7 and 2.8, respectively. The effect of the different filters on the one-parameter PDF can be seen. We find that the likelihood probability p_{AME2016}, originating from the mass fit, has a negligible impact on the distributions. This can be understood from the fact that the prior distribution of empirical parameters already contains information provided by nuclear experiments. Hence, in all cases, the probability p_{AME2016} is accounted for in the evaluation of the PDF. The isovector surface tension parameter p is fixed to be $p = 3$ for this study, but the results presented in the following are unmodified if p is allowed to vary. The reason is that p is decoupled by construction from the homogeneous EoS parameters, and it additionally does not play any role in the mass fit, see Fig. 1.5, meaning that it is also independent of the other surface parameters. Five combinations of filters are considered:

- the LD only without the constraint on pressure (solid blue lines),

- the LD filter only with the constraint on pressure (dashdotted blue lines),

- the HD filter only with $M_{max}^{obs} = 1.97 M_{\odot}$ [Ant+13] (solid orange lines),

- the HD filter only with $M_{max}^{obs} = 2.05 M_{\odot}$ [Ant+13] (dashdotted orange lines),

- both LD and HD filters with the constraint on pressure, for $M_{max}^{obs} = 1.97 M_{\odot}$ (solid green lines).

By comparing the LD predictions in Fig. 2.7, it is seen that adding the pressure bands, predicted by chiral EFT [DHS16], as a constraint has a negligible effect on the posterior distributions of isoscalar empirical parameters. Since empirical information is available in SNM and included in our prior distribution, we observe that applying the LD filter does not impose strong constraints on the one-parameter PDF in the isoscalar sector. Still, we can notice that low values of E_{sat} and n_{sat} are disfavored by the passage through the chiral EFT predicted bands shown in Fig. 2.6. Conversely, it appears in 2.8 that applying LD constraints on the energy per nucleon have a enormous effect on the marginalized posterior distributions of the low-order isovector empirical parameters
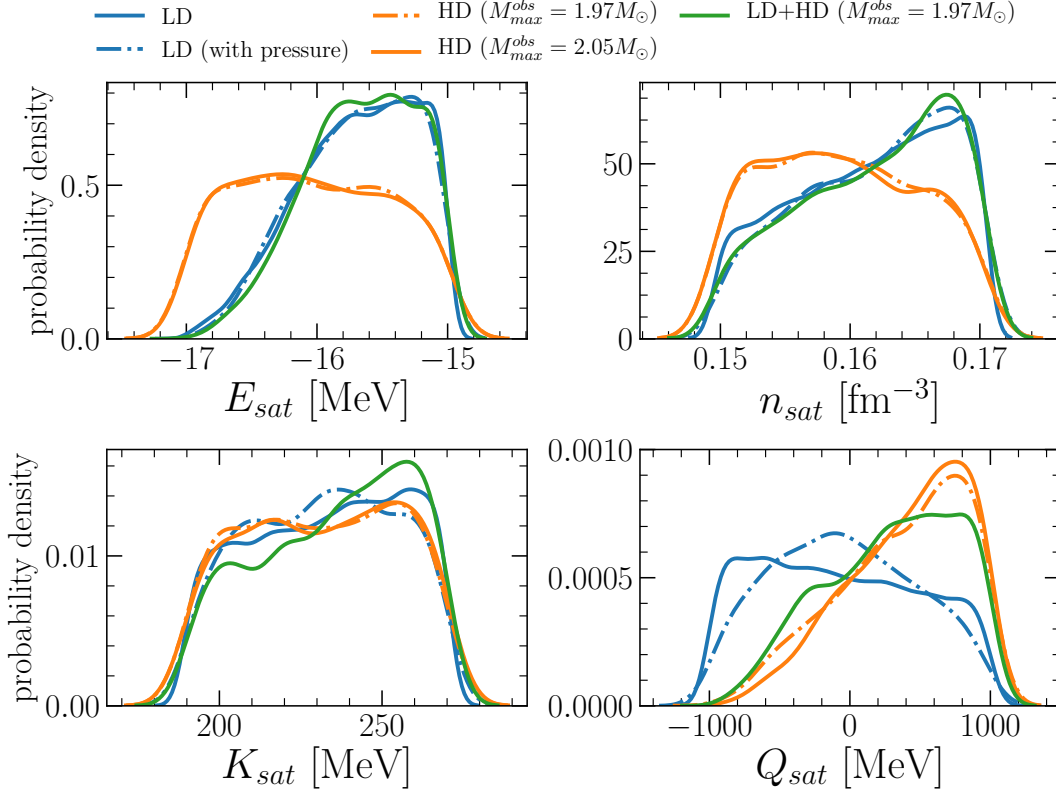
Figure 2.7: Marginalized posteriors for E_{sat}, n_{sat}, K_{sat}, and Q_{sat} for the sets passing through the LD filter without (solid blue lines) and with (dashdotted blue lines) the constraint on pressure, HD filter with $M_{max}^{obs} = 1.97 M_\odot$ [Ant+13] (solid orange lines) and with $M_{max}^{obs} = 2.05 M_\odot$ [Cro+20] (dashdotted orange lines), and both filters without the constraint on pressure, for $M_{max}^{obs} = 1.97 M_\odot$ (solid green lines). In all cases, the likelihood probability $p_{AME2016}$ is accounted for and $p = 3$ is fixed.

E_{sym} and L_{sym}, shown in the two upper panels. The effect on the posterior PDF of L_{sym} is even larger if we impose the sets to be compatible with the chiral EFT predicted bands for pressure of SNM and PNM. It also allows very tight determination of isovector incompressibility K_{sym}, its distribution being peaked at $K_{sym} \approx -200$ MeV, while it is rather flat without the constraint on pressure. Overall, we see that the posterior probabilities for these parameters are narrower than those without the additional constraints on pressure. These observations can be easily understood with the following expression for the pressure of PNM in the vicinity of the saturation density n_{sat},

$$P_{PNM}(n) = P_{HM}(n, \delta = 1) \simeq \frac{1}{3} n_{sat}(1 + 3x)^2 (K_{sat}x + L_{sym} + K_{sym}x), \qquad (2.31)$$

which gives $P_{PNM}(n = n_{sat}) = n_{sat}L_{sym}/3$ at the saturation point. The posterior distributions of Q_{sat} and Q_{sym} are only very slightly affected by the LD constraints.
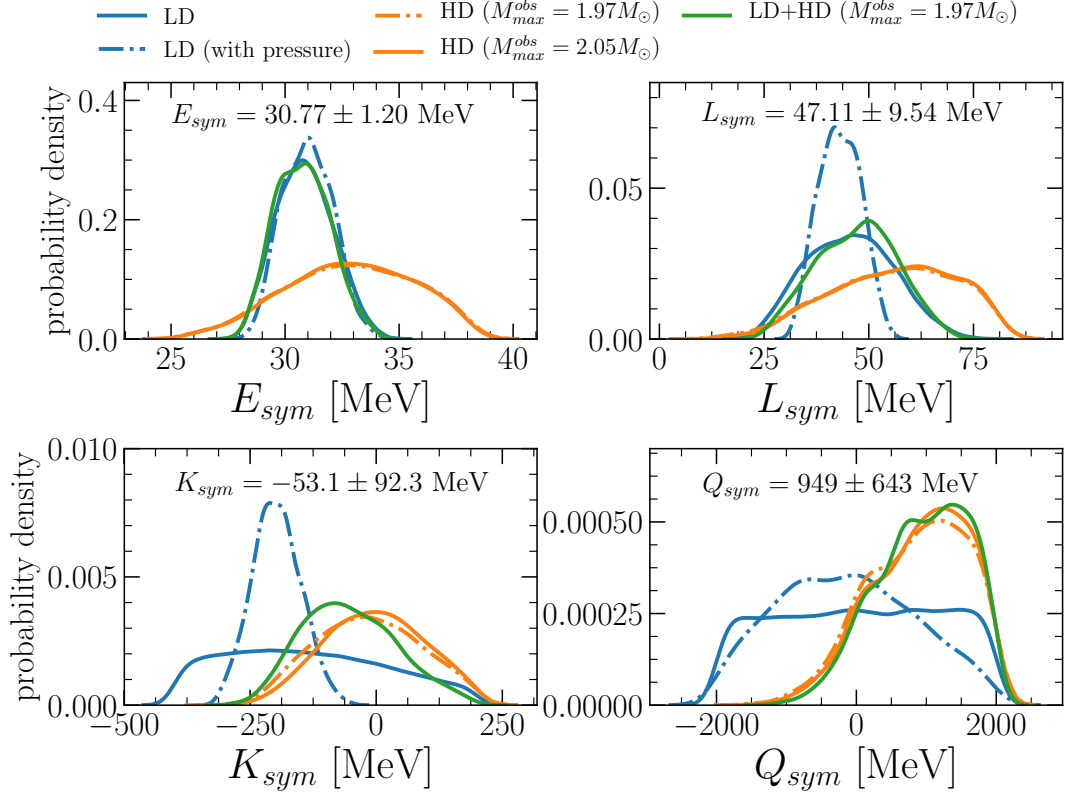
Figure 2.8: Marginalized posteriors for E_{sym}, L_{sym}, K_{sym}, and Q_{sym} for the sets passing through the LD filter without (solid blue lines) and with (dashdotted blue lines) the constraint on pressure, HD filter with $M_{max}^{obs} = 1.97 M_\odot$ [Ant+13] (solid orange lines) and with $M_{max}^{obs} = 2.05 M_\odot$ [Cro+20] (dashdotted orange lines), and both filters without the constraint on pressure, for $M_{max}^{obs} = 1.97 M_\odot$ (solid green lines). The resulting mean value and uncertainty, corresponding to the latter option, are shown for each parameter. In all cases, the likelihood probability p_{AME2016} is accounted for and $p = 3$ is fixed.

The same is true for parameters of order $N = 4$, Z_{sat} and Z_{sym}, which are not shown in the figures. The reason is that the high-order parameters contribute to the EoS at suprasaturation densities, which are not accessible with chiral EFT yet.

The one-parameter PDF for the sets passing through the HD pass-band filter w_{HD} are represented in orange lines. Overall, we find that the effect of varying the value M_{max}^{obs}, so as to be compatible with to the two considered observations of heavy NS [Ant+13; Cro+20], is very small. In the isoscalar sector, we can see the distributions of the low-order parameters E_{sat}, n_{sat} and K_{sat} are not affected by the passage through the w_{HD} filter. On the other hand, it has an important effect on the PDF of Q_{sat}, with large values being favored. In the isovector sector, the HD filter has a significant impact on the PDF of E_{sym}, L_{sym} and K_{sym}, yet less effective than that of the LD filter, except for the K_{sym}. Concerning the isovector skewness parameter Q_{sym}, which we recall is not

Figure 2.9: Correlation matrix for the empirical parameters of orders $N \leq 3$ for the sets passing through the LD filter without (left) and with (right) the constraint on pressure. The likelihood probability p_{AME2016} is accounted for and $p = 3$ is fixed.

affected by the LD filter, we find negative values to be very unlikely. Overall, we can see that HD constraints favor stiff EoS with respect to the LD predictions. The reason is obviously that stiff EoS are desired in order to verify the maximum mass constraint.

The generated one-parameter PDF associated to the sets passing through the combination of both LD and HD filters without the constraint on pressure, for $M_{max}^{obs} = 1.97 M_{\odot}$, are plotted in solid green lines. The mean value and standard deviation application of LD and HD constraints are given for each of the isovector parameters.

Let us notice that the marginalized posteriors for the effective mass m_{sat}^*/m and the isospin splitting $\Delta m_{sat}^*/m$ are not displayed here. As for the low-density parameters in the isoscalar sector, these quantities are already well constrained by nuclear experiments. Hence the associated posteriors distributions are very close the prior distributions. The marginalized posterior probability for low-density parameter b is close to the prior distribution as well. This point can be understood from the fact that none of the filters concern the $n \to 0$ limit.

2.2.4.2 Correlations among empirical parameters

We now turn to explore the correlations between empirical parameters, as obtained by applying the different conditions. As in 2.2.4.1, $p = 3$ is fixed, and the likelihood probability $p_{AME2016}$ is accounted for in all cases.
Given a pair of parameters (X_i, X_j), the Pearson correlation coefficient is calculated as

$$r_{ij} = \frac{\text{cov}(X_i, X_j)}{\sigma_{X_i} \sigma_{X_j}}, \tag{2.32}$$

Figure 2.10: Correlation matrix for the empirical parameters of orders $N \leq 4$ for the sets passing through both LD and HD filters without the constraint on pressure, for $M_{max}^{obs} = 1.97 M_{\odot}$ [Ant+13]. The likelihood probability p_{AME2016} is accounted for and $p = 3$ is fixed.

where $\text{cov}(X_i, X_j)$ is the covariance and σ_{X_i} (σ_{X_j}) is the standard deviation of the parameter X_i (X_j).

In Fig. 2.9, we find that many correlations appear due to the LD constraints. The left panel of the figure shows the correlation matrix for the empirical parameters of orders $N \leq 3$ for the sets passing through the LD filter without applying the constraint on pressure arising from chiral EFT. We find an anticorrelation between E_{sat} and E_{sym}, and a positive correlation between E_{sym} and n_{sat}. More interesting correlations among the different isovector parameters are induced by the constraint of reproducing the ab initio EFT calculations. Indeed, we recover the correlation between E_{sym} and L_{sym}, which has been already observed by many authors using different models [LH19; Kor+12; DL14; TCV08; CGS14]. We also observe a strong correlation between L_{sym} and K_{sym} and find that E_{sym} is slightly anticorrelated to K_{sym}.

The correlation matrix calculated from the joint posterior distributions of parameters for the sets passing through chiral EFT predicted bands both for energy per nucleon and pressure of NM is displayed in right panel of Fig. 2.9. Several differences with respect to the matrix in the left panel can be noticed. Among the isovector parameters, it is seen that the previously found correlation between the slope of the symmetry energy L_{sym} and

the isovector incompressibility K_{sym} disappears in favor of a strong correlation between K_{sym} and the isovector sqewness Q_{sym}, and an anticorrelation between L_{sym} and Q_{sym}. We also observe that the isoscalar parameters K_{sat} and Q_{sat} are weakly correlated with the corresponding isovector ones K_{sym} and Q_{sym}. These nontrivial correlations can only be revealed within the metamodeling strategy, because in usual functionals, such as Skyrme ones, the high-order parameters are a priori strongly correlated from the functional form.

In both cases studied in Fig. 2.9, the fourth order parameters Z_{sat} and Z_{sym} do not show any correlation with any other parameter, showing their negligible influence on the density relatively close to saturation implied in the LD filter. Similarly, the isoscalar effective mass and effective mass splitting are also essentially uncorrelated with the others. The reason is that variations of these parameters, which play a crucial role in the structure of finite nuclei, are fully compensated by variations of the density derivatives as long as only the total energetics, that is kinetic plus potential, is involved [Cha+17].
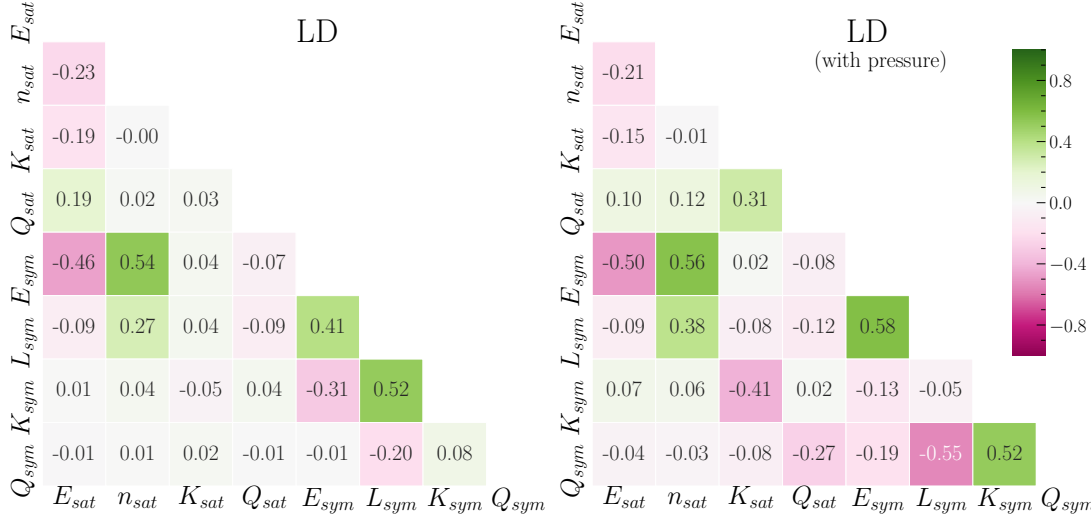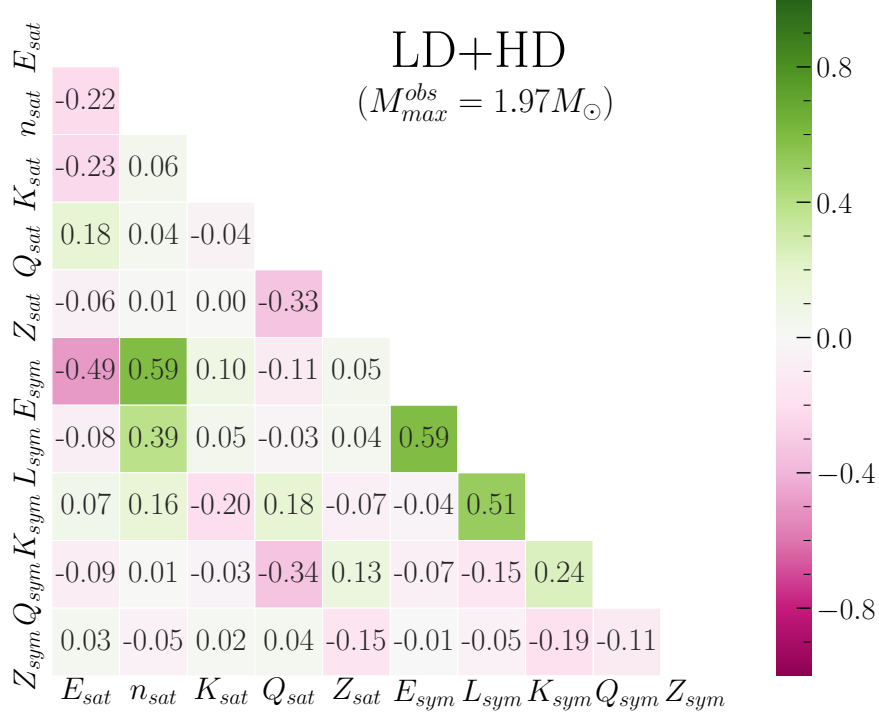
Fig. 2.10 shows the correlation matrix for the empirical parameters of orders $N \leq 4$ for the sets passing through both LD and HD filters without the constraint on pressure, for $M_{max}^{obs} = 1.97 M_\odot$ [Ant+13]. One can identify the correlations induced by the application of HD filter by comparison with the left panel of Fig. 2.9. Doing so, we infer that the w_{HD} pass-band filter does not induce any correlation among the empirical parameters, with the exception of Q_{sat} being now slightly anticorrelated to Q_{sym} and Z_{sat}.

2.3 General predictions for neutron star observables

This section deals with general predictions for NS observables, based on the Bayesian analysis performed in Section 2.2. The marginalized posterior for the observable $\mathcal{O}$,

$$p(\mathcal{O}|\text{data}) = \left\{ \prod_{i=1}^{2(N+1)+3} \int dX_i \right\} \mathcal{O}(\boldsymbol{X}) p(\boldsymbol{X}|\text{data}), \qquad (2.33)$$

can be extracted from the joint posterior distribution of empirical parameters $p(\boldsymbol{X}|\text{data})$, where $\mathcal{O}(\boldsymbol{X})$ is the value of the observable $\mathcal{O}$ as obtained with the parameter set $\boldsymbol{X}$. Our predictions for global properties of the NS are presented and confronted with popular models as well as GW170817 event in 2.3.1. The Bayesian determination of the CC transition density and pressure is carried out in 2.3.2. Finally, in 2.3.3, we calculate the fraction of crust moment of inertia for the joint posterior distribution of parameters in order to investigate whether *the crust in enough* to explain pulsar glitches in the standard picture presented in 2.1.2.2.

2.3.1 Global properties: confrontation with popular models and the GW170817 event

A large number of EoS models, based for instance on Skyrme functionals or relativistic mean-field models, have been proposed in the literature over the years. Astrophysical observations can provide strong constraints on the nuclear EoS and therefore allows to discriminate between the different models. For instance, we have seen from that the observations of massive pulsars require from the EoS to support $M_{max} \gtrsim 2M_\odot$ [Dem+10;
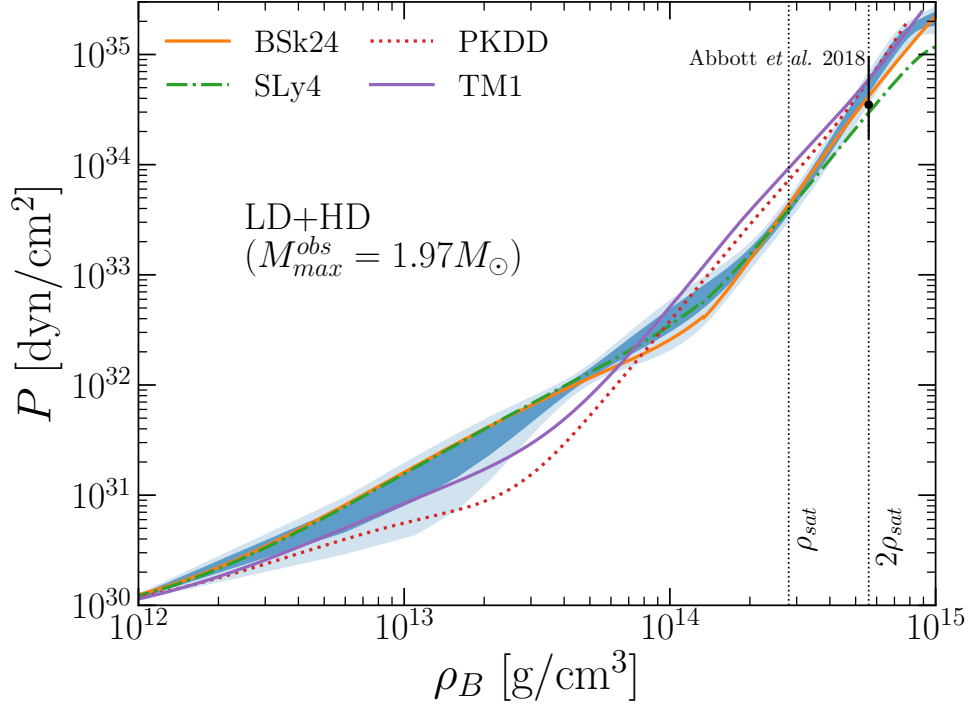
Figure 2.11: Marginalized posterior for the pressure P as a function of the baryon mass density ρ_B of the NS interior for the sets passing through both LD and HD filters without the constraint on pressure, for $M_{max}^{obs} = 1.97 M_\odot$ [Ant+13]. The likelihood probability p_{AME2016} is accounted for and $p = 3$ is fixed. The blue dark and light shaded regions show the 1σ and 2σ confidence intervals, respectively. The BSk24 (solid orange line), SLy4 (dashdotted green line), PKDD (dotted red line), and TM1 (solid purple line) unified EoS calculated within the metamodeling technique with $p = 3$ are represented. The recent constraint on $P_{2\rho_{sat}}$ inferred from GW170817 [Abb+18] is given.

Ant+13; Cro+20]. The recent GW170817 event, which is the first detection of GW from a binary NS coalescence, has provided a constraint on the NS tidal deformability [Abb+17; Abb+18; Abb+19].

In the following, we calculate global properties of NS from the LD+HD joint posterior distribution of parameters and confront our results with popular EoS models as well as GW170817 constraints provided by the LIGO and Virgo collaborations.

2.3.1.1 Equation of state

The 1σ and 2σ confidence regions for the posterior unified EoS, obtained from the sets passing through both LD and HD constraints, are shown in Fig. 2.11 along with two popular EoS calculated within the metamodeling technique, namely BSk24 (dashdotted orange line) and PKDD EoS (dotted green line). We can see that only the EoS based on

BSk24 functional is compatible, at 2σ, with the final LD+HD prediction in the whole density domain considered in the figure. It is observed that the SLy4 EoS deviates below the 2σ band at suprasaturation densities. The two EoS based on functionals issued from relativistic mean-field theory, namely PKDD and TM1, do not meet the final LD+HD predictions. The reason is that the ab initio calculations considered for our LD filter [DHS16] tend to favor soft EoS, typically based on Skyrme functionals, as we can see in Fig. 2.8. Indeed, we find $E_{sym} = 30.77 \pm 1.20$ MeV and $L_{sym} = 47.11 \pm 9.54$ MeV for the low-order isovector parameters for the LD+HD prediction, which is very close to the LD one for these parameters. The two relativistic functionals considered here, the empirical parameters of which are reported in Table 2.1, exhibit a very stiff behavior at saturation.

The recent constraint, provided by the observation of GW170817, on the pressure at twice nuclear saturation density, $P_{2\rho_{sat}} = 3.5^{+2.7}_{-1.7} \times 10^{34}$ dyn/cm^2 at the 90% level [Abb+18], is also shown in Fig. 2.11. We can see that this result is in very good agreement with our analysis. Let us notice that our predicted 2σ band at $2\rho_{sat}$ is very thin in comparison with the constraint arising from GW170817. This is because the ab initio calculations, not considered as a filter in [Abb+18], impose stringent constraints on the low-density EoS.

2.3.1.2   Masses and radii

In Fig. 2.12, we plot the 68%, 95% and 99% confidence regions for the mass-radius relation obtained from the Bayesian modeling of the EoS for the LD+HD prediction, using the marginalization principle, Eq. (2.33). The mass-radius relationship for the same popular EoS as in Fig. 2.11, namely the Skyrme-based BSk24 and SLy4 EoS, and relativistic PKDD and TM1 EoS, are represented. As we can see, only the BSk24 result (solid orange line) is compatible with our prediction at 95% credible level in the whole mass domain considered. The two relativistic models predict large radii compared to our prediction. The soft SLy4 EoS, while similar to BSk24 EoS at low density, predict too small radii by ≈ 1 km to meet the LD+HD prediction at $M = 2M_\odot$. Given the results presented in this figure and in Fig. 2.11, we therefore find that all known models considered would have been rejected by the filters except BSk24, which satisfy both LD and HD constraints.

Let us now confront our prediction for the radius of a canonical NS, $R_{1.4} = 12.88^{+0.53}_{-0.65}$ km (90% credible interval), with different constraints found in the literature. De *et al.* have performed a Bayesian parameter estimation for the tidal deformabilities and radii of NS from the observation of GW170817 within the approximation $R_1 = R_2$, R_1 being the radius of the heavier star and R_2 that of the lighter star, that is assuming an identical value for the radius of binary components. The authors found $R_{1.4} = 10.7^{+2.1}_{-1.6}$ km (90% credible interval) [De+18], which is in a very close agreement with the estimation of the LIGO/Virgo collaborations which use EoS-insensitive relations, $R_{1.4} \approx R_1 = 10.7^{+2.1}_{-1.5}$ km (90% credible interval) [Abb+18]. Using a parametrized EoS and imposing the constraint on the maximum mass $M^{obs}_{max} = 1.97M_\odot$, LIGO and Virgo collaborations further constrain $R_{1.4} \approx R_1 = 11.9^{+1.4}_{-1.4}$ km (90% credible interval). In all analyses, a uniform prior was used on the component masses. We find that our estimation of the canonical radius $R_{1.4}$ is compatible with these three analyses, even though we can notice
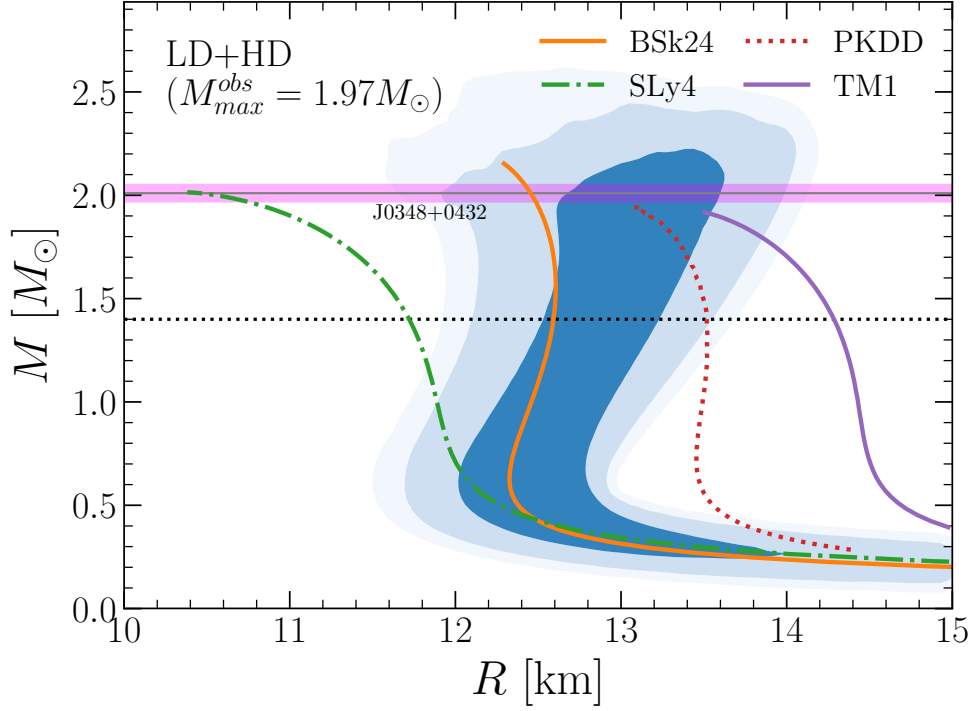
Figure 2.12: Marginalized posterior for the NS mass M as a function of the radius R for the sets passing through both LD and HD filters without the constraint on pressure, for $M_{max}^{obs} = 1.97 M_\odot$ [Ant+13] (magenta band). The likelihood probability $p_{AME2016}$ is accounted for and $p = 3$ is fixed. The blue shaded regions show the 68%, 95% and 99% confidence intervals. The mass-radius relation for the same popular EoS as in Fig. 2.11 are represented.

that the our value for the median is larger, and the 90% confidence interval is tighter. This outlines the importance of the LD filter in our calculation, which ensure that our posterior is compatible with chiral EFT predicted bands for the energy per nucleon of SNM and PNM. Moreover, our prior distribution of EoS parameters contains information arising from nuclear experiments. In [De+18; Abb+18], constraints on nuclear physics observables were not considered.

In Fig. 2.1, we have observed an apparent correlation between the radius of the star R and the slope of the symmetry energy L_{sym}, given five characteristic EoS models. This correlation has been highlighted recently in several studies, using EoS based either on Skyrme forces or relativistic mean-field models [Ala+16; Ji+19; Hu+20]. Surprisingly, for the LD prediction, we find that $R_{1.4}$ is especially correlated with the isovector incompressibility K_{sym}, $r(K_{sym}, R_{1.4}) = 0.69$ rather than with the L_{sym}, $r(L_{sym}, R_{1.4}) = 0.33$. As previously discussed in 2.2.2.2, the functional forms of Skyrme forces or relativistic models generally induce artificial correlations between some of the empirical parameters, with the effect of altering true correlations. The metamodeling technique prevents this

problem because no a priori correlation exists among the empirical parameters, so the true correlation are brought by the passage through LD and HD filters. For instance, correlations in the isovector sector between E_{sym} and L_{sym}, and between K_{sym} and $3E_{sym} - L_{sym}$, have been shown in [Mon+17; MG19] using a larger set of characteristic EoS models.

2.3.1.3   Tidal deformability

The tidal effects arising from a binary NS coalescence are encoded in the GW signal through the binary tidal deformability,

$$\tilde{\Lambda} = \frac{16}{13} \frac{(m_1 + 12m_2)m_1^4\Lambda_1 + (m_2 + 12m_1)m_2^4\Lambda_2}{(m_1 + m_2)^{1/5}}, \tag{2.34}$$

where $\Lambda_{1,2}$ are the individual NS tidal deformabilities, and $m_{1,2}$ the component masses satisfying the inequality $m_1 \geq m_2$. The binary tidal deformability is essentially correlated with the so-called chirp mass,

$$\mathcal{M} = \frac{(m_1 m_2)^{3/5}}{(m_1 + m_2)^{1/5}}. \tag{2.35}$$

For the specific case of GW170817, this quantity has been well constrained to $\mathcal{M}_{GW170817} = 1.188^{+0.004}_{-0.002} M_\odot$ [Abb+17]. The probability distributions for the component masses m_1 and m_2 are obtained from $\mathcal{M}_{GW170817}$ and the mass ratio m_2/m_1 (see Fig. 4 of [Abb+17]). The black dashed lines in Fig. 2.13 show the 50% and 90% confidence intervals as obtained by the LIGO and Virgo collaborations for the low-spin prior ($|\chi| < 0.05$, χ being the dimensionless spin), which is consistent with binary NS systems [Abb+19].

We show in Fig. 2.13 the 50% and 90% confidence regions corresponding to the joint probability distribution for Λ_1 and Λ_2 that we obtain for the sets passing through both LD and HD filters for the chirp mass $\mathcal{M}_{GW170817}$. The mass of the components have been sampled according to their respective individual probability distributions given in [Abb+17], and the same EoS have been used to calculate the individual tidal deformabilities. The part under the diagonal corresponds to the unphysical region $\Lambda_2 > \Lambda_1$ since the convention $m_1 \geq m_2$ has been taken. It is seen that our LD+HD prediction meets the results of the LIGO/Virgo collaborations at 90% confidence level, but we find that our posterior slightly favors larger values of $\Lambda_{1,2}$, that can be obtained with more stiff EoS, associated to less compact NS. The dimensionless tidal deformabilities are also calculated for the same four popular EoS as in Figs. 2.11 and 2.12. We observe that the soft SLy4 and BSk24 EoS are in a rather good agreement with the analysis of the LIGO and Virgo collaborations, whereas the relativistic models PKDD and TM1 seems very unlikely. Let us recall that yet such stiff EoS are required in order to explain the large glitches occurring in the Vela pulsar. Among the four popular EoS, only the one based on BSk24 functional is compatible with the LD+HD prediction.

The marginalized posterior distribution that we obtain for the dimensionless tidal deformability of a $1.4 M_\odot$ NS is shown in Fig. 2.14, along with the prediction of characteristic EoS based on Skyrme and relativistic models. The 90% confidence interval corresponding to the LD+HD prediction is $\Lambda_{1.4} = 634^{+204}_{-190}$. It meets the results of the
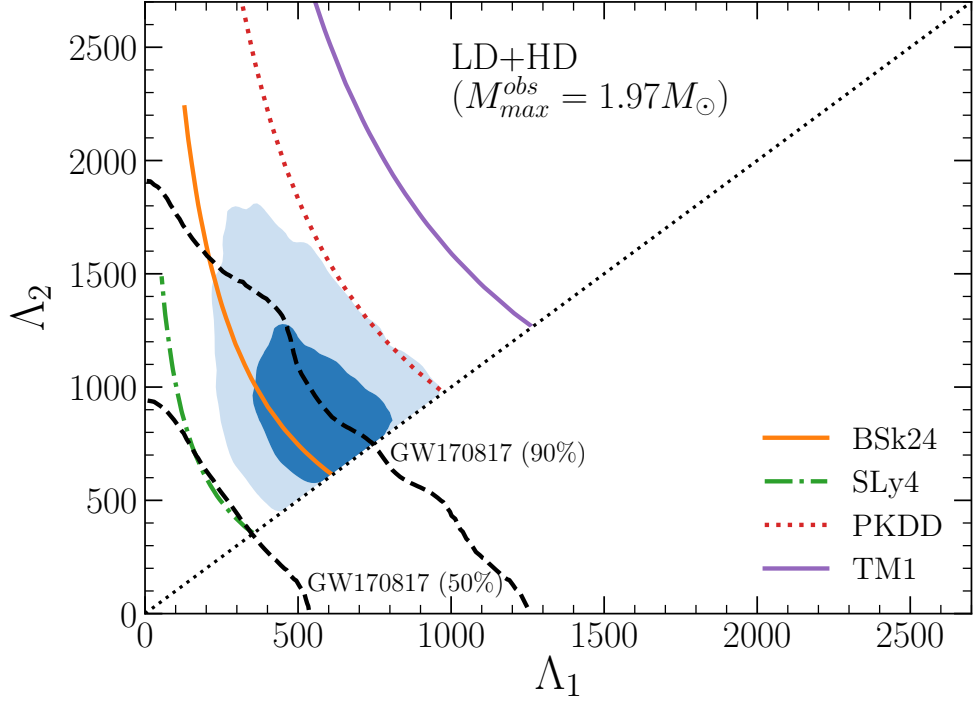
Figure 2.13: Marginalized posterior for Λ_1 (more massive component) and Λ_2 (less massive component) for the sets passing through both LD and HD filters without the constraint on pressure, for $M_{max}^{obs} = 1.97 M_\odot$. The value of the chirp mass corresponds to the specific case of GW170817, $\mathcal{M} = 1.188 M_\odot$, and the individual probability distributions for m_1 and m_2 are taken from [Abb+17]. Dark (light) shaded regions represents the 50% (90%) confidence interval with our Bayesian estimation with $p = 3$. The black dashed lines show the 50% and 90% confidence regions as obtained by LIGO/Virgo collaborations for the low-spin prior [Abb+18]. The $\Lambda_1 - \Lambda_2$ relation is also represented for the same popular EoS as in Fig. 2.11. The diagonal dotted line marks the $\Lambda_1 = \Lambda_2$ boundary.

LIGO/Virgo collaborations for GW170817, $\Lambda_{1.4} = 190_{-120}^{+390}$, the 90% confidence interval of which is given by the vertical dashed lines in the figure. However, we find that the probability for $\Lambda_{1.4} < 300$ is negligible. The shift of the median with respect to that inferred from GW170817 event outlines the importance of the LD filter in our calculation. Indeed, it is known that $\Lambda_{1.4}$ is strongly correlated to the NS radius $R_{1.4}$, we find a Pearson correlation coefficient of $r(R_{1.4}, \Lambda_{1.4}) = 0.98$, and we have seen that the radius of a $1.4 M_\odot$ NS is correlated with the isovector incompressibility parameter K_{sym}. Hence, we observe that K_{sym} and $\Lambda_{1.4}$ are correlated, with $r(K_{sym}, \Lambda_{1.4}) = 0.66$. We have seen in 2.8 that the isovector empirical parameters are strongly constrained by the ab initio calculations of NM, particularly when the constraint on pressure is accounted for in the LD pass-band filter. More specifically, we find that the isovector incompressibility is
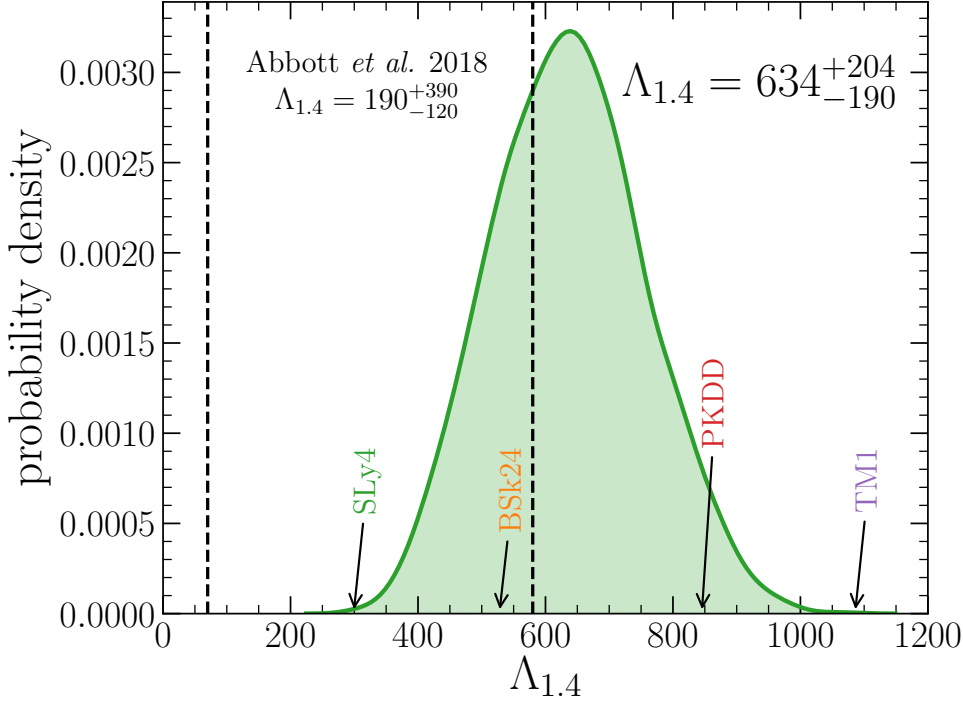
Figure 2.14: Marginalized posterior probability distribution for the dimensionless tidal deformability of a $1.4M_\odot$ NS, calculated for the sets passing through both LD and HD filters without the constraint on pressure, for $M_{max}^{obs} = 1.97M_\odot$. The resulting 90% credible interval is indicated in the top right corner. The arrows give the value of $\Lambda_{1.4}$ for four characteristic EoS: BSk24, SLy4, PKDD, and TM1. The vertical dashed lines delimit the 90% confidence interval associated to the constraint of the LIGO/Virgo collaborations for GW170817, $\Lambda_{1.4} = 190^{+390}_{-120}$ [Abb+18].

tightly determined in that case, with a distribution being peaked at $K_{sym} \approx -200$ MeV, therefore favoring soft EoS and in consequence smaller values of the tidal parameter $\Lambda_{1.4}$.

2.3.2 Bayesian analysis of the crust-core transition

The precise estimation of the CC transition point location, defined by Eq. (1.103), is important for the theoretical determination of NS static properties, such as the radius [For+16], for which accurate measurements will be available in the near future using hard x-ray timing techniques [Wat+16]. Furthermore, the computation of the crustal observables with the hydrostatic equilibrium equations requires the knowledge of the CC transition pressure P_t in addition to the EoS. In the following, we make quantitative predictions on the density and pressure of the CC transition point from the joint posterior distribution, and examine in details the influence of the different EoS parame-
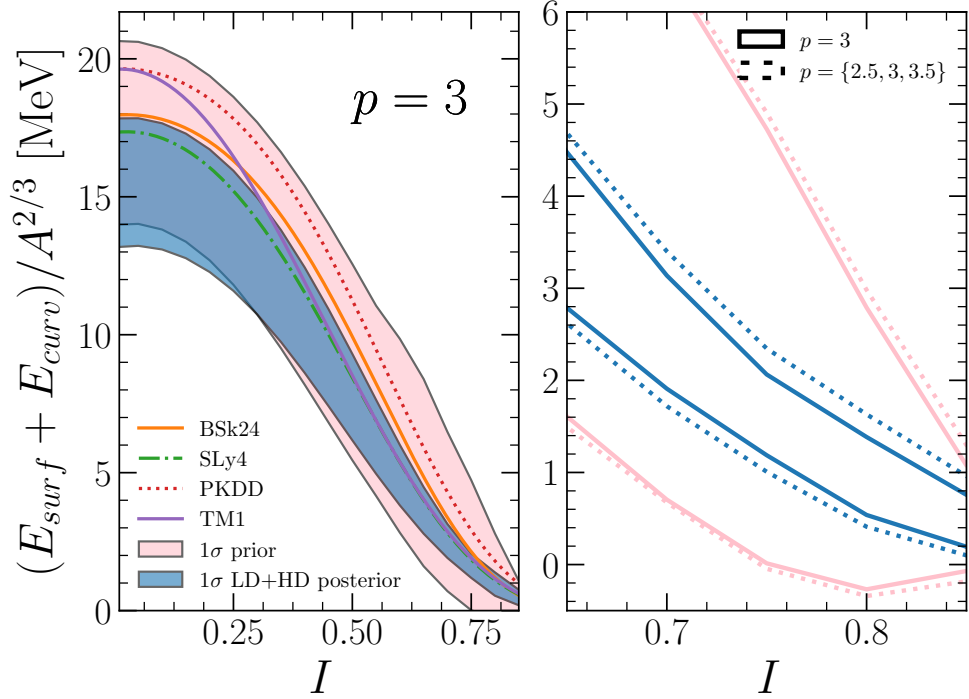
Figure 2.15: Left: 1σ prior (pink band) and LD+HD posterior distribution (blue band) for the surface plus curvature energy per surface nucleon, defined by Eqs. (1.58)-(1.61), as a function of the isospin asymmetry long the isobaric chain $A = 200$ for $p = 3$. The results for four characteristic EoS are also given. Right: 1σ prior and LD+HD posterior for $(E_{surf} + E_{curv})/A^{2/3}$ at high isospin for $p = 3$ (solid lines) and $p = \{2.5, 3, 3.5\}$ (dotted lines).

ters, as well as the effectiveness of the different filters entering the likelihood probability, Eq. (2.29).

Following the strategy introduced in 1.2.6, we calculate the CC transition properties from the crust, the description of which demands an explicit modeling of clusterized matter, thus the introduction of a surface (and eventually curvature) term in the energetics. This is done within the classical CLD approximation, using Eqs. (1.58)-(1.61). For a given set of empirical parameters, we expect that the theoretical determination of the CC transition point is sensitive to the surface energy at high isospin, which is essentially governed by the isovector surface parameter p, see Fig. 1.12. Unfortunately, experimental data are unavailable above $I = (N - Z)/A \gtrsim 0.3$ for the moment.

The prior and LD+HD posterior distribution for the surface plus curvature energy per surface nucleon are displayed in the left panel of Fig. 2.15 as a function of isospin asymmetry for the $p = 3$ case, along the isobaric chain $A = 200$. The variation with I of $(E_{surf} + E_{nuc})/A^{2/3}$ is also shown for four popular models. All of them are compatible with the 1σ band for to prior distribution. It is seen that the LD+HD distribution

predicts a low surface energy for nearly symmetric nuclei with respect to the prior distribution and the selected popular functionals. This is not surprising because we known that the surface parameter $\sigma_0 = \sigma(I = 0)$ is strongly anticorrelated with the energy per nucleon of SNM at saturation E_{sat} [CGM19a], for which large values are favored by the LD filter, see Fig. 2.7. Above the neutron drip line, $I \gtrsim 0.35$, we can see that the filters defining our likelihood probability allows a tight determination of the surface energy in comparison to the prior distribution. This translates into smaller uncertainties for the CC transition density and pressure.

The effect of allowing a distribution for the parameter p on the prior and LD+HD posterior distributions can be seen in the right panel of Fig. 2.15. In spite of the simple discrete ansatz $p = \{2.5, 3, 3.5\}$, we observe a continuous and smooth distribution of the surface tension. The reason is that the variation of the surface tension σ with p is continuous and smooth, and that the other surface parameters, which are fixed by the fit to experimental masses, have a continuous distribution. The effect of allowing a distribution for the parameter p does not modify the behavior of the surface energy in the vicinity of $I = 0$. However, above the drip line and particularly in the high isospin region, we can clearly observe that the uncertainties associated to the discrete ansatz are larger than those associated to $p = 3$ case. Let us notice that this effect is much more important in [CGM19a]. This can be understood from the fact that, in the latter study, curvature terms were not accounted for, and that the surface parameters were fitted to the spherical magic and semimagic nuclei ^{40,48}Ca, ^{48,58}Ni, ^{88}Sr, ^{90}Zr, ^{114,132}Sn, and ^{208}Pb, while the surface and curvature parameters are here fitted to the 2498 experimental masses of the AME2016 [Hua+17].

The correlation coefficients between the EoS parameters and the density and pressure at the CC transition point are calculated and reported in Fig. 2.16 for different joint distributions of parameters. For the prior distribution, which corresponds to the consideration of nuclear experimental constraints included as fully uncorrelated parameters sets, we observe that the most influential empirical parameters on n_t and P_t are the high-order parameters Q_{sat} and Q_{sym}. We also recover a small anticorrelation between the transition density and the L_{sym} parameter, as anticipated in 1.2.6. The transition density directly depends on the energy of beta-equilibrated matter. The transition pressure being linked to the first derivative of the energy density, it is not surprising to observe that P_t is rather slightly anticorrelated with K_{sym}. Since this parameter widely varies in existing functionals, this can explain why the present predictions of the transition pressure are so largely scattered, see Fig. 1.13. The HD filter does not impose further correlations between the transition quantities and the EoS with respect to the prior distribution, apart from tiny correlations with the isoscalar kurtosis Z_{sat}. We can see that the LD filter slightly reinforces the correlation of transition density and pressure with the isovector sqewness Q_{sym}. If the pressure filter, which allows a tight determination of the low-order isovector parameters, is also considered, the correlations with Q_{sym} are even stronger, $r(Q_{sym}, n_t) = 0.59$ and $r(Q_{sym}, P_t) = 0.74$. In addition, the anticorrelation between L_{sym} and P_t emerges, with $r(L_{sym}, P_t) = -0.40$. For our final LD+HD prediction with $p = 3$, we find that n_t is correlated with K_{sat} and Q_{sym}, and anticorrelated with Q_{sat}. A slight correlation with L_{sym} can also be seen. Concerning the transition pressure P_t, correlations with the isovector empirical parameters L_{sym}, K_{sym}

$$n_t$$

	E_{sat}	n_{sat}	K_{sat}	Q_{sat}	Z_{sat}	E_{sym}	L_{sym}	K_{sym}	Q_{sym}	Z_{sym}	p	σ_0	b_s	σ_{0c}	β
LD+HD	-0.11	-0.02	0.41	-0.51	0.25	-0.08	-0.26	-0.16	0.43	-0.14	0.11	0.11	0.15	-0.10	-0.08
LD+HD $p=3$	-0.10	-0.02	0.42	-0.51	0.24	-0.11	-0.29	-0.17	0.46	-0.16	0.00	0.10	0.21	-0.10	-0.13
LD (w/ P) $p=3$	-0.02	-0.05	0.12	-0.54	0.05	-0.06	-0.27	0.10	0.59	-0.11	0.00	0.02	0.09	-0.04	-0.06
LD $p=3$	-0.08	0.02	0.29	-0.48	0.07	-0.05	-0.20	-0.04	0.47	-0.10	0.00	0.08	0.13	-0.05	-0.11
HD $p=3$	0.23	0.07	0.30	-0.52	0.25	-0.16	-0.21	-0.06	0.33	-0.13	0.00	-0.23	-0.01	0.17	0.06
Prior $p=3$	0.17	0.06	0.25	-0.52	0.06	-0.01	-0.22	-0.12	0.32	-0.04	0.00	-0.18	-0.10	0.21	-0.03

$$P_t$$

	E_{sat}	n_{sat}	K_{sat}	Q_{sat}	Z_{sat}	E_{sym}	L_{sym}	K_{sym}	Q_{sym}	Z_{sym}	p	σ_0	b_s	σ_{0c}	β
LD+HD	-0.08	-0.00	0.31	-0.39	0.18	0.06	-0.26	-0.38	0.47	-0.14	0.12	0.07	0.11	-0.01	-0.07
LD+HD $p=3$	-0.07	-0.01	0.32	-0.39	0.18	0.05	-0.29	-0.41	0.49	-0.16	0.00	0.07	0.03	-0.01	-0.10
LD (w/ P) $p=3$	0.00	-0.02	0.11	-0.34	0.02	-0.09	-0.40	0.15	0.74	-0.13	0.00	-0.00	0.08	-0.00	-0.03
LD $p=3$	-0.04	0.02	0.19	-0.31	0.06	0.10	-0.19	-0.23	0.46	-0.08	0.00	0.03	-0.05	0.04	-0.06
HD $p=3$	0.22	0.05	0.27	-0.46	0.19	0.05	-0.16	-0.28	0.39	-0.14	0.00	-0.23	-0.17	0.26	-0.00
Prior $p=3$	0.15	0.03	0.19	-0.42	0.04	0.15	-0.05	-0.24	0.36	-0.04	0.00	-0.16	-0.20	0.24	-0.06

Figure 2.16: Correlation of the CC transition density n_t (upper panel) and pressure P_t (lower panel) with the empirical, surface, and curvature parameters for different distributions: prior, HD, LD, LD with pressure filter, and LD+HD joint posterior distributions for $p = 3$, and LD+HD joint posterior distribution for the discrete ansatz $p = \{2.5, 3, 3.5\}$.

and Q_{sym} are observed, as well as with K_{sat} and Q_{sat} in the isoscalar sector. It is seen that correlations of the transition quantities with the surface and curvature parameters are negligible in this study, even if the isovector surface parameter p is allowed to vary (lines "LD+HD"). This observation contrasts with some of the results of [CGM19a], in which important correlations between the transition quantities and the surface parameters were revealed. Once again, this is because the surface energy is better controlled in our calculation, as permitted by the introduction of curvature terms, supplemented by the fact that a larger pool of nuclear masses is used for the fit of surface and curvature parameters.

The joint distribution for n_t and P_t as well as the corresponding marginalized one-parameter probability distributions are shown in Fig. 2.17 for different filters. In the first five panels, the dashed lines delimit the 50% and 90% confidence regions, and the different symbols give the CC transition point as obtained with the popular models BSk24, SLy4, PKDD and TM1. In all cases and in agreement with [CGM19a], we find

Distribution	n_t (fm^{-3})	P_t (MeV/fm^3)
Prior	$0.062^{+0.028}_{-0.036}$	$0.225^{+0.379}_{-0.167}$
HD	$0.059^{+0.023}_{-0.029}$	$0.190^{+0.232}_{-0.120}$
LD	$0.073^{+0.025}_{-0.032}$	$0.281^{+0.478}_{-0.179}$
LD (with pressure)	$0.068^{+0.021}_{-0.021}$	$0.263^{+0.302}_{-0.149}$
LD+HD	$0.074^{+0.019}_{-0.033}$	$0.277^{+0.276}_{-0.168}$

Table 2.3: 68% confidence intervals for the CC transition density n_t and pressure P_t for different distributions: prior, HD, LD with and without the pressure filter, and LD+HD. In all cases, $p = 3$ is fixed.

that n_t and P_t are strongly correlated in all cases. The Pearson correlation coefficient is as high as $r = 0.92$ when using the LD filter with the constraint on pressure. We can observe in a graphical way that the LD and HD constraints lead to compatible predictions for the CC transition point. It is clearly seen that the most constraining filter for both n_t and P_t is the LD filter which account for the constraint on pressure ("LD (with pressure)"), ensuring the compatibility of the empirical parameters with the chiral ETF predicted bands for energy per nucleon and pressure of SNM and PNM [DHS16]. From the corresponding joint distribution, we obtain $n_t = 0.068^{+0.021}_{-0.021}$ fm^{-3} and $P_t = 0.263^{+0.302}_{-0.149}$ MeV/fm^3 at the 1σ confidence level. The passage through the HD filter has a significant impact on the distribution of P_t. We find that the resulting CC transition points, for three of the four popular models considered in this study, meet our final LD+HD prediction at the 50% confidence level. The 68% confidence intervals for the transition density and pressure for each of the considered distributions are reported in Table 2.3. The effect of varying p on the marginalized one-parameter distributions for n_t and P_t is displayed in the last panel of Fig. 2.17, for the LD+HD prediction. Overall, only minor differences are observed between the $p = 2.5$, $p = 3$ and $p = 3.5$ cases. We can see that the difference between the $p = 3$ and $p = 3.5$ cases is even smaller than that between $p = 2.5$ and $p = 3$ as far as the transition density was concerned, as it was expected from Fig. 1.12.

2.3.3 Pulsar glitches: answering the question "*Is the crust enough?*"

For a given EoS, the determination of the fraction of crust moment of inertia, using Eq. (2.10), and more generally of any crustal observable, is possible providing the location of the transition point to homogeneous matter. As discussed in 2.1.2.2, the NS crustal moment of inertia is related to the theoretical description of the glitch phenomenon, which consists of sudden spin-up of the rotational frequency of a NS. In the consensus view, a pulsar glitch is observed as the consequence of the angular momentum transfer from the neutron superfluid permeating the inner crust to the solid crust [AI75]. For a specific pulsar for which the coupling parameter $\mathcal{G}$ has been measured, and depending of the importance of the crustal entrainment effect [Cha13], the crust must therefore be sufficiently thick to store enough angular momentum. Naturally, it yields
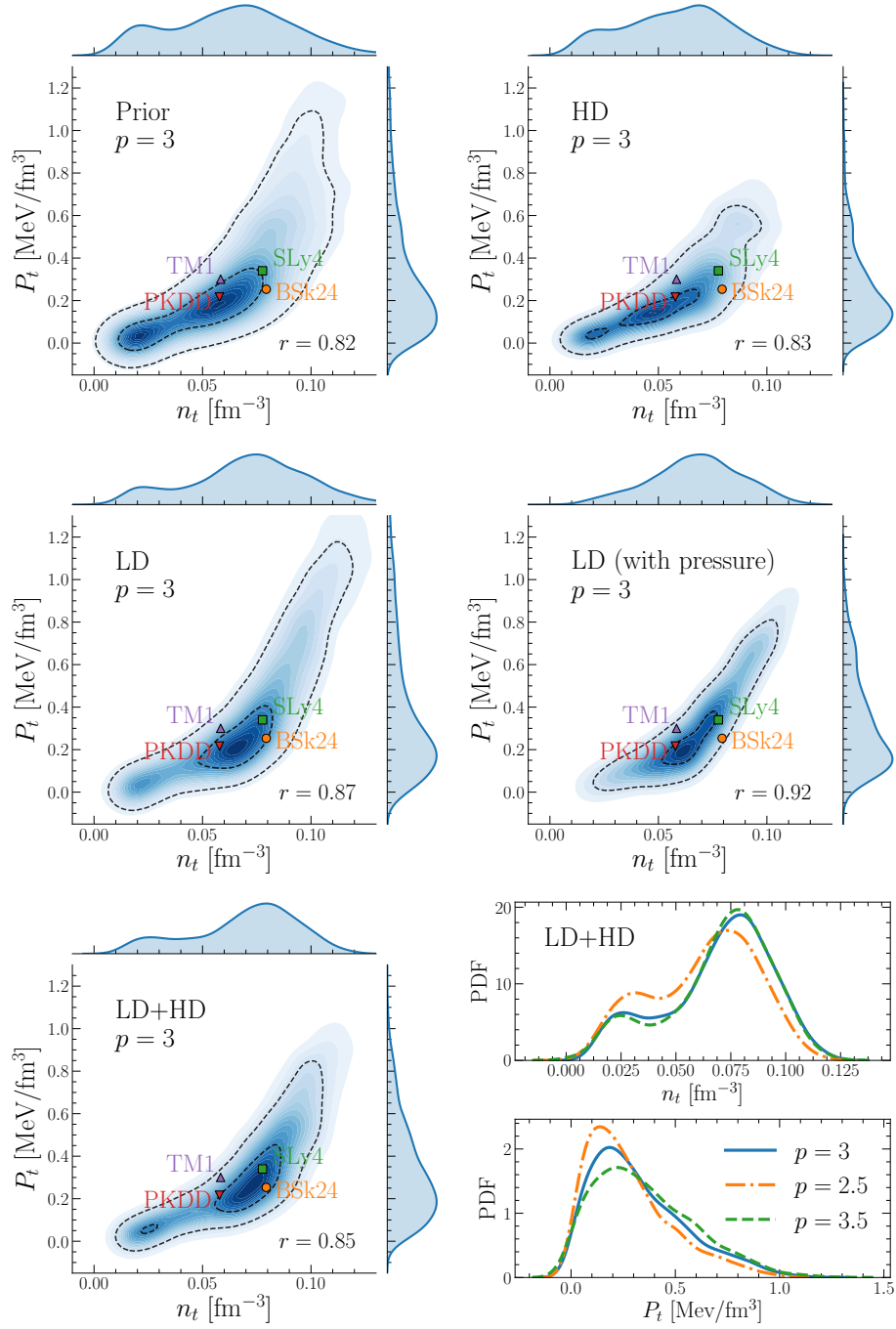
Figure 2.17: Marginalized probabilities for the transition density n_t and pressure P_t for different distributions. In the first five panels, the dashed lines delimit the 50% and 90% confidence regions. For each distribution, the Pearson correlation coefficient $r(n_t, P_t)$ is given. The results for four characteristic EoS are also shown.
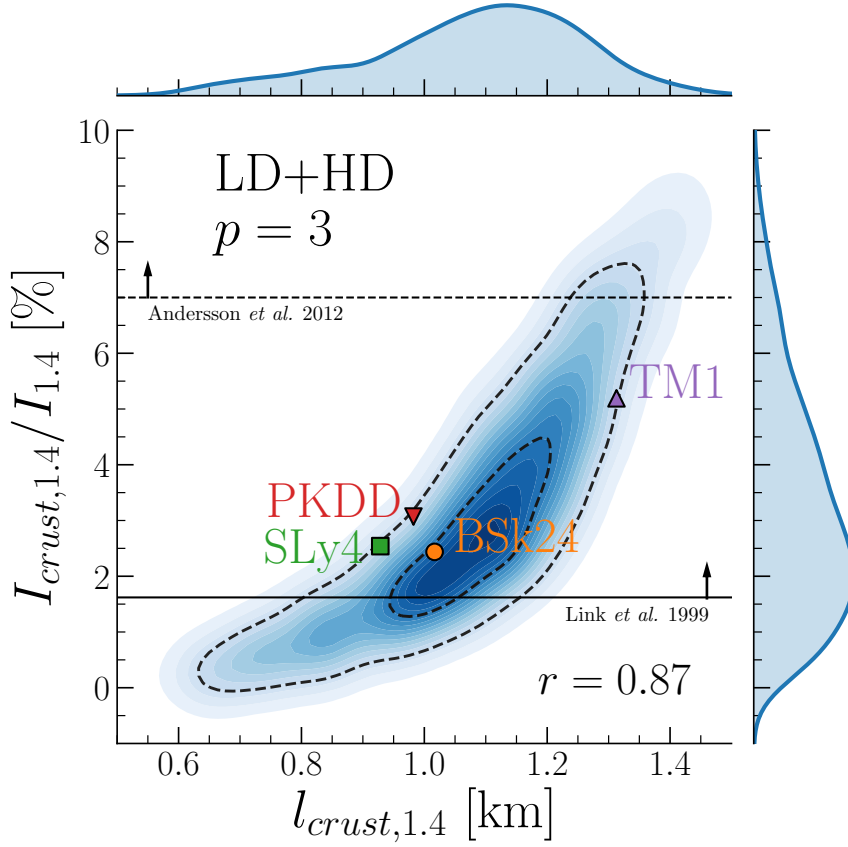
Figure 2.18: Marginalized probabilities for the crust thickness $l_{crust,1.4}$ and fraction of crust moment of inertia $I_{crust,1.4}/I_{1.4}$ for a $1.4 M_\odot$ NS, using the LD+HD distribution. The dashed lines delimit the 50% and 90% confidence regions. The Pearson correlation coefficient r is given. The symbols show the prediction of four characteristic EoS models. The minimum values needed to justify Vela glitches with (Andersson *et al.* [And+12]) and without (Link *et al.* [LEL99]) crustal entrainment are represented.

the question "*Is the crust enough?*", for which the answer is known to be very sensitive to the EoS [And+12; PFH14] and, most important to the CC transition density and pressure [CGM19b]. In the following, the crustal origin of pulsar glitches is discussed for the specific case of Vela, using the LD+HD joint posterior distribution of EoS parameters.

The strong correlation between the crust thickness and the fraction of crust moment of inertia for $M = 1.4 M_\odot$ is seen in Fig. 2.18. It means that the thicker the crust is, the more angular momentum is confined to the neutron superfluid coexisting with the crystal lattice of the inner crust. We obtain $l_{crust,1.4} = 1.11^{+0.14}_{-0.21}$ km and $I_{crust,1.4}/I_{1.4} = 2.89^{+2.51}_{-1.68}\%$ at the 1σ confidence level. The empirical parameters contributing the most to the uncertainty in the crust moment of inertia are, as for the transition density and pressure, the isovector incompressibility K_{sym} and sqewness Q_{sym}. As expected from
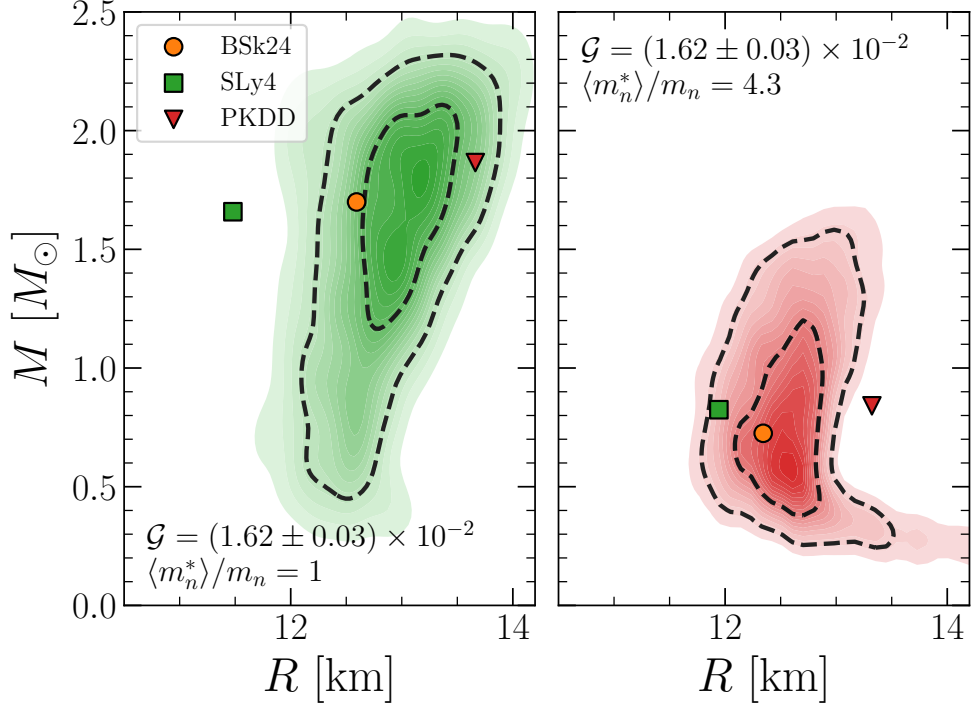
Figure 2.19: Marginalized posterior for the NS mass M and radius R of Vela, $\mathcal{G} = (1.62 \pm 0.03) \times 10^{-2}$, without ($\langle m_n^* \rangle / m_n = 1$ [LEL99], left panel) and with an estimation of crustal entrainment ($\langle m_n^* \rangle / m_n = 4.3$ [And+12], right panel), using the LD+HD filter for $p = 3$. Dashed lines represent the 50% and 90% confidence intervals, and symbols show the prediction of characteristic EoS models.

previous studies [PFH14; CGM19b], we observe large correlations between the crustal observables and the transition quantities, notably $r(P_t, I_{crust,1.4}/I_{1.4}) = 0.98$. Among the four popular models considered, only the prediction of the BSk24 EoS (orange circle) meets our distribution. The results for SLy4 (green square), PKDD (red triangle) and TM1 (purple triangle) EoS are only marginally compatible with the LD+HD prediction at the 90% confidence level (dashed lines).

From pulsar timing techniques, it is possible to infer the coupling parameter $\mathcal{G}$ of a given pulsar. This parameter is related to the fraction of crust moment of inertia via Eq. (2.14). In the specific case of the Vela pulsar (PSR B0833-45), the coupling parameter is very well constrained thanks to its long-term monitoring, $\mathcal{G}_{\text{Vela}} = (1.62 \pm 0.03) \times 10^{-2}$ [Ho+15]. Fig. 2.19 displays the marginalized posterior distributions for the mass and radius of Vela for two estimations of crustal entrainment, using our LD+HD distribution. Let us recall that the importance of the crustal entrainment effect is encoded in the neutron effective mass. Here, we consider $\langle m_n^* \rangle / m_n = 1$, that is no entrainment [LEL99], and $\langle m_n^* \rangle / m_n = 4.3$, which is an estimation of crustal entrainment [And+12]. In this calculation, we assume that the observed glitches correspond to

the maximum amplitude that can be sustained by the crust reservoir, which means that
we impose the equality

$$\frac{I_{crust}}{I} = \mathcal{G}_{\text{Vela}} \frac{\langle m_n^* \rangle}{m_n}. \tag{2.36}$$

Hence, the marginalized two-parameter distribution for Vela mass and radius is computed as

$$p(M, R | \text{data}) = \sum_{\boldsymbol{X}} \delta(M(\boldsymbol{X}) - M)\delta(R(\boldsymbol{X}) - R)p(\boldsymbol{X} | \text{data}), \tag{2.37}$$

where $M(\boldsymbol{X})$ and $R(\boldsymbol{X})$ are the mass and radius obtained with the parameter set $\boldsymbol{X}$ when
the central density is such that the corresponding fractional moment of inertia verifies
Eq. (2.36). The resulting distribution for Vela mass and radius without entrainment (left
panel) is compatible with the uncertainties reported in Table 2 of [Ho+15]. Evidently,
the uncertainties are larger in our work since we consider a distribution of models,
while three specific EoS (BSk20, BSk21, and APR) were used in [Ho+15]. In the same
spirit, we show the prediction of BSk24, SLy4, and PKDD EoS. Considering the specific
treatment of the entrainment effect with $\langle m_n^* \rangle / m_n = 4.3$ (right panel), the predicted Vela
mass is significantly lower than that inferred in the case where entrainment is neglected,
with $M_{\text{Vela}} = 0.79^{+0.41}_{-0.33} M_\odot$ at the 1σ confidence level. This shows that the uncertainty
on the importance of crustal entrainment is dominant over the EoS uncertainty and
the experimental uncertainty on the glitch amplitude. Let us notice that an innovative
method was recently proposed to determine the mass and radius using observations of
the maximum observed glitches [Piz+17].

Fig. 2.20 shows the average value of the fraction of crust moment of inertia I_{crust}/I
and the 50% and 90% regions as a function of the NS mass for the LD+HD posterior distribution. It should be stressed that the uncertainty on I_{crust}/I is smaller in [CGM19b]
because this quantity is correlated with the isovector empirical parameters K_{sym} and
Q_{sym}, which are strongly constrained by the filter on pressure, see Fig. 2.8, not accounted
for in the present calculation. The black lines represent the minimum values to justify
the large glitches exhibited by Vela with [Del+16; And+12] and without [LEL99] accounting for the entrainment effect. As expected from [LEL99], we find that the amount
of angular momentum stored in the crust is sufficient to explain pulsar glitches if the
entrainment effect is neglected. Given the intermediate estimation of crustal entrainment [And+12] ($\langle m_n^* \rangle / m_n = 4.3$), we infer that the mass of Vela must be lower than
$\approx 1.4 M_\odot$ to meet the LD+HD prediction at the 90% level. This can also be seen in
Fig. 2.18. Finally, it is clearly observed that the largest estimation of the crustal entrainment effect [Del+16] is incompatible with the present nuclear physics knowledge if
we keep the standard picture where a full crustal origin is assumed [AI75]. Indeed, it
yields $M_{\text{Vela}} \lesssim 1 M_\odot$, yet such low-mass NS have never been observed to this day.

2.4 Conclusion

In this chapter, we have first introduced the basic equations of hydrostatic equilibrium
in general relativity, for spherical nonrotating stars. We have solved these equations for
different popular EoS in order to obtain the relationship between the mass and radius
of the star. In the same spirit, we have computed the moment of inertia as well as the
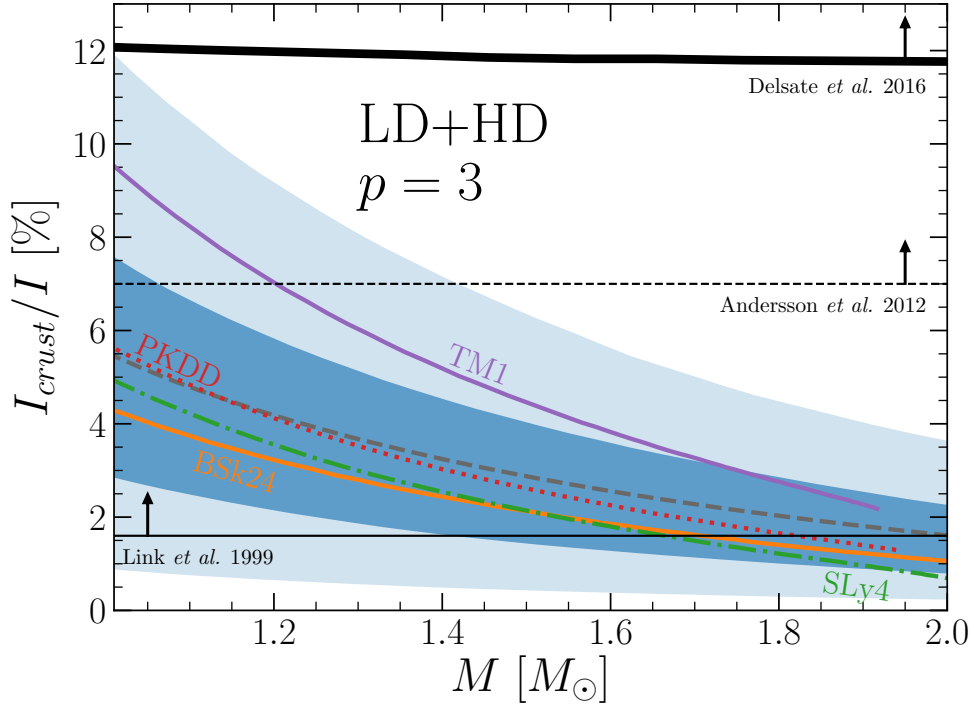
Figure 2.20: Marginalized posterior for the fraction of crust moment of inertia I_{crust}/I as a function of the NS mass M, using the LD+HD distribution. The blue dark and light shaded regions show the 50% and 90% confidence intervals, respectively. The gray dashed line represents the average value. The results for four characteristic EoS models are given. The minimum values needed to justify Vela glitches with (Delsate *et al.* [Del+16] and Andersson *et al.* [And+12]) and without (Link *et al.* [LEL99]) crustal entrainment are represented.

tidal deformability within the slow rotation approximation, which is expected to be valid for most of the pulsars. The determination of the CC transition density and pressure, discussed thoroughly in Chapter 1, allows the calculation of crustal observables. We have thus computed the crust thickness and fraction of crust moment of inertia. We have explained in detail the connection between the latter observable and the glitch phenomenon in the standard picture, that is where a glitch is observed during the transfer of angular momentum from the superfluid in the crust to the solid crust [AI75]. A major issue exhibited in Section 2.1 is the sensitivity of the results on the EoS, and more specifically on the isovector empirical parameters. We have shown that not every EoS successfully pass the maximum mass constraint of $M_{max} \gtrsim 2M_\odot$ [Dem+10; Ant+13; Cro+20]. In addition, the recent constraint on the tidal deformability parameter $\Lambda_{1.4}$ inferred from GW170817 [Abb+18] tends to favor soft EoS. Conversely, a full crustal origin for the glitch phenomenon can only be accepted with very stiff EoS, given the present estimations of crustal entrainment [And+12; PFH14].

We have recalled the principle of Bayesian inference before performing the Bayesian determination of the EoS parameters, using the metamodeling technique [MHG18a]. We have used a uniform prior distribution for the parameters, given empirical constraints. A sensitivity analysis on the CC transition point has revealed that the isovector parameters are likely to be the most important for the precise determination of n_t and P_t. We have calculated the likelihood function using constraints on nuclear physics observables (LD constraints), namely the experimental masses [Hua+17] and chiral EFT calculations on SNM and PNM [DHS16], and on NS observables as well as physical requirements (HD constraints). The posterior distribution of empirical parameters was analyzed. We have observed that the LD filter is very effective in constraining the isovector parameters, particularly if the impose the compatibility with the chiral ETF predicted bands for pressure. We have shown that only the constraints arising from nuclear physics impose correlations among the empirical parameters. In the isovector sector, the correlation between E_{sym} and L_{sym} is recovered, and we find that L_{sym} is correlated with K_{sym}. We have found new interesting correlations when imposing pressure filter: $r(L_{sym}, Q_{sym}) = -0.55$ and $r(K_{sym}, Q_{sym}) = 0.52$.

Finally, we have made general predictions for the static properties and crustal observables of NS, using the LD+HD joint posterior distribution of parameters calculated in Section 2.2. Overall, we have found that our predictions for the NS observables are in a rather good agreement with the constraints on the EoS, radius, and tidal deformability, inferred from the GW170817 event [De+18; Abb+18]. We have obtained $R_{1.4} = 12.88^{+0.53}_{-0.65}$ km and $\Lambda_{1.4} = 634^{+204}_{-190}$ at the 90% level. We have shown that the transition density and pressure are correlated with the isovector parameters, and particularly with the sqewness parameter Q_{sym}. Within the present experimental and theoretical uncertainty on those parameters, we have estimated the transition density and pressure respectively as $n_t = 0.068^{+0.021}_{-0.021}$ fm^{-3} and $P_t = 0.263^{+302}_{-0.149}$ MeV/fm^3, at the 1σ confidence level. In contrast with [CGM19a], we did not observe a strong influence of the surface parameters on the CC transition quantities. This can be explained by a refined control of the surface energy in the present work. We have observed that the thicker the crust is, the more angular momentum is confined to the neutron superfluid coexisting with the crystal lattice in the inner crust. The large uncertainty on the transition pressure is reflected on the fraction of crust moment of inertia. Indeed, for a $1.4M_\odot$ NS, we have obtained $I_{crust,1.4}/I_{1.4} = 2.89^{+2.51}_{-1.68}\%$, at the 1σ confidence level. The joint distribution for Vela mass and radius was computed for two different estimations of the crustal entrainment effect. It has shown that the uncertainty on crustal entrainment is largely dominant over those on the EoS and glitch amplitude. We have observed the variation with NS mass of the fraction of crust moment and inertia and concluded that a full crustal origin is excluded if we consider the present largest estimation of crustal entrainment [Del+16].

Chapter 3

Crystallization of the crust of a non-accreting neutron star

Contents

3.1 Model of the crust at finite temperature

This section deals with the model of the crust at finite temperature. Since the possible contribution of a free proton gas is expected to be small at the temperatures considered, we neglect it. This working hypothesis is a posteriori confirmed by the calculation of the proton fugacity, $z_p = \exp[(\mu_p - m_p c^2)/(k_B T)]$, which never exceeds -20 MeV in the density and temperature domain of interest. The existence of nonspherical pasta phases expected in the deeper layers of the inner crust ($n_B \gtrsim 0.05$ fm^{-3} [PCP20]) is difficult to account for in the multicomponent plasma (MCP) approach [BMG20], and as a consequence is not considered in this study.

We review the one-component plasma (OCP) approximation in 3.1.1. We give the expressions of the ideal and interacting contributions to the ion free energy in solid and liquid phases, and discuss the thermodynamic condition for crystallization. The nuclear statistical equilibrium (NSE) is implemented perturbatively in the MCP approach in 3.1.2. The derivation of the rearrangement term, required to guarantee thermodynamic consistency, is carried out. In 3.1.3, we present the free energy functional used in the free neutron regime.

3.1.1 One-component Coulomb plasma approximation

At zero temperature, WS cells are supposed to be identical, thus the OCP (single-nucleus) approximation [BH80], which considers a unique nucleus (A, Z) for a given thermodynamic condition of pressure and temperature (P, T), is exact. Let us recall that the equilibrium composition is determined by minimizing the Gibbs free energy per nucleon at fixed pressure [Fan+20] (or equivalently the free energy density at fixed baryon density [LS91; GR15; Car+20]). At finite temperature in the OCP approximation, the expected distribution of nuclei is replaced by the equilibrium nucleus obtained from the minimization of the relevant thermodynamic potential. The physical properties of the OCP are fully characterized by the so-called dimensionless Coulomb coupling parameter,

$$\Gamma = \frac{Ze^2}{a_N k_B T}, \tag{3.1}$$

where $a_N = (4\pi n_N/3)^{-1/3}$ is the ion-sphere radius, $n_N = 1/V_{WS}$ being the ion density. More precisely, Γ allows to quantify the nonideality of the system, that is the importance of the many-body interactions in the OCP. The lower the temperature, the more coupled are the ions. The crystallization of the OCP into a lattice is observed at $T = T_m$, corresponding to $\Gamma = \Gamma_m \approx 175$.

The total free energy per ion in the crust is given by

$$F = F_{i,e} + F_g + F_e, \tag{3.2}$$

where $F_{i,e}$ is the ion free energy in the e-cluster representation, see 1.2.1, F_g is the neutron gas free energy, and F_e is the electron gas free energy, given by [HPY07]

$$\mathcal{F}_e = \frac{F_e}{V_{WS}} = \varepsilon_e - \frac{P_r}{6} t_r^2 x_r \gamma_r, \tag{3.3}$$

with $t_r = T/(m_e c^2)$. The expressions of the energy density ε_e, relativistic unit of the electron pressure P_r, relativity parameter x_r, and γ_r are given in 1.1.1.2. It should be stressed that Eq. (3.3) is obtained by employing a Sommerfeld expansion in the limit $t_r \ll \gamma_r - 1$. Let us notice that in the regime of the outer crust, neutrons are still bound to the nuclei, thus $F_g = 0$ MeV, and consequently $F_{i,e}$ coincides with the ion free energy in the r-cluster representation F_i. The ion free energy reads

$$F_{i,e} = M_{i,e} c^2 + F_i^{\text{id}} + F_i^{\text{int}}, \tag{3.4}$$

where the ion mass in e-cluster representation $M_{i,e}$ has been introduced. In Eq. (3.4), F_i^{id} represents the ideal contribution to the ion free energy, that is the noninteracting part, and F_i^{int} the interacting part.

In the following, we give the expressions associated to the ideal and interacting contributions to the ion free energy which differ according to the phase of matter, either solid or liquid. In the free neutron regime, the finite-size contribution is included and is common to both phases. The latter is derived from the application of Gauss theorem,

$$E_{fs} = \frac{2n_p}{n_0(1-I)} \frac{e^2}{r_0} \frac{Z^2}{A^{1/3}}, \tag{3.5}$$

where $r_0 = (4\pi n_0/3)^{-1/3}$ is related to the average density of the cluster n_0. The modeling of $M_{i,e}$ as well as of the neutron gas free energy F_g is presented in detail in 3.1.3.

3.1.1.1 OCP in a liquid phase

Above the crystallization temperature, $T > T_m$, the OCP is in a liquid phase. In the Coulomb liquid, each ion can move freely within the volume of the WS cell in which it is confined. This translational center-of-mass motion is accounted for in the noninteracting part of the ion free energy, which therefore reads [HPY07]

$$F_i^{\text{id}} = k_B T \left[\ln \left(\frac{n_N \lambda^3}{g_s} \right) - 1 \right], \tag{3.6}$$

where g_s is the spin degeneracy, which we take $g_s = 1$ for nuclei whose ground-state angular momentum is unknown, and λ is the de Broglie wavelength of the component given by

$$\lambda = \sqrt{\frac{2\pi(\hbar c)^2}{M_{i,e} c^2 k_B T}}. \tag{3.7}$$

The interacting part of the ion free energy can be decomposed as [Fan+20]

$$F_i^{\text{int}} = F_{ii,\text{liq}} + F_{ie,\text{liq}}^{\text{pol}} \tag{3.8}$$

Analytical formulae have been derived for these two terms in [PC00]. In the present study, we find that the importance of the correction associated to electron polarization effects, $F_{ie,\text{liq}}^{\text{pol}}$ (Eq. (19) of [PC00]), is very small in the density and temperature regime of interest, and is therefore neglected. The only significant effect of the latter correction is to change the crystallization temperature of $40-50\%$ around $P \approx 1.25 \times 10^{-4}$ MeV/fm^3,

where the composition changes drastically due to shell structure [Fan+20]. For the total Coulomb contribution, we employ the parametrization proposed in [PC00]:

$$
\begin{aligned}
\frac{F_{ii,\text{liq}}}{k_B T} &= A_1 \left[\sqrt{\Gamma(A_2 + \Gamma)} - A_2 \ln \left(\sqrt{\Gamma/A_2} + \sqrt{1 + \frac{\Gamma}{A_2}} \right) \right] \\
&\quad + 2A_3 \left(\sqrt{\Gamma} - \arctan \sqrt{\Gamma} \right) + B_1 \left[\Gamma - B_2 \ln \left(1 + \frac{\Gamma}{B_1} \right) \right] \\
&\quad + \frac{B_3}{2} \ln \left(1 + \frac{\Gamma^2}{B_4} \right),
\end{aligned}
\tag{3.9}
$$

with $A_1 = -0.9070$, $A_2 = 0.62954$, $A_3 = -\sqrt{3}/2 - A_1/\sqrt{A_2}$, $B_1 = 4.56 \times 10^{-3}$, $B_2 = 211.6$, $B_3 = -10^{-4}$, and $B_4 = 4.62 \times 10^{-3}$. Let us notice that the latter parametrization solely depends on the Coulomb coupling parameter Γ, Eq. (3.1), and that $F_{ii,\text{liq}}$ vanishes at high temperature.

3.1.1.2 OCP in a solid phase

Once the crystallization temperature T_m is reached, we assume that the OCP crystallizes into a perfect body-centered cubic lattice [CF16], as in the zero temperature case studied in Chapter 1. In the solid OCP, ions are able to oscillate near their equilibrium positions. Hence, the ideal part of the ion free energy accounting for the translational motion in the liquid OCP, F_i^{id}, is replaced by the zero-point motion energy, E_{zp}, Eq. (1.3). The ion free energy in the e-cluster representation is therefore rewritten as

$$
F_{i,e,\text{sol}} = M_{i,e}c^2 + E_{zp} + F_{ii,\text{sol}} + F_{ie,\text{sol}}^{\text{pol}},
\tag{3.10}
$$

where $F_{ie,\text{sol}}^{\text{pol}}$ corresponds to the polarization correction in the solid phase [PC00], which is neglected here, and $F_{ii,\text{sol}}$ is the Coulomb interaction term that can be decomposed as

$$
F_{ii,\text{sol}} = E_L + F_{\text{th}} + F_{\text{ah}} - k_B T \ln(g_s).
\tag{3.11}
$$

In the latter expression, E_L represents the temperature-independent static lattice term, given by Eq. (1.5). The last term in 3.11 is the spin entropy. As previously, we fix $g_s = 1$ for nuclei whose spin degeneracy is unknown, yet the inclusion of this term has no effect on the determination of the crystallization temperature because it is the same for both liquid and solid OCP.

As for total Coulomb contribution in the liquid phase, the thermal contribution due to the ion vibrations around their equilibrium position in the harmonic approximation and the anharmonic correction have been analytically fitted by Baiko *et al.* [BPY01] and Potekhin & Chabrier [PC10], respectively. The expression employed for the thermal contribution reads [BPY01]

$$
\frac{F_{\text{th}}}{k_B T} = \sum_{n=1}^{3} \ln \left(1 - e^{-\alpha_n \theta} \right) - \frac{A(\theta)}{B(\theta)},
\tag{3.12}
$$

where $\theta \equiv \hbar \omega_p/(k_B T)$, ω_p being the ion plasma frequency, Eq. (1.4), and

$$
A(\theta) = \sum_{n=0}^{8} a_n \theta^n,
\tag{3.13}
$$

$$B(\theta) = \sum_{n=0}^{7} b_n \theta^n + \alpha_6 a_6 \theta^9 + \alpha_8 a_8 \theta^{11}, \tag{3.14}$$

with α_n, a_n, and b_n numerical constants (see Table II in [BPY01]). The analytical expression of the anharmonic correction used in our study is [PC10]

$$F_{\rm ah} = F_{\rm ah}^{(0)} {\rm e}^{-c_1 \theta^2} - k_B T d_1 \frac{\theta^2}{\Gamma}, \tag{3.15}$$

where

$$F_{\rm ah}^{(0)} = k_B T \sum_{n \geq 1} \frac{f_n}{n \Gamma^n} \tag{3.16}$$

with c_1, d_1, and f_n numerical constants. One should stress that the latter expression is modified with respect to that proposed by Farouki & Hamaguchi, $F_{\rm ah}^{(0)}$, based on numerical simulations of the solid OCP for $170 \leq \Gamma \leq 2000$ [FH93], so as to reproduce the zero-temperature and classical limits.

3.1.1.3   Crystallization of a OCP

As in previous works [Fan+20; Car+20; CFG20], we compute the crystallization temperature within the OCP approximation, which is simple and not costly from the numerical point of view. An additional reason is that the ion distribution could be frozen at some temperature $T_f > T_m$ considering the present uncertainties on timescales relative to NS cooling [Gor+11].

The condition of crystallization of a OCP with associated composition $\boldsymbol{\theta}$ is

$$\mathcal{F}_{\rm liq}(\boldsymbol{\theta}, T_m) = \mathcal{F}_{\rm sol}(\boldsymbol{\theta}, T_m), \tag{3.17}$$

where $\mathcal{F}_{\rm liq}$ and $\mathcal{F}_{\rm sol}$ are the WS cell free energy density in the liquid and solid phase, respectively. The latter equation is equivalent to

$$F_i^{\rm id} + F_{ii,{\rm liq}} = E_{zp} + F_{ii,{\rm sol}}, \tag{3.18}$$

which shows that the Coulomb coupling parameter at melting temperature Γ_m strongly depends on the corrections that step in a finite temperature. Furthermore, those corrections are small in the vicinity the crystallization temperature, making it difficult to estimate Γ_m with precision. Still, several works estimate the Coulomb parameter to $\Gamma_m \approx 175$ [Hor69; HPY07]. The crystallization temperature of a OCP at a given baryon density n_B can then be approximated by inverting Eq. (3.1), yielding

$$T_m \simeq \frac{(Ze)^2}{k_B a_N \Gamma_m} \ {\rm K}, \tag{3.19}$$

assuming the composition to be the same as in CCM. We proceed as in [Fan+20] in order to precisely calculate the crystallization temperature. At each value of the baryon density n_B and temperature T, the equilibrium composition is computed following the procedure detailed in Chapter 1. Specifically, we solve the coupled differential equations,
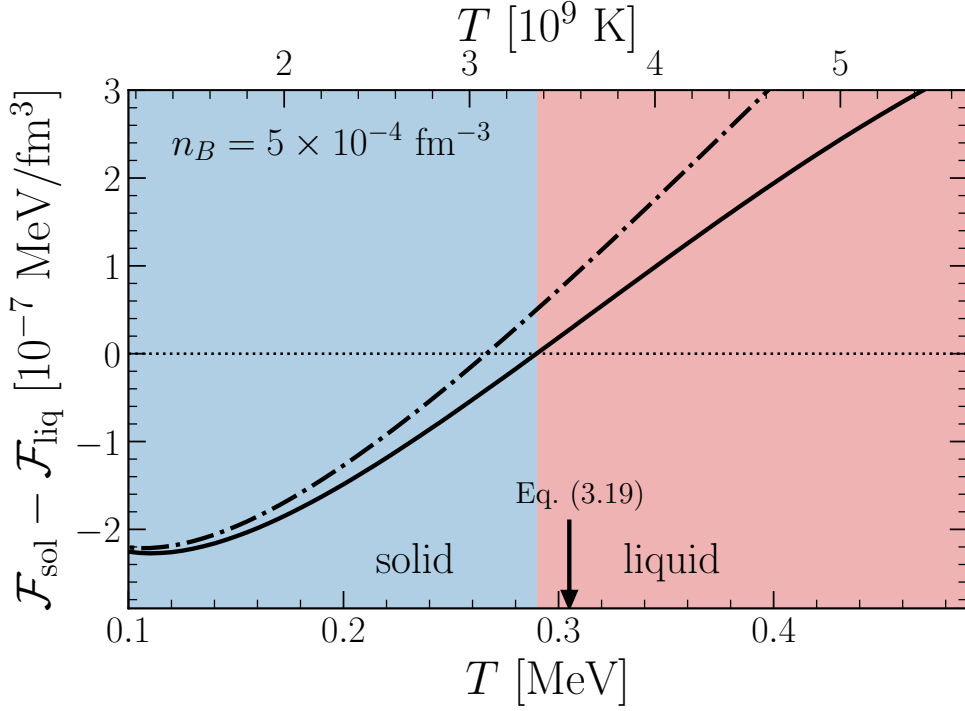
Figure 3.1: Variation with temperature T of the free energy density difference between liquid and solid phases $\mathcal{F}_{\mathrm{sol}} - \mathcal{F}_{\mathrm{liq}}$ for the optimal composition $\boldsymbol{\theta}_{\mathrm{liq}}$ at $n_B = 5 \times 10^{-4}$ fm^{-3} (free neutron regime) with (solid line) and without (dashdotted line) the anharmonic contribution, Eq. (3.15), to the free energy in the solid phase, using BSk24 CLDM. The crystallization temperature obtained from Eq. (3.19) is also indicated.

Eqs. (1.85)-(1.88), using the expressions of F_i^{id} and F_i^{ind} of the liquid phase, yielding the optimal liquid composition $\boldsymbol{\theta}_{\mathrm{liq}}$ and the associated WS cell free energy density $\mathcal{F}_{\mathrm{liq}}$. Then, for the same composition $\boldsymbol{\theta}_{\mathrm{liq}}$, we calculate the free energy density assuming a solid phase $\mathcal{F}_{\mathrm{sol}}(\boldsymbol{\theta}_{\mathrm{liq}})$. The lowest temperature for which $\mathcal{F}_{\mathrm{liq}} \geq \mathcal{F}_{\mathrm{sol}}$ is identified as the crystallization temperature T_m corresponding to the baryon density under study. The first guess for T_m is obtained from the application of Eq. (3.19).

Fig. 3.1 shows the variation with temperature of the free energy difference $\mathcal{F}_{\mathrm{sol}} - \mathcal{F}_{\mathrm{liq}}$ at a given baryon density $n_B = 5 \times 10^{-4}$ for the BSk24 CLDM based on the metamodeling technique. The intersect of the solid line and zero marks the crystallization temperature, $T_m = 0.29$ MeV, which is equivalent to $T_m = (1.16 \times 10^{10}) \times (0.29) = 3.36 \times 10^9$ K. We can observe that the crystallization temperature is significantly lower if the anharmonic contribution to the free energy of the solid OCP is neglected (dashdotted line). This stresses the importance of the small thermal corrections in the calculation. It is also seen that the effect of the anharmonic contribution becomes bigger with temperature increasing, and vanishes in case of strong coupling, that is in the zero-temperature limit. We find that the simple expression Eq. (3.19) gives a fairly good estimation of the

crystallization temperature.

3.1.2   Multicomponent Coulomb plasma in a liquid phase

The OCP approximation is expected to be reliable at the temperatures typically encountered at low density in the crystallized crust, yet the very principle of statistical mechanics tells us that at finite temperature different configurations of the WS cell are realized for a same total density. In the following, the nuclear distribution is included in a MCP approach at equilibrium, as in [Fan+20; CFG20]. A particular attention is paid to the evaluation of the chemical potentials, as well as of the rearrangement term, which is required to ensure thermodynamic consistency.

3.1.2.1   Nuclear statistical equilibrium

The NS crust at a given depth in the star is supposed to contain different ion species characterized by their mass and charge number $(A^{(j)}, Z^{(j)})$, associated to different WS cells of volume $V_{WS}^{(j)}$, such that p_j is the frequency of occurence (or probability) of the component (j), with $\sum_j p_j = 1$. Thermodynamic quantities are defined in terms of the ion densities of the different species $n_N^{(j)}$, which are related to the probabilities p_j through

$$n_N^{(j)} = \frac{p_j}{\langle V_{WS} \rangle}. \tag{3.20}$$

where the average WS cell volume has been introduced,

$$\langle V_{WS} \rangle = \sum_j p_j V_{WS}^{(j)}, \tag{3.21}$$

the notation $\langle \rangle$ indicating ensemble averages. The different configurations $(A^{(j)}, Z^{(j)})$ are associated with different different baryon densities $n_B^{(j)}$, such that the total baryon density is

$$n_B = \sum_j p_j n_B^{(j)}. \tag{3.22}$$

Conversely, they share the same total pressure P imposed by the hydrostatic equilibrium and the same background densities of electrons, $n_e^{(j)} = n_e$, and of free neutrons, $n_g^{(j)} = n_g$. It is assumed that the charge neutrality is assured at the level of each cell, implying that the proton density is the same in each cell, $n_p^{(j)} = n_p$, and equal to the electron density,

$$n_e = n_p = \sum_j n_N^{(j)} Z^{(j)} = \frac{Z^{(j)}}{V^{(j)}}. \tag{3.23}$$

The free energy density of the MCP is given by

$$\mathcal{F} = \sum_j n_N^{(j)} F^{(j)}, \tag{3.24}$$

where $F^{(j)}$ is the free energy per ion of a single component (j) defined in Eq. (3.2). The probabilities p_j and ion densities $n_N^{(j)}$ are calculated such as to maximize the thermodynamic potential in the canonical ensemble. Because of the chosen free energy

decomposition, we can observe that the free neutron and electron contributions to the free energy density, respectively $\mathcal{F}_g$ and $\mathcal{F}_e$, do not depend on $n_N^{(j)}$,

$$\mathcal{F}\left(\left\{n_N^{(j)}\right\}\right) = \mathcal{F}_{i,e}\left(\left\{n_N^{(j)}\right\}\right) + \mathcal{F}_g + \mathcal{F}_e, \tag{3.25}$$

with

$$\mathcal{F}_{i,e} = \sum_j n_N^{(j)} F_{i,e}^{(j)}. \tag{3.26}$$

This means that the variation can be performed on the ion part only, yielding

$$
\begin{aligned}
d\mathcal{F}_{i,e} &= \sum_j \left(F_{i,e}^{(j)} + n_N^{(j)} \frac{\partial F_{i,e}^{(j)}}{\partial n_N^{(j)}} \right) dn_N^{(j)} \\
&= \sum_j \left(F_{i,e}^{(j)} + k_B T + n_N^{(j)} \frac{\partial F_i^{(j),\text{int}}}{\partial n_N^{(j)}} \right) dn_N^{(j)} \\
&= \sum_j \left(\Omega_{i,e}^{(j)} + k_B T \ln n_N^{(j)} \right) dn_N^{(j)},
\end{aligned}
\tag{3.27}
$$

where the single-ion canonical potential has been introduced,

$$\Omega_{i,e}^{(j)} = M_{i,e} c^2 + k_B T \ln \frac{(\lambda^{(j)})}{g_s^{(j)}} + F_i^{(j),\text{int}} + n_N^{(j)} \frac{\partial F_i^{(j),\text{int}}}{\partial n_N^{(j)}}. \tag{3.28}$$

A deviation to the linear-mixing rule (the hypothesis of uncorrelated WS cells) is observed in Eq. (3.28) due to the translational degree of freedom in the liquid phase [GR15], because within the MCP approach the center-of-mass position of each ion is not confined to the single cell volume $V_{WS}^{(j)}$ but can freely explore the whole volume. As a consequence, the average composition of the MCP does not coincide with the OCP optimal configuration in general.

In Eq. (3.27), the variations $dn_N^{(j)}$ are not independent because of the normalization of probabilities, and the baryon number and charge conservation laws:

$$\frac{1}{\langle V \rangle} = \sum_j n_N^{(j)}, \tag{3.29}$$

$$n_B - n_g = \sum_j n_N^{(j)} A^{(j)} \left(1 - \frac{n_g}{n_0^{(j)}} \right), \tag{3.30}$$

$$n_p = \sum_j n_N^{(j)} Z^{(j)}. \tag{3.31}$$

We can identify the mass number associated to component (j) in e-cluster representation $A_e^{(j)}$ in the right hand side of Eq. (3.30). Let us recall that in the regime of the outer crust, $n_g = 0$ fm^{-3} thus $A_e^{(j)} = A^{(j)}$. The average density of the ion (j) $n_0^{(j)}$ is obtained by solving numerically the equation corresponding to the pressure equilibrium between the ion and the gas (see 1.2.2 for the derivation),

$$\frac{n_0^{(j)}}{A^{(j)}} \frac{\partial F_i^{(j)}}{\partial n_0^{(j)}} = P_g, \tag{3.32}$$

P_g being the pressure of the neutron gas, whose expression is given in Eq. (1.54). As in [Gra+18], the neutron gas density is taken to be the OCP solution, $n_g = n_g^{\mathrm{OCP}}$. The constraints Eqs. (3.29)-(3.31) are taken into account by introducing the Lagrange multipliers α, μ_n, and μ_p, leading to the following equations for the equilibrium densities $n_N^{(j)}$:

$$\sum_j \left(\Omega_{i,e}^{(j)} + k_B T \ln n_N^{(j)} - \alpha \right) dn_N^{(j)} - \mu_n \sum_j N_e^{(j)} dn_N^{(j)} - \mu_p \sum_j Z^{(j)} dn_N^{(j)} = 0 \qquad (3.33)$$

with $N_e^{(j)} = A_e^{(j)} - Z^{(j)}$. Considering independent variations, the solutions are given by

$$p_j = \mathcal{A} \exp\left(-\frac{\tilde{\Omega}_{i,e}^{(j)}}{k_B T} \right), \qquad (3.34)$$

with the normalization constant

$$\mathcal{A} = \exp\left(\frac{\alpha}{k_B T} \right) = \sum_j \exp\left(-\frac{\tilde{\Omega}_{i,e}^{(j)}}{k_B T} \right). \qquad (3.35)$$

The single-ion grand-canonical potential reads

$$\tilde{\Omega}_{i,e}^{(j)} = \Omega_{i,e}^{(j)} - \mu_n N_e^{(j)} - \mu_p Z^{(j)}, \qquad (3.36)$$

where μ_n and μ_p correspond finally to the neutron and proton chemical potentials, respectively. Let us note that the rest-mass energies are included in the the chemical potentials since they are contained in the ion free energy. The calculation of the grand-canonical potential $\tilde{\Omega}_{i,e}^{(j)}$, entering the definition of the probabilities p_j, requires the evaluation of the chemical potentials μ_n and μ_p, as well as of the rearrangement term

$$\mathcal{R}^{(j)} = n_N^{(j)} \frac{\partial F_i^{(j),\mathrm{int}}}{\partial n_N^{(j)}}, \qquad (3.37)$$

which are discussed thoroughly in 3.1.2.2 and 3.1.2.3, respectively.

3.1.2.2   Evaluation of the chemical potentials

For a given thermodynamic condition of pressure P and temperature T, the expression of the chemical potentials μ_n and μ_p can be derived from the well-known thermodynamic relation $\mathcal{F} + P = \mu_n n_n + \mu_p n_p + \mu_e n_e$ together with the beta equilibrium condition $\mu_n = \mu_p + \mu_e$,

$$\mu_n = \frac{\mathcal{F} + P}{n_B} \quad \text{and} \quad \mu_p = \mu_n - \frac{\mathcal{F}_e + P_e}{n_p}, \qquad (3.38)$$

where the electron chemical potential and pressure, respectively μ_e and P_e have been introduced. The determination of the equilibrium probabilities p_j within the complete NSE formalism therefore requires to solve a complex nonlinear system of coupled equations, which is obviously numerically costly. Still, the implementation of the complete

NSE was carried out in different studies in recent years [Oer+17; FF18], in which simplified nuclear functionals were adopted, density was imposed instead of the pressure, and the rearrangement term was neglected.

We choose here to implement the NSE perturbatively, as proposed in [Gra+18]. The motivation for this option comes from the recent work of Fantina *et al.*, where a very fast convergence of the chemical potentials is observed, along with a reduction of the computational time and an increase of the numerical precision [Fan+20]. We start by solving the OCP variational equations in order to get the equilibrium composition, which gives a first guess for the chemical potentials, μ_n^{OCP} and μ_p^{OCP}, via Eq. (3.38). The probabilities p_j can then be evaluated using Eq. (3.34), and an improved estimation of the chemical potentials μ_n and μ_p is calculated via

$$\mu_n = \frac{\sum_j n_N^{(j)} F^{(j)}}{\sum_j n_N^{(j)} A_e^{(j)} + n_g} + \frac{P}{n_B} \quad \text{and} \quad y_p \mu_e = \frac{\sum_j n_N^{(j)} F_e^{(j)}}{\sum_j n_N^{(j)} A_e^{(j)} + n_g} + \frac{P_e}{n_B}, \qquad (3.39)$$

where the average proton fraction of the mixture $y_p = \langle Z \rangle / (n_B \langle V_{WS} \rangle)$ has been introduced, with $\langle Z \rangle = \sum_j p_j Z^{(j)}$. The problem is thus solved by iteration until the convergence of the chemical potentials is observed. The convergence criterion is reasonably set to be $\Delta \mu_n < 10^{-9}$ MeV between iterations. We find that the number of iterations required to achieve convergence never exceeds 3. The reason is that the OCP result for μ_n and μ_p is already very close to the actual solutions for all pressures and temperatures explored in this work. Therefore, while we do solve the self-consistent problem in the regime of the outer crust to calculate the chemical potentials, the OCP estimation is safely kept in the free neutron regime so as to drastically reduce the computational cost. Indeed, in doing so the MCP calculation becomes equivalent to the much simpler OCP one.

3.1.2.3 Evaluation of the rearrangement term

At a given thermodynamic condition (P, T), the rearrangement term entering Eq. (3.28) requires to be evaluated if one wants to compute the ion abundances through Eq. (3.34). As already discussed in [Fan+20], the rearrangement term arises from the self-consistency induced by the Coulomb part of the ion free energy. This stems from the fact that, due to the strong incompressibility of the electrons, the condition of charge neutraly has been imposed at the level of each cell, see Eq. (3.23), in contrast with the baryon density n_B that can fluctuate from cell to cell, see Eq. (3.30). In consequence, any component of the free energy density that depends on the local cell proton density $n_p^{(j)} = n_p$ leads to a dependence on the local density $n_N^{(j)}$ through Eq. (3.23). With our presciption for the WS cell free energy, this is only the case for the interacting part $F_i^{(j),\mathrm{int}}$. We can therefore rewrite the rearrangement term of component (j) as

$$\begin{aligned} \mathcal{R}^{(j)} &= \left. n_N^{(j)} \frac{\partial F_i^{(j),\mathrm{int}}}{\partial n_N^{(j)}} \right|_{\{n_N^{(j)}\}_{i \neq j}} = n_N^{(j)} \frac{\partial F_i^{(j),\mathrm{int}}}{\partial n_p} \frac{\partial n_p}{\partial n_N^{(j)}} \\ &= n_N^{(j)} Z^{(j)} \frac{\partial F_i^{(j),\mathrm{int}}}{\partial n_p}. \end{aligned} \qquad (3.40)$$

The complication of the self-consistent resolution of Eq. (3.34) can be avoided by imposing the most probable ion in the MCP mixture to coincide with the OCP result, if nonlinear mixing terms are omitted [Gra+18]. This approximation for the rearragement term is justified by the principle of ensemble equivalence in the thermodynamic limit [GR15].

The maximum probability corresponds to the minimum of the single-ion grand-canonical potential $\tilde{\Omega}_{i,e}$. We therefore minimize the single-ion grand-canonical potential with respect to A, $I = 1 - 2Z/A$, and n_0 (n_p and n_g are fixed at a given thermodynamic condition), yielding the following nonlinear system of coupled equations:

$$\frac{n_0^2}{A}\left(\frac{\partial F_i}{\partial n_0} + \frac{\partial \mathcal{R}}{\partial n_0}\right) = P_g \tag{3.41}$$

$$\frac{2}{A}\left(\frac{\partial F_i}{\partial I} + \frac{\partial \mathcal{R}}{\partial I}\right) = \mu_n - \mu_p \tag{3.42}$$

$$\frac{\partial F_i}{\partial A} + \frac{\partial \mathcal{R}}{\partial A} + \frac{1-I}{A}\left(\frac{\partial F_i}{\partial I} + \frac{\partial \mathcal{R}}{\partial I}\right) = \mu_n - \frac{P_g}{n_0}, \tag{3.43}$$

where the partial derivatives are calculated at the values corresponding to the equilibrium OCP solution, with nonlinear mixing terms being excluded. The comparison of Eqs. (3.41)-(3.43) with Eqs. (1.86)-(1.88) indicates that $\mathcal{R}^{(j)}$ should not depend on $n_0^{(j)}$, meaning that $R^{(j)} = R^{(j)}(A^{(j)}, Z^{(j)})$. In addition, the rearrangement term should verify the following equation at the OCP solution:

$$\frac{1-I}{A}\frac{\partial \mathcal{R}}{\partial I} = -\frac{\partial \mathcal{R}}{\partial A}, \tag{3.44}$$

which is satisfied if $R^{(j)}$ linearly depends on $Z^{(j)} = A^{(j)}(1-I^{(j)})/2$. Our final expression for the rearrangement term is therefore

$$\mathcal{R}^{(j)} \simeq Z^{(j)}\left\langle \langle n_N^{(j)}\rangle \frac{\partial F_i^{(j),\mathrm{int}}}{\partial n_p}\right\rangle_j = \frac{Z^{(j)}}{V_{WS}^{\mathrm{OCP}}}\left.\frac{\partial F_i^{\mathrm{int}}}{\partial n_p}\right|_{\mathrm{OCP}}, \tag{3.45}$$

where V_{WS}^{OCP} is the equilibrium OCP cell volume, and the derivative is evaluated numerically at the OCP solution.

3.1.3   Free energy functional in the free neutron regime

As previously discussed in Chapter 1, in the regime of the outer crust we use the present day knowledge on experimental masses of neutron rich nuclei [Hua+17; Wel+17], combined with state-of-the-art microscopic HFB theoretical mass tables [GCP13]. The ion mass $M_{i,e}$ in the outer crust is therefore simply calculated using Eq. (1.6).

In the regime of the inner crust, $n_B \gtrsim 2.6 \times 10^{-4}$ fm^{-3}, we have seen that the ions are immersed in a neutron gas, whose free energy density $\mathcal{F}_g$ enters the expression of the ion mass in the e-cluter representation,

$$M_{i,e}^{(j)}c^2 = (A^{(j)} - Z^{(j)})m_n c^2 + Z^{(j)}m_p c^2 + F_{cl}^{(j)} - \frac{A^{(j)}}{n_0^{(j)}}(\mathcal{F}_g + n_g m_n c^2), \tag{3.46}$$

where $F_{cl}^{(j)}$ represents the nuclear free energy. In the range of densities corresponding to the free neutron regime, the clusters are so neutron rich that experimental data are not available. As a consequence, the modeling of $F_{cl}^{(j)}$ is required.

In the following, we first recall the simple case of free Fermi gas before deriving the expressions required to describe to the ambient neutron gas at finite temperature. We then give the expressions of the different quantities entering the expression of the smooth part of the nuclear free energy functional $F_{cl}^{(j)}$. The temperature dependence of shell corrections and its effect on the crystallization temperature is investigated in 3.3.1.

3.1.3.1 Thermodynamics of nuclear matter

Let us first consider a collection of noninteracting fermions. In the grand-canonical ensemble, it obeys Fermi-Dirac statistics and the average number of fermions occupying a single-particle state i is given by the Fermi-Dirac distribution,

$$\langle n_i \rangle = \left[1 + \exp\left(\frac{e_i - \mu}{k_B T} \right) \right]^{-1}, \tag{3.47}$$

where e_i is the energy of the single-particle state i, and μ is the total chemical potential. At the thermodynamic limit, the sum over states i is replaced by an integral over the energy, thus the Fermi-Dirac function that describe the occupation rate of state of given energy e is introduced,

$$f_{\mathrm{FD}}(e, T, \mu) = \left[1 + \exp\left(\frac{e - \mu}{k_B T} \right) \right]^{-1}. \tag{3.48}$$

When replacing the sum by an integral, one need to introduce the density of energy states $\rho(e)$. For a spinless free particle of energy $e = \hbar^2 k^2/(2m)$, the density of states is given by $\rho(\vec{k}) = \frac{V}{(2\pi)^3}$, with k the wave vector and V the volume. Using the relation $\rho(\vec{k}) d^3 k = \rho(e) de$, one obtains

$$\rho(e) = g \frac{V}{4\pi^2} \left(\frac{2m}{\hbar^2} \right)^{3/2} \sqrt{e}, \tag{3.49}$$

where the spin degeneracy $g = 2s + 1$ (for fermions, $s = 1/2$) has been introduced, and mass m is the mass of a particle. At the thermodynamic limit, that is if we consider a huge number of particles at a given temperature T so that a large number of states are occupied, all ensembles are equivalent. This means that we can use the expressions of the grand-canonical ensemble to calculate for instance the exact number of particles and the energy, respectively

$$N = \sum_i \langle n_i \rangle \simeq \int_0^\infty \rho(e) f_{\mathrm{FD}}(e) de \quad \text{and} \quad E \simeq \int_0^\infty e \rho(e) f_{\mathrm{FD}}(e) de. \tag{3.50}$$

At zero temperature, states are populated up to the Fermi energy $\mu(T = 0) = e_F$. Indeed, $f_{\mathrm{FD}} = 1$ for $e < \mu$, otherwise $f_{\mathrm{FD}} = 0$, which allows us to rewrite Eq. (3.50) as

$$N(T = 0) = \int_0^{e_F} de \rho(e), \tag{3.51}$$

yielding the expression of the Fermi energy,

$$e_F = \frac{\hbar^2}{2m}\left(3\pi^2\frac{N(T=0)}{V}\right)^{2/3} = \frac{\hbar^2 k_F^2}{2m}, \tag{3.52}$$

with $k_F = (3\pi^2 N(T=0)/V)^{1/3}$ the Fermi wave vector. At $T = 0$ K, the free energy is simply equivalent to the energy:

$$F(T=0) = E(T=0) = \int_0^{e_F} e\rho(e)de = \frac{3}{5}Ne_F. \tag{3.53}$$

At nonzero temperature, the calculation of thermodynamic properties of a free Fermi gas generally requires the numerical evaluation of Fermi integrals,

$$F_\nu(u) = \frac{1}{\Gamma(\nu+1)}\int_0^\infty \frac{t^\nu}{1+\exp(t-u)}dt, \tag{3.54}$$

where $\Gamma(\nu) = (\nu-1)!$ is the gamma function. It is however useful to apply Sommerfeld development in the limit $T \ll e_F$ – which is satisfied in the range of temperatures explored in our work – in order to derive analytical formulas. In that case, we can obtain the expression of the chemical potential from $N = \int_0^\infty \rho(e)f_{\rm FD}(e)de$, assuming that $\mu = e_F(1 + \alpha T^2)$. By identifying terms scaling as T^2, we get

$$\mu = e_F\left[1 - \frac{\pi^2}{12}\left(\frac{T}{e_F}\right)^2\right]. \tag{3.55}$$

We can proceed in the same manner to calculate the energy at finite temperature and the entropy, respectively

$$E = \frac{3}{5}Ne_F\left[1 + \frac{5\pi^2}{12}\left(\frac{T}{e_F}\right)^2\right] \quad \text{and} \quad S = \frac{\pi^2}{2}N\frac{T}{e_F}, \tag{3.56}$$

which finally gives, using the thermodynamic relation $F = E - TS$, the expression of the free energy of a nonrelativistic free Fermi gas,

$$F = \frac{3}{5}Ne_F\left[1 - \frac{5\pi^2}{12}\left(\frac{T}{e_F}\right)^2\right]. \tag{3.57}$$

We now turn to show that those results can still be used in the case of a huge number of interacting fermions in a infinite volume at a finite density, that is for infinite nuclear matter. The energy density $\mathcal{H} = \mathcal{K} + \mathcal{V}$ for this idealized system can be derived from an effective functional, and is often decomposed into a kinetic term and a contribution due to the nuclear interactions, respectively $\mathcal{K}$ and $\mathcal{V}$. As discussed in 1.2.1.1, the effective mass m_q^* of species q is usually introduced to regroup in a single term of kinetic energy the momentum dependence of the mean field,

$$\frac{\hbar^2 k_q^2}{2m_q^*} = \frac{\hbar^2 k_q^2}{2m_q} + U_{\rm eff}(k_q). \tag{3.58}$$

In the grand-canonical ensemble, the occupation rate of state of given energy e_q for interacting fermions reads

$$f_q(e_q + U_q, T, \mu_q) = \left[1 + \exp\left(\frac{e_q + U_q - \mu_q}{k_B T}\right)\right]^{-1}, \tag{3.59}$$

where $e_q + U_q = \hbar^2 k_q^2/(2m_q^*) + U_q$ is the single-particle energy of species q, $U_q = \partial \mathcal{H}/\partial n_q$ being the local mean field potential, which is given in the metamodel by $(q = n, p)$

$$\begin{aligned}
U_q &= v_{MM}(n, \delta) + \frac{1 + 3x}{3}\left(\frac{\partial v_{MM}}{\partial x}\right)_\delta + (\tau_3 - \delta)\left(\frac{\partial v_{MM}}{\partial \delta}\right)_x \\
&+ (1 + 3x) \sum_{l=n,p} \frac{3}{5} \frac{1 + \tau_{3,l}\delta}{2} e_{F,l}\left[1 - \frac{5\pi^2}{12}\left(\frac{T}{e_{F,l}}\right)^2\right] \\
&\times \frac{m_l^*}{m}\left[\kappa_{sat} + \tau_{3,l}\kappa_{sym}\left(\delta + \frac{\tau_3 - \delta}{1 + 3x}\right)\right], \tag{3.60}
\end{aligned}$$

with $\tau_{3,l} = 1$ $(\tau_{3,l} = 1)$ for $l = n$ $(l = p)$. The expressions of the potential energy v_{MM} and effective masses are given in 1.2.1.1. The simple case of free Fermi gas is recovered by introducing the effective chemical potential $\tilde{\mu}_q = \mu_q - U_q$, yielding the free energy per particle of nuclear matter,

$$f_{HM}(n, \delta, T) = \sum_{q=n,p} \frac{3}{5} \frac{1 + \tau_3\delta}{2} e_{F,q}\left[1 - \frac{5\pi^2}{12}\left(\frac{T}{e_{F,q}}\right)^2\right] + v_{MM}(n, \delta).. \tag{3.61}$$

which enters the expression of the neutron gas free energy, $\mathcal{F}_g = n_g f_{HM}(n_g, 1, T)$. Let us note that the chemical potential does not include the rest mass energy in the above expressions.

3.1.3.2 Energetics of clusters at finite temperature in the CLD approximation

Within the CLD approximation, the nuclear free energy F_{cl} at temperature T of a cluster of mass number A, isospin asymmetry I, and average density n_0, can be decomposed into a bulk, surface and Coulomb part as

$$F_{cl}^{CLD} = A f_{HM}(n_0, I, T) + F_{surf} + F_{curv} + F_{Coul}, \tag{3.62}$$

where $f_{HM}(n_0, I, T)$ represents the free energy per baryon of bulk nuclear matter, which is calculated using Eq. (3.61). The expressions used for the surface and curvature free energy are given in Eqs. (1.58) and (1.60) respectively, with the exception of the surface tension, Eq. (1.59) whose expression is modified with respect to the zero temperature case in order to effectively account for the excitation of surface modes:

$$\sigma(I, T) = \sigma(I, T = 0)h(T), \tag{3.63}$$

with $h(T > T_c) = 0$ and $h(T \le T_c) = [1 - (T/T_c)^2]^2$ (see Eq. (2.31) of [LS91]). However, because the critical temperature T_c is of the order of $T_c \approx 1.75 \times 10^{11}$ K and the

crystallization temperature is lower than 10^{10} K in the inner crust [HPY07], $h \approx 1$ and the excitation of surface modes can be neglected. Assuming spherical clusters, we write the Coulomb energy as

$$F_{Coul} = \frac{3}{5} \frac{e^2}{r_0^2} \frac{Z^2}{A^{1/3}}.$$ (3.64)

We limit ourselves to the empirical parameters associated to four different functionals of the BSk family taken from [GCP13]: BSk22, BSk24, BSk25, and BSk26. We choose these models because they all provide excellent fits to the AME2016 [Hua+17], are compatible both with ab initio and NS mass constraints, and explore a relatively large domain in the symmetry energy parameters (consistent with existing experimental constraints), which constitute the most important part of the EoS uncertainty [Pea+14; Pea+18]. Moreover, for each functional, surface and curvature parameters can be fitted to the ETF results [Pea+19], and the corresponding Strutinsky shell corrections, which are tabulated in [Pea+18], can be added on top of the CLD free energy, see 1.2.4 and 3.3.1. Another motivation is that full mass tables obtained by deformed HFB calculations have been published for these models [Xu +13] and can therefore be used in the regime of the outer crust as a complement to experimental masses [Fan+20].

3.2   Study of the outer crust at crystallization

In this section, we present the results for the outer crust at finite temperature, and more at crystallization. Unless explicitly stated, all thermal corrections introduced in Section 3.1 are included in the ion free energy. We made use of experimental masses from AME2016 [Hua+17] when available, apart from the mass excesses of $^{77-79}$Cu which are better constrained in [Wel+17].

The crystallization temperature of a OCP is calculated throughout the outer crust in 3.2.1. In 3.2.2, the equilibrium composition of the MCP at crystallization is presented, and deviations with respect to CCM are investigated. The variation with pressure of the impurity parameter is analyzed in 3.2.3. Finally, the fraction of odd nuclei present in the outer crust at crystallization is computed in 3.2.4.

3.2.1   Crystallization temperature

The left panel of Fig. 3.2 shows the crystallization temperature as a function of the pressure in the outer crust, as obtained in the OCP approximation, Eq. (3.17). Experimental masses are supplemented with the microscopic HFB-24 theoretical mass table [GCP13]. It is seen that the crystallization temperature is overall an increasing function of the pressure in the outer crust, and ranges from approximately 5×10^7 K (4 keV) at very low pressure to 2.8×10^9 K (240 keV) close to the neutron-drip point. As one could have expected from the quadratic dependence on Z observed in Eq. (3.19), we can see that the effect of shell structure on the crystallization temperature is very important. Indeed, each change in the equilibrium OCP composition results in an abrupt change in T_m, that is clearly noticeable in Fig. 3.2. In particular, the fact that the curve of the crystallization temperature is very steep in the vicinity of $P = 1.2 \times 10^{-4}$ MeV/fm^3, with T_m rapidly increasing from 1.2×10^9 K to 2.4×10^9 K, can be easily attributed
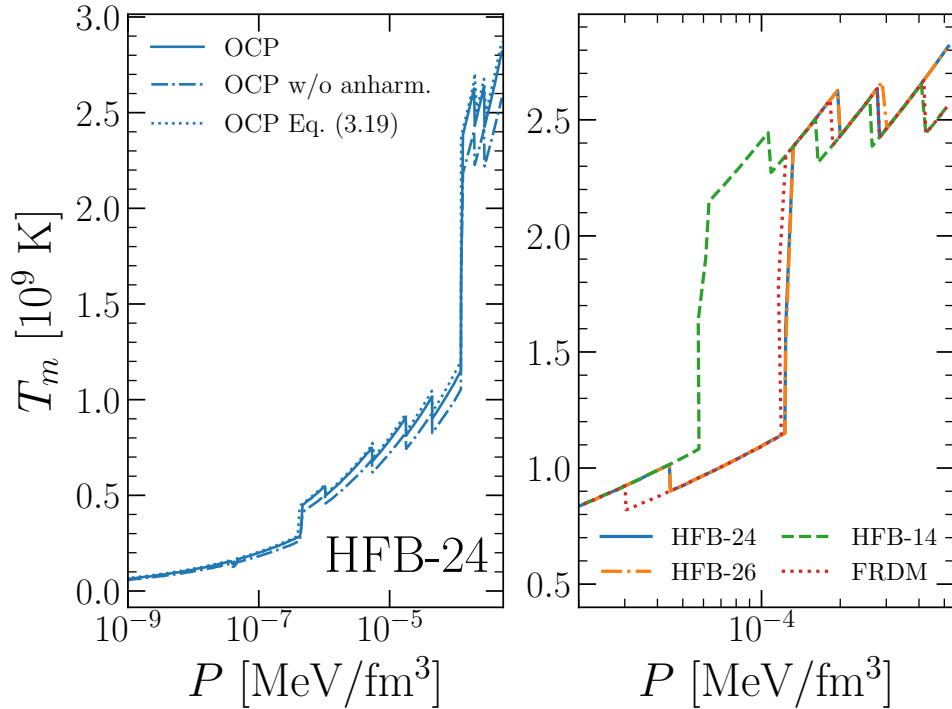
Figure 3.2: Crystallization temperature T_m as a function of pressure P for the OCP in the outer crust. The left panel shows T_m for the OCP with all corrections included (solid line), without taking into account the anharmonic contribution (dashdotted line), and the result obtained from Eq. (3.19) (dotted line). Experimental data are supplemented with masses from microscopic HFB-24 theoretical mass table [GCP13]. The right panel shows T_m in the bottom layers of the outer crust for four selected models: HFB-24 (solid blue line), HFB-26 [GCP13] (dashdotted orange line), HFB-14 [GSP07] (dashed green line), and FRDM [Mol+95] (dotted red line).

to the transition from $N = 50$ to $N = 82$, observed in Fig. 1.1. The importance of the anharmonic contribution to the ion free energy of a solid OCP, already investigated in Fig. 3.1, can be appreciated in the left panel of Fig. 3.2 by comparing the solid and dashdotted blue lines. We recover the result of [Fan+20] that the crystallization temperature is quite sensitive to the anharmonic contribution. We find that not accounting for this thermal correction induce an error on T_m of the order of 10% in the range of pressure corresponding to the outer crust. The dotted blue line shows the result of the approximation Eq. (3.19). It is seen that one can obtain a very good estimation of the crystallization temperature for all pressures in the outer crust by using this approximation, which indicates that the crystallized composition (at $T = T_m$) is very similar to that at $T = 0$ K. This is discussed in detail in 3.2.2. The fact that Eq. (3.19) consistently but only slightly overestimate the crystallization temperature justify its use for getting a first estimate so as to reduce the computational time.
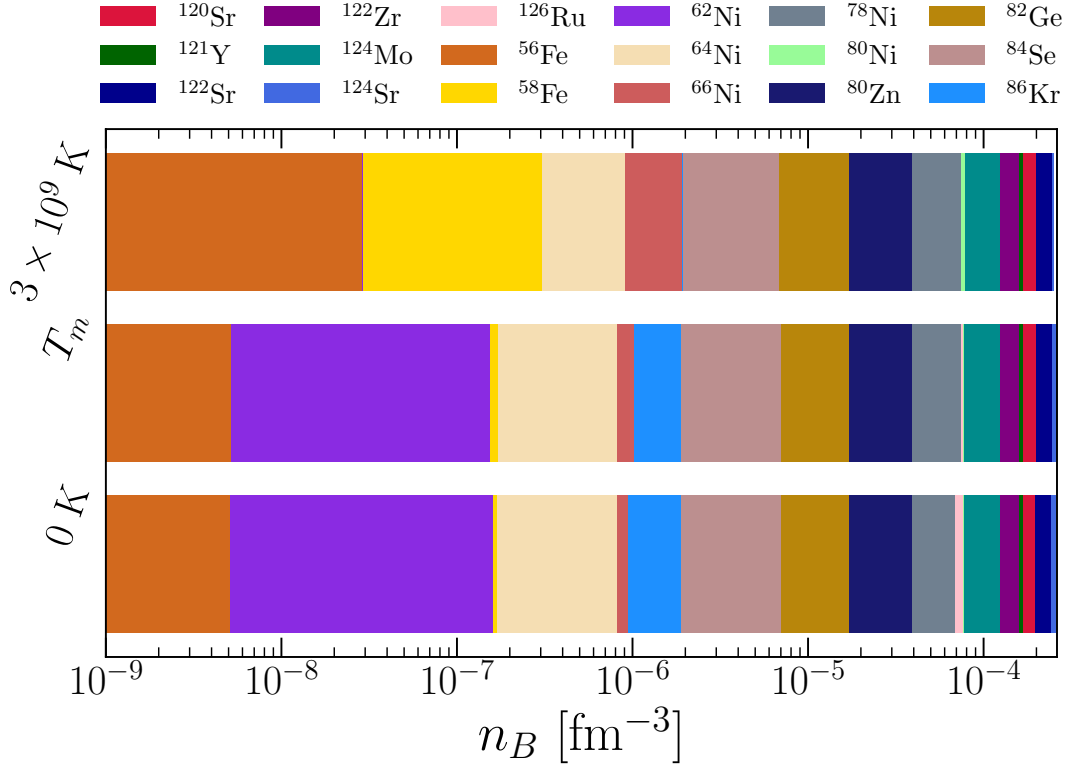
Figure 3.3: Equilibrium composition of a OCP as a function of baryon density n_B in the outer crust at $T = 0$ K, $T = T_m$, and $T = 3 \times 10^9$ K. Experimental data are supplemented with masses from microscopic HFB-24 theoretical mass table [GCP13].

The model dependence of the crystallization temperature of a OCP is illustrated in the right panel of Fig. 3.2, where T_m is represented as a function of P for four different models that supplement experimental data: HFB-24, HFB-26 [GCP13], HFB-14 [GSP07], and FRDM [Mol+95]. As for the equilibrium composition of CCM, see Fig. 1.1, the crystallization temperature becomes sensitive to the model from $P \approx 3 \times 10^{-5}$ MeV/fm^3, due to nuclei being so neutron rich that experimental masses are not available. We can see that the results are very close for HFB-24, HFB-26, and FRDM, once again showing the importance of including the small thermal corrections in the calculation.

3.2.2 Equilibrium composition

The crystallization temperature in the outer crust does not exceed ≈ 0.25 MeV, which is very low from the nuclear physics point of view. Hence, one can ask whether the composition at crystallization is different to that of CCM, presented in Section 1.1. Fig. 3.3 shows the equilibrium composition of a OCP as a function of the baryon density
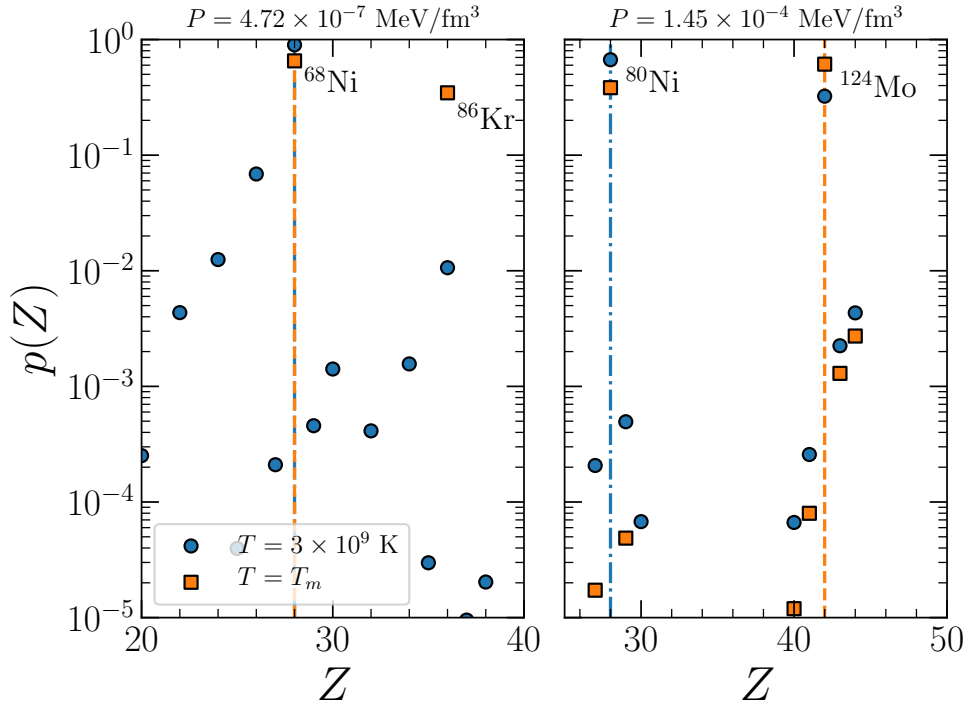
Figure 3.4: Normalized probability distribution $p(Z)$ for $P = 4.72 \times 10^{-7}$ MeV/fm^3 (left panel) and $P = 1.45 \times 10^{-4}$ MeV/fm^3 (right panel) at $T = 3 \times 10^9$ K (blue circles) and $T = T_m$ (orange squares). The blue dashdotted and orange dashed vertical lines indicate the OCP solution at $T = 3 \times 10^9$ K and $T = T_m$, respectively. Experimental data are supplemented with masses from microscopic HFB-24 theoretical mass table [GCP13]. Figure inspired from [Fan+20].

n_B in the regime of the outer crust for two different temperatures: $T = 0$ K (CCM) and $T = 3 \times 10^9$ K, and at crystallization, $T = T_m$. We make use of the microscopic HFB-24 theoretical mass table to complement the experimental data. Let us notice that for all densities encountered in the outer crust, nonlinear mixing effects are so small that the equilibrium nucleus obtained within OCP approximation coincides with the most probable ion in the MCP mixture. We find that the difference between $T = 0$ K and $T = T_m$ is very small and hardly visible in the figure. The exact same sequence of layers is observed in the two cases, only the transition densities being slightly different. This shows that the CCM hypothesis gives an accurate description of the composition of the outer crust at crystallization. Significant deviations with respect to the results at $T = 0$ K and $T = T_m$ are observed at $T = 3 \times 10^9$ K, which is above the crystallization temperature in the outer crust. In particular, the layers of ^{62}Ni and ^{86}Kr are not recovered, and ^{80}Ni is favored over ^{126}Ru around $n_B \approx 8 \times 10^{-5}$ fm^{-3}.

The normalized probability distribution $p(Z)$ of the MCP mixture is represented in Fig. 3.4 for different thermodynamic conditions relevant for the regime of the outer
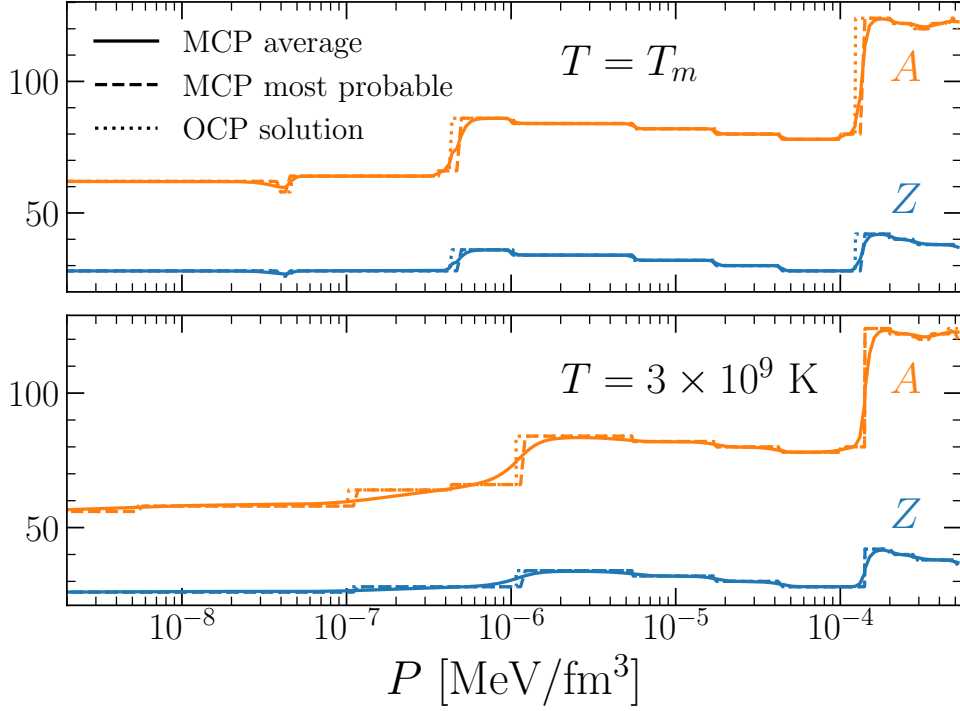
Figure 3.5:   Average (solid lines) and most probable values (dashed lines) of the charge number Z (blue lines) and mass number A (orange lines) in the MCP mixture as a function of pressure in the regime of the outer crust at $T = T_m$ (upper panel) and $T = 3 \times 10^9$ K (lower panel). The OCP solution is represented in dotted lines. Experimental data are supplemented with masses from microscopic HFB-24 theoretical mass table [GCP13]. Figure inspired from [Fan+20].

crust: $P = 4.72 \times 10^{-7}$ MeV/fm^3 (left panel) and $P = 1.45 \times 10^{-4}$ MeV/fm^3 (right panel). For both selected values of pressure, we plot the distribution for $T = 3 \times 10^9$ K (blue circles) and for the crystallization temperature $T = T_m$ calculated within the OCP approximation (orange squares). For each selected thermodynamic condition, it is observed that the most probable Z in the MCP mixture coincide with the OCP solution represented by a vectical line. At low pressure, the crystallization temperature is small and consequently only very few configurations are expected to occur. This can be seen in the left panel of the figure, $P = 4.72 \times 10^{-7}$ MeV/fm^3, where only $Z = 28$ ($p(^{66}\text{Ni}) = 0.65$) and $Z = 36$ ($p(^{86}\text{Kr}) = 0.35$) are associated to nonnegligible probabilities. This contrasts with the distribution calculated at $T = 3 \times 10^9$ K for the same value of pressure, for which a large number of configurations are found with $p(Z) > 10^{-5}$. Still, at this temperature the distribution is strongly peaked at $Z = 28$, while for $T = T_m$ the distribution is bimodal. In the right panel of Fig. 3.4, a bimodal behavior is also clearly exhibited around $Z = 28$ and $Z = 42$, respectively corresponding to ^{80}Ni and ^{124}Mo, in the vicinity of $P = 1.45 \times 10^{-4}$ MeV/fm^3, where the curve of

the crystallization temperature becomes very steep, see Fig. 3.2. While ^{124}Mo is favored over ^{80}Ni at high temperature, it turns out that the most probable nucleus change to ^{80}Ni as the temperature is decreased, and ultimately corresponds to the most probable nucleus at the crystallization temperature. The same feature is observed for the OCP solution.

Fig. 3.5 shows the equilibrium composition of the MCP as a function of pressure in the regime of the outer crust at the crystallization temperature (upper panel) and at $T = 3 \times 10^9$ K (lower panel). At $T = T_m$, it is seen that the average equilibrium values $\langle Z \rangle$ and $\langle A \rangle$ (solid blue and orange lines, respecitvely) coincides almost perfectly with the OCP solution (dotted blue and orange lines), apart in the vicinity of $P = 4.5 \times 10^{-7}$ MeV/fm^3 and $P = 1.5 \times 10^{-4}$ MeV/fm^3, where the distribution $p(Z)$ exhibits a bimodal character, as observed in Fig. 3.4. This results in the sotening of the shell effects, which is even more striking at $T = 3 \times 10^9$ K. Those deviations from the OCP approximation are reflected in the Coulomb coupling parameter, which exhibits spikes and can be as high as ≈ 330 at the crystallization temperature, see Fig. 4 of [Fan+20].

3.2.3 Impurity parameter

Once the abundancies of the different ions are computed via Eq. (3.34), the so-called impurity parameter of the solid crust, which represents the variance of the ionic charge distribution, can be evaluated. It is defined as [Mei+18]

$$Q_{\mathrm{imp}} = \sum_j p(Z^{(j)})(Z^{(j)} - \langle Z \rangle)^2, \tag{3.65}$$

where $p(Z^{(j)})$ represents the normalized probability distribution, that is integrated over all $N^{(j)}$, of the atomic number $Z^{(j)}$. The impurity parameter allows to quantify the presence of amorphous and heterogeneous phases in the crust, which is expected to reduce the electrical conductivity of the solid crust. In consequence, the impurity facotr is expected to play an important role in the magneto-thermal evolution of the star (see the discussion in Sect. 7 in [Mei+18] for a review). For instance, Q_{imp} is directly related to impurity scattering, which alters the cooling of the crust. In NS cooling simulations, the impurity parameter is generally taken as a free parameter which is directly fitted to cooling data.

3.2.4   Abundancies of odd nuclei

3.3   Study of the inner crust at crystallization

3.3.1   Influence of shell effects in the OCP approximation

3.3.1.1   Temperature dependence of shell corrections

3.3.1.2   Equilibrium composition at crystallization for modern BSk functionals

3.3.2   Equilibrium composition of the MCP and the importance of the rearrangement term

3.3.3   Dependence of the impurity parameter on the EoS

3.4   Conclusion

Appendix A

Energy density of a relativistic electron gas

We give here the derivation of the energy density of a relativistic electron gas of density n_e at zero temperature.

From $\approx 10^{14}$ g/cm^3, electrons are essentially free. In this case, the energy density is given by

$$\varepsilon_e = \frac{c}{\pi^2} \int_{k=0}^{k_e} dk k^2 \sqrt{\hbar^2 k^2 + m_e^2 c^2},$$ (A.1)

c being the speed of light, $\hbar$ the reduced Planck constant, and m_e the electron mass. The electron Fermi wave number k_e is related to the electron density via $k_e = (3\pi^2 n_e)^{1/3}$. Making a simple variable, $x = \hbar k/(m_e c)$, we can rewrite the energy density as

$$\varepsilon_e = \frac{m_e^4 c^5}{\pi^2 \hbar^3} \xi(x_r)$$ (A.2)

with $x_r = \hbar k_e/(m_e c)$ and

$$\xi = \int_{x=0}^{x_r} dx x^2 \sqrt{x^2 + 1}.$$ (A.3)

Integrating by parts, it follows

$$\begin{aligned}
\xi &= \left[\frac{x^3}{3}\sqrt{x^2+1}\right]_0^{x_r} - \int_0^{x_r} dx \frac{x^4}{3\sqrt{x^2+1}} \\
3\xi &= x_r^3 \sqrt{x_r^2+1} - \int_0^{x_r} dx x^2 \left(\frac{x^2+1}{\sqrt{x^2+1}} - \frac{1}{\sqrt{x^2+1}}\right) \\
4\xi &= x_r^3 \sqrt{x_r^2+1} + \int_0^{x_r} dx \frac{x^2}{\sqrt{x^2+1}}.
\end{aligned}$$ (A.4)

We have

$$\frac{d}{dx}\left(x\sqrt{x^2+1}\right) = \sqrt{x^2+1} + \frac{x^2}{\sqrt{x^2+1}},$$ (A.5)

and

$$\frac{d}{dx}\left[\ln(x + \sqrt{x^2+1})\right] = \sqrt{x^2+1} - \frac{x^2}{\sqrt{x^2+1}}.$$ (A.6)

thus,

$$\frac{1}{2}\frac{d}{dx}\left[x\sqrt{x^2+1}-\ln\left(x+\sqrt{x^2+1}\right)\right]=\frac{x^2}{\sqrt{x^2+1}}. \tag{A.7}$$

Hence,

$$4\xi = x_r^3\sqrt{x_r^2+1}+\frac{1}{2}\left[x\sqrt{x^2+1}-\ln\left(x+\sqrt{x^2+1}\right)\right]_0^{x_r}, \tag{A.8}$$

which finally gives

$$\varepsilon_e(n_e)=\frac{m_e^4 c^5}{8\pi^2\hbar^3}\left[x_r(2x_r^2+1)\gamma_r-\ln(x_r+\gamma_r)\right], \tag{A.9}$$

where we have introduced the parameter parameter $\gamma_r=\sqrt{x_r^2+1}$.

Appendix B

Neutron and proton chemical potentials in the metamodel

From the metamodeling of the nuclear matter energy, Eq. 1.37, we give here the complete expressions of the neutron and proton chemical potentials for a homogeneous system characterized by a neutron density n_n and proton density n_p at zero temperature. Let us introduce the variables $x = (n - n_{sat})/(3n_{sat})$ and $\delta = (n_n - n_p)/n$, $n = n_n + n_p$ being the total baryon density.

The neutron chemical potential, with the rest mass energy $m_n c^2$, is given by

$$\mu_{HM,n} = e_{HM}(n_n, n_p) + n\left(\frac{\partial e_{HM}}{\partial n_n}\right)_{n_p} + m_n c^2 \tag{B.1}$$

$$\mu_{HM,n} = e_{HM}(n, \delta) + \frac{1 + 3x}{3}\left(\frac{\partial e_{HM}}{\partial x}\right)_\delta + (1 - \delta)\left(\frac{\partial e_{HM}}{\partial \delta}\right)_x + m_n c^2. \tag{B.2}$$

Equivalently, the proton chemical potential is given by

$$\mu_{HM,p} = e_{HM}(n, \delta) + \frac{1 + 3x}{3}\left(\frac{\partial e_{HM}}{\partial x}\right)_\delta - (1 + \delta)\left(\frac{\partial e_{HM}}{\partial \delta}\right)_x + m_p c^2. \tag{B.3}$$

We first go through the derivative with respect to x, yielding

$$
\begin{aligned}
\left(\frac{\partial e_{HM}}{\partial x}\right)_\delta = {} & \frac{5}{1 + 3x} t_{HM}^{FG}(n, \delta) \\
& - \frac{3}{1 + 3x}\frac{1}{2} t_{sat}^{FG}(1 + 3x)^{2/3}\left[(1 + \delta)^{5/3} + (1 - \delta)^{5/3}\right] \\
& + \sum_{\alpha \geq 0}(v_\alpha^{is} + v_\alpha^{iv}\delta^2)\frac{1}{\alpha!}\left(\alpha x^{\alpha-1} u_\alpha(x) + x^\alpha \frac{du_\alpha}{dx}\right).
\end{aligned} \tag{B.4}
$$

Let us notice that is gives the expression for the total pressure,

$$P_{HM}(n, \delta) = n^2\left(\frac{\partial e_{HM}}{\partial n}\right)_\delta \tag{B.5}$$

$$= \frac{1}{3}n_{sat}(1 + 3x)^2\left(\frac{\partial e_{HM}}{\partial x}\right)_\delta. \tag{B.6}$$

We now turn to the derivative with respect to the asymmetry δ,

$$
\begin{aligned}
\left(\frac{\partial e_{HM}}{\partial \delta}\right)_x =\ & \frac{1}{2}t^{FG}_{sat}(1+3x)^{5/3}\left[(1+\delta)^{5/3}-(1-\delta)^{5/3}\right] \\
& +\frac{5}{6}t^{FG}_{sat}(1+3x)^{2/3}\left[(1+\delta)^{2/3}\frac{m}{m^*_n}-(1-\delta)^{2/3}\frac{m}{m^*_p}\right] \\
& +2\delta\sum_{\alpha\geq 0}v^{iv}_\alpha\frac{x^\alpha}{\alpha!}u_\alpha(x).
\end{aligned}
\tag{B.7}
$$

Appendix C

Total pressure in the inner crust

Bibliography

[Abb+17]   B. P. Abbott et al. "GW170817: Observation of Gravitational Waves from a Binary Neutron Star Inspiral". In: *Phys. Rev. Lett.* 119 (16 Oct. 2017), p. 161101. DOI: 10.1103/PhysRevLett.119.161101.

[Abb+18]   B. P. Abbott et al. "GW170817: Measurements of Neutron Star Radii and Equation of State". In: *Phys. Rev. Lett.* 121 (16 Oct. 2018), p. 161101. DOI: 10.1103/PhysRevLett.121.161101.

[Abb+19]   B. P. Abbott et al. "Properties of the Binary Neutron Star Merger GW170817". In: *Phys. Rev. X* 9 (1 Jan. 2019), p. 011001. DOI: 10.1103/PhysRevX.9.011001.

[AI75]   P. W. Anderson and N. Itoh. "Pulsar glitches and restlessness as a hard superfluidity phenomenon". In: *Nature* 256 (1975), pp. 25–27. DOI: 10.1038/256025a0.

[Ala+16]   N. Alam et al. "Strong correlations of neutron star radii with the slopes of nuclear matter incompressibility and symmetry energy at saturation". In: *Phys. Rev. C* 94 (5 Nov. 2016), p. 052801. DOI: 10.1103/PhysRevC.94.052801.

[And+12]   N. Andersson et al. "Pulsar Glitches: The Crust is not Enough". In: *Phys. Rev. Lett.* 109 (24 Dec. 2012), p. 241103. DOI: 10.1103/PhysRevLett.109.241103.

[Ant+13]   John Antoniadis et al. "A Massive Pulsar in a Compact Relativistic Binary". In: *Science* 340.6131 (2013). DOI: 10.1126/science.1233232. eprint: https://science.sciencemag.org/content/340/6131/1233232.full.pdf.

[Ant+19]   Sofija Antić et al. "Quantifying the uncertainties on spinodal instability for stellar matter through meta-modeling". In: *Journal of Physics G: Nuclear and Particle Physics* 46.6 (May 2019), p. 065109. DOI: 10.1088/1361-6471/ab1a51.

[APR98]   A. Akmal, V. R. Pandharipande, and D. G. Ravenhall. "Equation of state of nucleon matter and neutron star structure". In: *Phys. Rev. C* 58 (3 Sept. 1998), pp. 1804–1828. DOI: 10.1103/PhysRevC.58.1804.

[Aud+12]   G. Audi et al. "The Ame2012 atomic mass evaluation". In: *Chinese Physics C* 36.12 (Dec. 2012), pp. 1287–1602. DOI: 10.1088/1674-1137/36/12/002.

[Ava+08]   S. S. Avancini et al. "Warm and cold pasta phase in relativistic mean field theory". In: *Phys. Rev. C* 78 (1 July 2008), p. 015802. DOI: 10.1103/PhysRevC.78.015802.

[Ava+10]   Sidney S. Avancini et al. "Warm "pasta" phase in the Thomas-Fermi approximation". In: *Phys. Rev. C* 82 (5 Nov. 2010), p. 055807. DOI: 10.1103/PhysRevC.82.055807.

[Bay+19]   Gordon Baym et al. "New Neutron Star Equation of State with Quark-Hadron Crossover". In: *Astrophys. J.* 885.1, 42 (Nov. 2019), p. 42. DOI: 10.3847/1538-4357/ab441e. arXiv: 1903.08963 [astro-ph.HE].

[BBP71]   Gordon Baym, Hans A. Bethe, and Christopher J Pethick. "Neutron star matter". In: *Nuclear Physics A* 175.2 (1971), pp. 225–271. DOI: https://doi.org/10.1016/0375-9474(71)90281-8.

[Bed+12]   Bednarek, I. et al. "Hyperons in neutron-star cores and a $2M_\odot$ pulsar". In: *A&A* 543 (2012), A157. DOI: 10.1051/0004-6361/201118560.

[BH80]   Marc Baus and Jean-Pierre Hansen. "Statistical mechanics of simple coulomb systems". In: *Physics Reports* 59.1 (1980), pp. 1–94. DOI: https://doi.org/10.1016/0370-1573(80)90022-8.

[BMG20]   Celso C. Barros, Débora P. Menezes, and Francesca Gulminelli. "Fluctuations in the composition of nuclear pasta in symmetric nuclear matter at finite temperature". In: *Phys. Rev. C* 101 (3 Mar. 2020), p. 035211. DOI: 10.1103/PhysRevC.101.035211.

[BPS71]   Gordon Baym, Christopher Pethick, and Peter Sutherland. "The Ground state of matter at high densities: Equation of state and stellar models". In: *Astrophys. J.* 170 (1971), pp. 299–317. DOI: 10.1086/151216.

[BPY01]   D. A. Baiko, A. Y. Potekhin, and D. G. Yakovlev. "Thermodynamic functions of harmonic Coulomb crystals". In: *Phys. Rev. E* 64 (5 Oct. 2001), p. 057402. DOI: 10.1103/PhysRevE.64.057402.

[Bro65]   C. G. Broyden. "A Class of Methods for Solving Nonlinear Simultaneous Equations". In: *Mathematics of Computation* 19.92 (1965), pp. 577–593.

[BW39]   Niels Bohr and John Archibald Wheeler. "The Mechanism of Nuclear Fission". In: *Phys. Rev.* 56 (5 Sept. 1939), pp. 426–450. DOI: 10.1103/PhysRev.56.426.

[Car+20]   Carreau, T. et al. "Crystallization of the inner crust of a neutron star and the influence of shell effects". In: *A&A* 635 (2020), A84. DOI: 10.1051/0004-6361/201937236.

[Car17a]   T. Carreau. https://github.com/thomascarreau/NSEoS. 2017.

[Car17b]   T. Carreau. "Vers une description unifiée de la croûte et du coeur des étoiles à neutrons". MA thesis. Université de Caen-Normandie, 2017.

[CF16]   N. Chamel and A. F. Fantina. "Binary and ternary ionic compounds in the outer crust of a cold nonaccreting neutron star". In: *Phys. Rev. C* 94 (6 Dec. 2016), p. 065802. DOI: 10.1103/PhysRevC.94.065802.

[CFG20]   T. Carreau, A. F. Fantina, and F. Gulminelli. *Inner crust of a neutron star at crystallization in a multi-component approach.* 2020. arXiv: 2005.02089 [astro-ph.HE].

[CGM19a]   Carreau, Thomas, Gulminelli, Francesca, and Margueron, Jérôme. "Bayesian analysis of the crust-core transition with a compressible liquid-drop model". In: *Eur. Phys. J. A* 55.10 (2019), p. 188. DOI: 10.1140/epja/i2019-12884-1.

[CGM19b]   Thomas Carreau, Francesca Gulminelli, and Jérôme Margueron. "General predictions for the neutron star crustal moment of inertia". In: *Phys. Rev. C* 100 (5 Nov. 2019), p. 055803. DOI: 10.1103/PhysRevC.100.055803.

[CGS14]   Colò, G., Garg, U., and Sagawa, H. "Symmetry energy from the nuclear collective motion: constraints from dipole, quadrupole, monopole and spin-dipole resonances". In: *Eur. Phys. J. A* 50.2 (2014), p. 26. DOI: 10.1140/epja/i2014-14026-9.

[Cha+07]   N. Chamel et al. "Validity of the Wigner-Seitz approximation in neutron star crust". In: *Phys. Rev. C* 75 (5 May 2007), p. 055806. DOI: 10.1103/PhysRevC.75.055806.

[Cha+17]   D. Chatterjee et al. "Constraints on the nuclear equation of state from nuclear masses and radii in a Thomas-Fermi meta-modeling approach". In: *Phys. Rev. C* 96 (6 Dec. 2017), p. 065805. DOI: 10.1103/PhysRevC.96.065805.

[Cha+98]   E. Chabanat et al. "A Skyrme parametrization from subnuclear to neutron star densities Part II. Nuclei far from stabilities". In: *Nuclear Physics A* 635.1 (1998), pp. 231–256. DOI: https://doi.org/10.1016/S0375-9474(98)00180-8.

[Cha06]   Nicolas Chamel. "Effective mass of free neutrons in neutron star crust". In: *Nuclear Physics A* 773.3 (2006), pp. 263–278. DOI: https://doi.org/10.1016/j.nuclphysa.2006.04.010.

[Cha12]   N. Chamel. "Neutron conduction in the inner crust of a neutron star in the framework of the band theory of solids". In: *Phys. Rev. C* 85 (3 Mar. 2012), p. 035801. DOI: 10.1103/PhysRevC.85.035801.

[Cha13]   N. Chamel. "Crustal Entrainment and Pulsar Glitches". In: *Phys. Rev. Lett.* 110 (1 Jan. 2013), p. 011101. DOI: 10.1103/PhysRevLett.110.011101.

[Cro+20]   H. T. Cromartie et al. "Relativistic Shapiro delay measurements of an extremely massive millisecond pulsar". In: *Nature Astronomy* 4 (Jan. 2020), pp. 72–76. DOI: 10.1038/s41550-019-0880-2. arXiv: 1904.06759 [astro-ph.HE].

[DCG07]   C. Ducoin, Ph. Chomaz, and F. Gulminelli. "Isospin-dependent clusterization of neutron-star matter". In: *Nuclear Physics A* 789.1 (2007), pp. 403–425. DOI: https://doi.org/10.1016/j.nuclphysa.2007.03.006.

[De+18]   Soumi De et al. "Tidal Deformabilities and Radii of Neutron Stars from the Observation of GW170817". In: *Phys. Rev. Lett.* 121 (9 Aug. 2018), p. 091102. DOI: `10.1103/PhysRevLett.121.091102`.

[Del+16]   T. Delsate et al. "Giant pulsar glitches and the inertia of neutron star crusts". In: *Phys. Rev. D* 94 (2 July 2016), p. 023008. DOI: `10.1103/PhysRevD.94.023008`.

[Dem+10]   P. B. Demorest et al. "A two-solar-mass neutron star measured using Shapiro delay". In: *Nature Astronomy* 467.7319 (Oct. 2010), pp. 1081–1083. DOI: `10.1038/nature09466`. arXiv: `1010.5788 [astro-ph.HE]`.

[DH00]   F Douchin and P Haensel. "Inner edge of neutron-star crust with SLy effective nucleon-nucleon interactions". In: *Physics Letters B* 485.1 (2000), pp. 107–114. DOI: `https://doi.org/10.1016/S0370-2693(00)00672-9`.

[DH01]   Douchin, F. and Haensel, P. "A unified equation of state of dense matter and neutron star structure". In: *A&A* 380.1 (2001), pp. 151–167. DOI: `10.1051/0004-6361:20011402`.

[DHM00]   F Douchin, P Haensel, and J Meyer. "Nuclear surface and curvature properties for SLy Skyrme forces and nuclei in the inner neutron-star crust". In: *Nuclear Physics A* 665.3 (2000), pp. 419–446. DOI: `https://doi.org/10.1016/S0375-9474(99)00397-8`.

[DHS16]   C. Drischler, K. Hebeler, and A. Schwenk. "Asymmetric nuclear matter based on chiral two- and three-nucleon interactions". In: *Phys. Rev. C* 93 (5 May 2016), p. 054314. DOI: `10.1103/PhysRevC.93.054314`.

[DL14]   Pawel Danielewicz and Jenny Lee. "Symmetry energy II: Isobaric analog states". In: *Nuclear Physics A* 922 (2014), pp. 1–70. DOI: `https://doi.org/10.1016/j.nuclphysa.2013.11.005`.

[DMC08]   C. Ducoin, J. Margueron, and Ph. Chomaz. "Cluster formation in asymmetric nuclear matter: Semi-classical and quantal approaches". In: *Nuclear Physics A* 809.1 (2008), pp. 30–64. DOI: `https://doi.org/10.1016/j.nuclphysa.2008.05.015`.

[DNR14]   J Dobaczewski, W Nazarewicz, and P-G Reinhard. "Error estimates of theoretical models: a guide". In: *Journal of Physics G: Nuclear and Particle Physics* 41.7 (May 2014), p. 074001. DOI: `10.1088/0954-3899/41/7/074001`.

[Duc+07]   C. Ducoin et al. "Anomalous thermodynamics and phase transitions in neutron star matter". In: *Phys. Rev. C* 75 (6 June 2007), p. 065805. DOI: `10.1103/PhysRevC.75.065805`.

[Duc+11]   Camille Ducoin et al. "Core-crust transition in neutron stars: Predictivity of density developments". In: *Phys. Rev. C* 83 (4 Apr. 2011), p. 045810. DOI: `10.1103/PhysRevC.83.045810`.

[Esp+11]   C. M. Espinoza et al. "A study of 315 glitches in the rotation of 102 pulsars". In: *Monthly Notices of the Royal Astronomical Society* 414.2 (June 2011), pp. 1679–1704. DOI: 10.1111/j.1365-2966.2011.18503.x. eprint: https://academic.oup.com/mnras/article-pdf/414/2/1679/3015039/mnras0414-1679.pdf.

[Fan+20]   Fantina, A. F. et al. "Crystallization of the outer crust of a non-accreting neutron star". In: *A&A* 633 (2020), A149. DOI: 10.1051/0004-6361/201936359.

[FF18]   G. Fiorella Burgio and Anthea F. Fantina. "Nuclear Equation of State for Compact Stars and Supernovae". In: *The Physics and Astrophysics of Neutron Stars.* Ed. by Luciano Rezzolla et al. Cham: Springer International Publishing, 2018, pp. 255–335. DOI: 10.1007/978-3-319-97616-7_6.

[FH93]   R. T. Farouki and S. Hamaguchi. "Thermal energy of the crystalline one-component plasma from dynamical simulations". In: *Phys. Rev. E* 47 (6 June 1993), pp. 4330–4336. DOI: 10.1103/PhysRevE.47.4330.

[FMT49]   R. P. Feynman, N. Metropolis, and E. Teller. "Equations of State of Elements Based on the Generalized Fermi-Thomas Theory". In: *Phys. Rev.* 75 (10 May 1949), pp. 1561–1573. DOI: 10.1103/PhysRev.75.1561.

[For+15]   M. Fortin et al. "Neutron stars with hyperon cores: stellar radii and equation of state near nuclear density". In: *Astron. Astrophys.* 576 (2015), A68. DOI: 10.1051/0004-6361/201424800. arXiv: 1408.3052 [astro-ph.SR].

[For+16]   M. Fortin et al. "Neutron star radii and crusts: Uncertainties and unified equations of state". In: *Phys. Rev. C* 94 (3 Sept. 2016), p. 035804. DOI: 10.1103/PhysRevC.94.035804.

[Gan+14]   Gandolfi, S. et al. "The equation of state of neutron matter, symmetry energy and neutron star structure". In: *Eur. Phys. J. A* 50.2 (2014), p. 10. DOI: 10.1140/epja/i2014-14010-5.

[GAO12]   Keith C. Gendreau, Zaven Arzoumanian, and Takashi Okajima. "The Neutron star Interior Composition ExploreR (NICER): an Explorer mission of opportunity for soft x-ray timing spectroscopy". In: *Space Telescopes and Instrumentation 2012: Ultraviolet to Gamma Ray.* Ed. by Tadayuki Takahashi, Stephen S. Murray, and Jan-Willem A. den Herder. Vol. 8443. International Society for Optics and Photonics. SPIE, 2012, pp. 322–329. DOI: 10.1117/12.926396.

[GCP13]   S. Goriely, N. Chamel, and J. M. Pearson. "Further explorations of Skyrme-Hartree-Fock-Bogoliubov mass formulas. XIII. The 2012 atomic mass evaluation and the symmetry coefficient". In: *Phys. Rev. C* 88 (2 Aug. 2013), p. 024308. DOI: 10.1103/PhysRevC.88.024308.

[Gon+17]   C. Gonzalez-Boquera et al. "Higher-order symmetry energy and neutron star core-crust transition with Gogny forces". In: *Phys. Rev. C* 96 (6 Dec. 2017), p. 065806. DOI: 10.1103/PhysRevC.96.065806.

[Gor+05]   S. Goriely et al. "Further explorations of Skyrme–Hartree–Fock–Bogoliubov mass formulas. IV: Neutron-matter constraint". In: *Nuclear Physics A* 750.2 (2005), pp. 425–443. DOI: https://doi.org/10.1016/j.nuclphysa.2005.01.009.

[Gor+11]   Goriely, S. et al. "The decompression of the outer neutron star crust and r-process nucleosynthesis". In: *A&A* 531 (2011), A78. DOI: 10.1051/0004-6361/201116897.

[GPA12]   Fabrizio Grill, Constan ça Providência, and Sidney S. Avancini. "Neutron star inner crust and symmetry energy". In: *Phys. Rev. C* 85 (5 May 2012), p. 055808. DOI: 10.1103/PhysRevC.85.055808.

[GR15]   F. Gulminelli and Ad. R. Raduta. "Unified treatment of subsaturation stellar matter at zero and finite temperature". In: *Phys. Rev. C* 92 (5 Nov. 2015), p. 055803. DOI: 10.1103/PhysRevC.92.055803.

[Gra+17]   Guilherme Grams et al. "Nuclear pasta phases within the quark-meson coupling model". In: *Phys. Rev. C* 95 (5 May 2017), p. 055807. DOI: 10.1103/PhysRevC.95.055807.

[Gra+18]   G. Grams et al. "Distribution of nuclei in equilibrium stellar matter from the free-energy density in a Wigner-Seitz cell". In: *Phys. Rev. C* 97 (3 Mar. 2018), p. 035807. DOI: 10.1103/PhysRevC.97.035807.

[GSP07]   S. Goriely, M. Samyn, and J. M. Pearson. "Further explorations of Skyrme-Hartree-Fock-Bogoliubov mass formulas. VII. Simultaneous fits to masses and fission barriers". In: *Phys. Rev. C* 75 (6 June 2007), p. 064312. DOI: 10.1103/PhysRevC.75.064312.

[Har67]   James B. Hartle. "Slowly Rotating Relativistic Stars. I. Equations of Structure". In: *Astrophys. J.* 150 (Dec. 1967), p. 1005. DOI: 10.1086/149400.

[Hew+68]   A. Hewish et al. "Observation of a rapidly pulsating radio source". In: *Nature* 217 (1968), pp. 709–713. DOI: 10.1038/217709a0.

[Hin+10]   Tanja Hinderer et al. "Tidal deformability of neutron stars with realistic equations of state and their gravitational wave signatures in binary inspiral". In: *Phys. Rev. D* 81 (12 June 2010), p. 123016. DOI: 10.1103/PhysRevD.81.123016.

[Ho+15]   Wynn C. G. Ho et al. "Pinning down the superfluid and measuring masses using pulsar glitches". In: *Science Advances* 1.9 (2015). DOI: 10.1126/sciadv.1500578. eprint: https://advances.sciencemag.org/content/1/9/e1500578.full.pdf.

[Hor69]   H.M. [Van Horn]. "Crystallization of a classical, one-component coulomb plasma". In: *Physics Letters A* 28.10 (1969), pp. 706–707. DOI: https://doi.org/10.1016/0375-9601(69)90699-9.

[HP94]   P. Haensel and B. Pichon. "Experimental nuclear masses and the ground state of cold dense matter". In: *Astron. Astrophys.* 283 (1994), p. 313. arXiv: nucl-th/9310003 [nucl-th].

[HPY07]   P. Haensel, A. Y. Potekhin, and D. G. Yakovlev. *Neutron stars 1: Equation of state and structure*. Vol. 326. 2007, pp.1–619. DOI: 10.1007/978-0-387-47301-7.

[Hu+20]   Jinniu Hu et al. *Effects of symmetry energy on the radius and tidal deformability of neutron stars in relativistic mean-field model*. 2020. arXiv: 2002.00562 [nucl-th].

[Hua+17]   W.J. Huang et al. "The AME2016 atomic mass evaluation (I). Evaluation of input data; and adjustment procedures". In: *Chinese Physics C* 41.3 (Mar. 2017), p. 030002. DOI: 10.1088/1674-1137/41/3/030002.

[Ji+19]   Fan Ji et al. "Effects of nuclear symmetry energy and equation of state on neutron star properties". In: *Phys. Rev. C* 100 (4 Oct. 2019), p. 045801. DOI: 10.1103/PhysRevC.100.045801.

[Jod]   Jodrell Bank Centre for Astrophysics. *Glitch Catalogue*. http://www.jb.man.ac.uk/pulsar/glitches.html.

[Kor+12]   M. Kortelainen et al. "Nuclear energy density optimization: Large deformations". In: *Phys. Rev. C* 85 (2 Feb. 2012), p. 024304. DOI: 10.1103/PhysRevC.85.024304.

[LEL99]   Bennett Link, Richard I. Epstein, and James M. Lattimer. "Pulsar Constraints on Neutron Star Structure and Equation of State". In: *Phys. Rev. Lett.* 83 (17 Oct. 1999), pp. 3362–3365. DOI: 10.1103/PhysRevLett.83.3362.

[LH19]   Lim, Y. and Holt, J. W. "Bayesian modeling of the nuclear equation of state for neutron star tidal deformabilities and GW170817". In: *Eur. Phys. J. A* 55.11 (2019), p. 209. DOI: 10.1140/epja/i2019-12917-9.

[LHS19]   Yeunhwan Lim, Jeremy W. Holt, and Robert J. Stahulak. "Predicting the moment of inertia of pulsar J0737-3039A from Bayesian modeling of the nuclear equation of state". In: *Phys. Rev. C* 100 (3 Sept. 2019), p. 035802. DOI: 10.1103/PhysRevC.100.035802.

[Li+14]   Bao-An Li et al. *Topical issue on nuclear symmetry energy*. 2014.

[Li17]   Bao-An Li. "Origins and impacts of high-density symmetry energy". In: *AIP Conference Proceedings* 1852.1 (2017), p. 030005. DOI: 10.1063/1.4984856. eprint: https://aip.scitation.org/doi/pdf/10.1063/1.4984856.

[Lon+04]   Wenhui Long et al. "New effective interactions in relativistic mean field theory with nonlinear terms and density-dependent meson-nucleon coupling". In: *Phys. Rev. C* 69 (3 Mar. 2004), p. 034319. DOI: 10.1103/PhysRevC.69.034319.

[LPT03]   D. Lunney, J. M. Pearson, and C. Thibault. "Recent trends in the determination of nuclear masses". In: *Rev. Mod. Phys.* 75 (3 Aug. 2003), pp. 1021–1082. DOI: 10.1103/RevModPhys.75.1021.

[LRP93]   C. P. Lorenz, D. G. Ravenhall, and C. J. Pethick. "Neutron star crusts". In: *Phys. Rev. Lett.* 70 (4 Jan. 1993), pp. 379–382. DOI: 10.1103/PhysRevLett.70.379.

[LS08]   Z. H. Li and H.-J. Schulze. "Neutron star structure with modern nucleonic three-body forces". In: *Phys. Rev. C* 78 (2 Aug. 2008), p. 028801. DOI: `10.1103/PhysRevC.78.028801`.

[LS91]   James M. Lattimer and Douglas F. Swesty. "A generalized equation of state for hot, dense matter". In: *Nuclear Physics A* 535.2 (Dec. 1991), pp. 331–376. DOI: `10.1016/0375-9474(91)90452-C`.

[Mei+18]   Zach Meisel et al. "Nuclear physics of the outer layers of accreting neutron stars". In: *Journal of Physics G: Nuclear and Particle Physics* 45.9 (July 2018), p. 093001. DOI: `10.1088/1361-6471/aad171`.

[MG19]   Jérôme Margueron and Francesca Gulminelli. "Effect of high-order empirical parameters on the nuclear equation of state". In: *Phys. Rev. C* 99 (2 Feb. 2019), p. 025806. DOI: `10.1103/PhysRevC.99.025806`.

[MHG18a]   Jérôme Margueron, Rudiney Hoffmann Casali, and Francesca Gulminelli. "Equation of state for dense nucleonic matter from metamodeling. I. Foundational aspects". In: *Phys. Rev. C* 97 (2 Feb. 2018), p. 025805. DOI: `10.1103/PhysRevC.97.025805`.

[MHG18b]   Jérôme Margueron, Rudiney Hoffmann Casali, and Francesca Gulminelli. "Equation of state for dense nucleonic matter from metamodeling. II. Predictions for neutron star properties". In: *Phys. Rev. C* 97 (2 Feb. 2018), p. 025806. DOI: `10.1103/PhysRevC.97.025806`.

[MN88]   P. Möller and J.R. Nix. "Nuclear masses from a unified macroscopic-microscopic model". In: *Atomic Data and Nuclear Data Tables* 39.2 (1988), pp. 213–223. DOI: `https://doi.org/10.1016/0092-640X(88)90022-8`.

[Mol+95]   P. Moller et al. "Nuclear Ground-State Masses and Deformations". In: *Atomic Data and Nuclear Data Tables* 59.2 (1995), pp. 185–381. DOI: `https://doi.org/10.1006/adnd.1995.1002`.

[Mon+17]   C. Mondal et al. "Interdependence of different symmetry energy elements". In: *Phys. Rev. C* 96 (2 Aug. 2017), p. 021302. DOI: `10.1103/PhysRevC.96.021302`.

[MS65]   W. D. Myers and W. J. Swiatecki. "unpublished". In: *UCRL Report* 11980 (May 1965).

[MS66]   William D. Myers and Wladyslaw J. Swiatecki. "Nuclear masses and deformations". In: *Nuclear Physics* 81.1 (1966), pp. 1–60. DOI: `https://doi.org/10.1016/0029-5582(66)90639-0`.

[MTC09]   Toshiki Maruyama, Toshitaka Tatsumi, and Satoshi Chiba. "Equation of state of nuclear matter in the first order phase transition". In: *AIP Conference Proceedings* 1120.1 (2009), pp. 129–134. DOI: `10.1063/1.3141634`. eprint: `https://aip.scitation.org/doi/pdf/10.1063/1.3141634`.

[MU16]   Noël Martin and Michael Urban. "Superfluid hydrodynamics in the inner crust of neutron stars". In: *Phys. Rev. C* 94 (6 Dec. 2016), p. 065801. DOI: `10.1103/PhysRevC.94.065801`.

[NGL12]   W. G. Newton, M. Gearheart, and Bao-An Li. "A SURVEY OF THE PA-
          RAMETER SPACE OF THE COMPRESSIBLE LIQUID DROP MODEL
          AS APPLIED TO THE NEUTRON STAR INNER CRUST". In: *The As-
          trophysical Journal Supplement Series* 204.1 (Dec. 2012), p. 9. DOI: 10.
          1088/0067-0049/204/1/9.

[NS09]   W. G. Newton and J. R. Stone. "Modeling nuclear "pasta" and the transi-
          tion to uniform nuclear matter with the 3D Skyrme-Hartree-Fock method
          at finite temperature: Core-collapse supernovae". In: *Phys. Rev. C* 79 (5
          May 2009), p. 055801. DOI: 10.1103/PhysRevC.79.055801.

[NV73]   J.W. Negele and D. Vautherin. "Neutron star matter at sub-nuclear densi-
          ties". In: *Nuclear Physics A* 207.2 (1973), pp. 298–320. DOI: https://doi.
          org/10.1016/0375-9474(73)90349-7.

[Oer+17] M. Oertel et al. "Equations of state for supernovae and compact stars". In:
          Rev. Mod. Phys. 89 (1 Mar. 2017), p. 015007. DOI: 10.1103/RevModPhys.
          89.015007.

[Ons+08] M. Onsi et al. "Semi-classical equation of state and specific-heat expressions
          with proton shell corrections for the inner crust of a neutron star". In: *Phys.
          Rev. C* 77 (6 June 2008), p. 065805. DOI: 10.1103/PhysRevC.77.065805.

[OV39]   J. R. Oppenheimer and G. M. Volkoff. "On Massive Neutron Cores". In:
          Phys. Rev. 55 (4 Feb. 1939), pp. 374–381. DOI: 10.1103/PhysRev.55.374.

[Pap+13] P. Papakonstantinou et al. "Densities and energies of nuclei in dilute matter
          at zero temperature". In: *Phys. Rev. C* 88 (4 Oct. 2013), p. 045805. DOI:
          10.1103/PhysRevC.88.045805.

[PC00]   Alexander Y. Potekhin and Gilles Chabrier. "Equation of state of fully
          ionized electron-ion plasmas. II. Extension to relativistic densities and to
          the solid phase". In: *Phys. Rev. E* 62 (6 Dec. 2000), pp. 8554–8563. DOI:
          10.1103/PhysRevE.62.8554.

[PC10]   A. Y. Potekhin and G. Chabrier. "Thermodynamic Functions of Dense Plas-
          mas: Analytic Approximations for Astrophysical Applications". In: *Contri-
          butions to Plasma Physics* 50.1 (2010), pp. 82–87. DOI: 10.1002/ctpp.
          201010017. eprint: https://onlinelibrary.wiley.com/doi/pdf/10.
          1002/ctpp.201010017.

[PCP20]   J. M. Pearson, N. Chamel, and A. Y. Potekhin. "Unified equations of state
          for cold nonaccreting neutron stars with Brussels-Montreal functionals. II.
          Pasta phases in semiclassical approximation". In: *Phys. Rev. C* 101 (1 Jan.
          2020), p. 015802. DOI: 10.1103/PhysRevC.101.015802.

[Pea+12] J. M. Pearson et al. "Inner crust of neutron stars with mass-fitted Skyrme
          functionals". In: *Phys. Rev. C* 85 (6 June 2012), p. 065803. DOI: 10.1103/
          PhysRevC.85.065803.

[Pea+14] Pearson, J. M. et al. "Symmetry energy: nuclear masses and neutron stars".
          In: *Eur. Phys. J. A* 50.2 (2014), p. 43. DOI: 10.1140/epja/i2014-14043-8.

[Pea+18]   J M Pearson et al. "Unified equations of state for cold non-accreting neutron stars with Brussels–Montreal functionals – I. Role of symmetry energy". In: *Monthly Notices of the Royal Astronomical Society* 481.3 (Sept. 2018), pp. 2994–3026. DOI: `10.1093/mnras/sty2413`. eprint: `https://academic.oup.com/mnras/article-pdf/481/3/2994/25817956/sty2413.pdf`.

[Pea+19]   J M Pearson et al. "Erratum: Unified equations of state for cold non-accreting neutron stars with Brussels-Montreal functionals. I. Role of symmetry energy". In: *Monthly Notices of the Royal Astronomical Society* 486.1 (Mar. 2019), pp. 768–768. DOI: `10.1093/mnras/stz800`. eprint: `https://academic.oup.com/mnras/article-pdf/486/1/768/28345283/stz800.pdf`.

[Pea19]   J. M. Pearson. Private communication. 2019.

[PF19]   J. Piekarewicz and F. J. Fattoyev. "Impact of the neutron star crust on the tidal polarizability". In: *Phys. Rev. C* 99 (4 Apr. 2019), p. 045802. DOI: `10.1103/PhysRevC.99.045802`.

[PFH14]   J. Piekarewicz, F. J. Fattoyev, and C. J. Horowitz. "Pulsar glitches: The crust may be enough". In: *Phys. Rev. C* 90 (1 July 2014), p. 015803. DOI: `10.1103/PhysRevC.90.015803`.

[Piz+17]   P. M. Pizzochero et al. "Constraints on pulsar masses from the maximum observed glitch". In: *Nature Astronomy* 1, 0134 (July 2017), p. 0134. DOI: `10.1038/s41550-017-0134`. arXiv: `1611.10223 [astro-ph.HE]`.

[PR95]   C. J. Pethick and D. G. Ravenhall. "Matter at large neutron excess and the physics of neutron-star crusts". In: *Ann. Rev. Nucl. Part. Sci.* 45 (1995), pp. 429–484. DOI: `10.1146/annurev.ns.45.120195.002241`.

[PRL95]   C.J. Pethick, D.G. Ravenhall, and C.P. Lorenz. "The inner boundary of a neutron-star crust". In: *Nuclear Physics A* 584.4 (1995), pp. 675–703. DOI: `https://doi.org/10.1016/0375-9474(94)00506-I`.

[Roc+11]   X. Roca-Maza et al. "Relativistic mean-field interaction with density-dependent meson-nucleon vertices based on microscopical calculations". In: *Phys. Rev. C* 84 (5 Nov. 2011), p. 054309. DOI: `10.1103/PhysRevC.84.054309`.

[RPL83]   D.G. Ravenhall, C.J. Pethick, and J.M. Lattimer. "Nuclear interface energy at finite temperatures". In: *Nuclear Physics A* 407.3 (1983), pp. 571–591. DOI: `https://doi.org/10.1016/0375-9474(83)90667-X`.

[Sam+02]   M. Samyn et al. "A Hartree–Fock–Bogoliubov mass formula". In: *Nuclear Physics A* 700.1 (2002), pp. 142–156. DOI: `https://doi.org/10.1016/S0375-9474(01)01316-1`.

[Sha64]   Irwin I. Shapiro. "Fourth Test of General Relativity". In: *Phys. Rev. Lett.* 13 (26 Dec. 1964), pp. 789–791. DOI: `10.1103/PhysRevLett.13.789`.

[SKT95]   K. Sumiyoshi, H. Kuwabara, and H. Toki. "Relativistic mean-field theory with non-linear σ and ω terms for neutron stars and supernovae". In: *Nuclear Physics A* 581.3 (1995), pp. 725–746. DOI: `https://doi.org/10.1016/0375-9474(94)00335-K`.

[SLL13]   K Stovall, D R Lorimer, and R S Lynch. "Searching for millisecond pul-sars: surveys, techniques and prospects". In: *Classical and Quantum Gravity* 30.22 (Nov. 2013), p. 224003. DOI: 10.1088/0264-9381/30/22/224003.

[SS06]   Devinderjit Sivia and John Skilling. *Data analysis: a Bayesian tutorial.* OUP Oxford, 2006.

[TCV08]   Luca Trippa, Gianluca Colò, and Enrico Vigezzi. "Giant dipole resonance as a quantitative constraint on the symmetry energy". In: *Phys. Rev. C* 77 (6 June 2008), p. 061304. DOI: 10.1103/PhysRevC.77.061304.

[Tol39]   Richard C. Tolman. "Static Solutions of Einstein's Field Equations for Spheres of Fluid". In: *Phys. Rev.* 55 (4 Feb. 1939), pp. 364–373. DOI: 10.1103/PhysRev.55.364.

[Vid+09] Isaac Vidaña et al. "Density dependence of the nuclear symmetry energy: A microscopic perspective". In: *Phys. Rev. C* 80 (4 Oct. 2009), p. 045806. DOI: 10.1103/PhysRevC.80.045806.

[Viñ+17] X. Viñas et al. "Crust-Core Transitions in Neutron Stars Revisited". In: *Bulg. J. Phys.* 44.S1 (2017), pp. 081–092.

[Wat+03] Gentaro Watanabe et al. "Structure of cold nuclear matter at subnuclear densities by quantum molecular dynamics". In: *Phys. Rev. C* 68 (3 Sept. 2003), p. 035806. DOI: 10.1103/PhysRevC.68.035806.

[Wat+16] Anna L. Watts et al. "Colloquium: Measuring the neutron star equation of state using x-ray timing". In: *Rev. Mod. Phys.* 88 (2 Apr. 2016), p. 021001. DOI: 10.1103/RevModPhys.88.021001.

[Wel+17] A. Welker et al. "Binding Energy of ^{79}Cu: Probing the Structure of the Doubly Magic ^{78}Ni from Only One Proton Away". In: *Phys. Rev. Lett.* 119 (19 Nov. 2017), p. 192502. DOI: 10.1103/PhysRevLett.119.192502.

[WFF88]   R. B. Wiringa, V. Fiks, and A. Fabrocini. "Equation of state for dense nucleon matter". In: *Phys. Rev. C* 38 (2 Aug. 1988), pp. 1010–1037. DOI: 10.1103/PhysRevC.38.1010.

[WM11]   Gentaro Watanabe and Toshiki Maruyama. *Nuclear pasta in supernovae and neutron stars.* 2011. arXiv: 1109.3511 [nucl-th].

[WP17]   Gentaro Watanabe and C. J. Pethick. "Superfluid Density of Neutrons in the Inner Crust of Neutron Stars: New Life for Pulsar Glitch Models". In: *Phys. Rev. Lett.* 119 (6 Aug. 2017), p. 062701. DOI: 10.1103/PhysRevLett.119.062701.

[WS33]   E. Wigner and F. Seitz. "On the Constitution of Metallic Sodium". In: *Phys. Rev.* 43 (10 May 1933), pp. 804–810. DOI: 10.1103/PhysRev.43.804.

[Xu +13] Xu, Y. et al. "Databases and tools for nuclear astrophysics applications - BRUSsels Nuclear LIBrary (BRUSLIB), Nuclear Astrophysics Compilation of REactions II (NACRE II) and Nuclear NETwork GENerator (NET-GEN)". In: *A&A* 549 (2013), A106. DOI: 10.1051/0004-6361/201220537.

[Yas+14]   Nobutoshi Yasutake et al. "Finite-size effects at the hadron-quark transition and heavy hybrid stars". In: *Phys. Rev. C* 89 (6 June 2014), p. 065803. DOI: 10.1103/PhysRevC.89.065803.

[YMT09]   Nobutoshi Yasutake, Toshiki Maruyama, and Toshitaka Tatsumi. "Hot hadron-quark mixed phase including hyperons". In: *Phys. Rev. D* 80 (12 Dec. 2009), p. 123009. DOI: 10.1103/PhysRevD.80.123009.

[YMT11]   Nobutoshi Yasutake, Toshiki Maruyama, and Toshitaka Tatsumi. "Pasta Structures of Quark-Hadron Phase Transition in Proto-Neutron Stars". In: *Journal of Physics: Conference Series* 312.4 (Sept. 2011), p. 042027. DOI: 10.1088/1742-6596/312/4/042027.

[ZH13]   J. L. Zdunik and P. Haensel. "Maximum mass of neutron stars and strange neutron-star cores". In: *Astron. Astrophys.* 551 (2013), A61. DOI: 10.1051/0004-6361/201220697. arXiv: 1211.1231 [astro-ph.SR].